Title
Aspects of earthquake triggering and seismicity clustering /

Permalink
https://escholarship.org/uc/item/8g78688w

Author
Chen, Xiaowei

Publication Date
2013

Peer reviewed|Thesis/dissertation

UNIVERSITY OF CALIFORNIA, SAN DIEGO

Aspects of earthquake triggering and seismicity clustering

A dissertation submitted in partial satisfaction of the
requirements for the degree
Doctor of Philosophy

in

Earth Sciences

by

Xiaowei Chen

Committee in charge:

Professor Peter M. Shearer, Chair
Professor Kevin Brown
Professor Ahmed-waeil Elgamal
Professor Yuri Fialko
Professor Frank Vernon

2013

The dissertation of Xiaowei Chen is approved, and it is acceptable in quality and form for publication on microfilm and electronically:

_____

_____

_____

_____

_____
Chair

University of California, San Diego

2013

DEDICATION

To my mom and dad - with love.

To my daughter and husband - with love.

EPIGRAPH

Long as the way is
I will keep on searching above and below.

—Qu Yuan

TABLE OF CONTENTS

LIST OF FIGURES

LIST OF TABLES

ACKNOWLEDGEMENTS

This dissertation marks the end of my student life. I have met so many great people here at San Diego, without whom, my life would not have been so delightful, and this dissertation could not possibly have been done.

First and foremost, I would like to thank my advisor Peter Shearer. I am really lucky to have the privilege to work with Peter on various projects in the past five years. His expertise in seismology, his attitude towards details of data, and his insights about scientific advancements, will always be the criteria I look up to. His door is always open for me for questions and requests. He always encourages me to attend conferences and discuss my research, even during my first year, he was supportive for me to attend AGU meeting.

I was very fortunate to have Yuri and Kevin on my committee, their knowledge on earthquake physics helped me a lot with interpretation and analysis of data. I also owe many thanks to Frank and Ahmed, who were very supportive on the progress of my research projects, especially Ahmed, who traveled from upper campus to my meetings.

I would also like to thank other people I have worked with. Kris helped me with the visualization of surface wave, and I also learned about shell commands from his scripts. Helen Fricker and Fabian Walter have contributed significant amount of intellectual inputs for Antarctica earthquakes. Guy has provided programs to analyze Antarctica events and encouraged me when the first paper was rejected. Rachel's insight on the behavior of the southern California clustering led to the third project, which was ranked most popular paper in JGR. I also thank Egill Hauksson for the rapid response to the 2012 earthquake swarm and the well-organized paper.

I owe a great debt of gratitude to many people in IGPP. Ashlee has been my classmate and officemate for the entire graduate school and we graduated together. She helped improve my English, learn American culture, and I really enjoyed the time we have together in the "barnyard". Janine, who knows almost everything about Matlab coding and latex, and has been an inspiring and supportive friend all along. I will miss the small-talks in the office. Zhitu, an "non-official" but

the most hard-working member of the "barnyard", without his presence, I may not have worked that hard. I thank Lindsay, who shared many useful baby-care information, and Wenyuan, who has been a great officemate in the past year, hope he would enjoy the quiet office in spring quarter. Xiaopeng, who shared the same flight from China to US in our first year, and has been a good friend ever since. Debi, who is always enthusiastic about her work, and has so many cute and useful things for my daughter. I also thank Valerie, Erica, Soli for my last-minute practice talk, which helped to relieve the stress level for the final moment.

I would like to thank all other faculty members, who have taught me in classes; staff members, who have taken care of all the paper works and computing issues. I also appreciate opportunities of many field classes and field trips, which have introduced me to the geological stories behind the scenes and a lot of desert fun.

My deep gratitude also goes to all other Chinese friends here, Shang, Liyan, Xiaoshan, Yangyang, Qian, Linghan, Xiuli. We had so much fun together, and I am always inspired by your happiness, especially Liyan and Xiaoshan, who are always positive about life. When Qian first arrived, I was so happy to meet another USTCer at SIO, especially someone who shares so many similarities with me. She is like a little sister, and I hope she will enjoy the beautiful San Diego as I did. Many thanks to Linghan for being such a supportive friend these years. Xiuli, who is the most amazing woman I ever met, and really miss the good old times at her house. I hope we can have opportunities to reunion somewhere in the future.

Finally, my endless love goes to my family. To my parents, your early guidance to science has led me the journey of scientific world, and you are very supportive about my decision to study abroad, which is far from home. To my husband, Minh, thank you for your support, encouragement, and confidence you have in me, I am very lucky to meet you in San Diego. Without you, my life would not have been the same. Finally, to my daughter, Mindi, you are always a source of happiness, and thank you for letting me experience the joy and bitterness journey of being a mom.

Chapter 2, in full, is a reformatted version of a publication in Journal of

Geophysical Research: Chen, X., P. M. Shearer, F. Walter, and H. A. Fricker, Seventeen Antarctic seismic events detected by global surface waves and a possible link to calving events from satellite images, *J. Geophys. Res.*, 116, doi: 10.1029/2011JB008262, 2011. I was the primary investigator and author of the paper, which describes how we detected and located 17 events in Antarctica, and analyzed best-fitting force directions with the CSF model to understand the relationship between the events and glacier movement.

Chapter 3, in full, is a reformatted version of a publication in Journal of Geophysical Research: Chen, X., and P. M. Shearer, Comprehensive analysis of earthquake source spectra and swarms in the Salton Trough, California, *J. Geophys. Res.*, 116, doi:10.1029/ 2011JB008263, 2011. I was the primary investigator and author of the paper, which describes how we analyzed source spectra of events in the Salton Trough and investigated their relationship with geothermal activities. We also studied 20 individual swarms in this region, and their migration behavior.

Chapter 4, in full, is a reformatted version of publication in Journal of Geophysical Research: Chen, X., P. M. Shearer, and R. E. Abercrombie, Spatial migration of earthquakes within seismic clusters in Southern California: Evidence for fluid diffusion, *J. Geophys. Res.*, 117, B04301, doi:10.1029/2011gratitude JB008973, 2012. I was the primary investigator and author of the paper, which describes how we analyzed spatial migration behavior of 69 seismicity bursts in southern California, and investigated the role of fluids in the migration.

Chapter 5, in full, has been submitted to Geophysical Research Letters: Chen, X., and P. M. Shearer, California foreshock sequences suggest underlying aseismic process, submitted to *Geophysical Research Letters*. I am the primary investigator and author of the paper, in which we examine the foreshock sequences for three M>7 mainshocks in southern California. We apply the relocation and source spectra methods to analyze foreshock spatial patterns and compare their stress drops with those of immediate aftershock sequences.

Chapter 6, in full, is being prepared for publication: Analysis of foreshock sequences in California–implications of foreshock triggering process. I am the primary investigator and author of the paper. In this Chapter, we study the general

behavior of foreshock occurrence patterns in California, and try to understand the relationship between precursors and fault zone properties.

VITA

2007	B. S. in Geophysics, University of Science and Technology of China
2010	M. S. in Earth Sciences, University of California, San Diego
2007-2013	Research Assistant, University of California, San Diego
2013	Ph. D. in Earth Sciences, University of California, San Diego

PUBLICATIONS

Chen, X., and P. M. Shearer, California foreshock sequences suggest underlying aseismic process, *Geophysical Research Letters*, under revision.

Haukkson, E., J. Stock, R. Bilham, M. Boese, X. Chen, M. Boese, E. J. Fielding, J. Galetzka, K. W. Hudnut, K. Hutton, L. M. Jones, H. Kanamori, P. M. Shearer, J. Steidl, J. Treiman, S. Wei, W. Yang, Report on the August 2012 Brawley earthquake swarm in Imperial Valley, Southern California, v. 84 no. 2 p. 177-189, doi: 10.1785/0220120169, *Seismological Research Letters*, March/April, 2013.

Chen, X., P. M. Shearer, and R. E. Abercrombie, Spatial migration of earthquakes within seismic clusters in Southern California: Evidence for fluid diffusion, *J. Geophys. Res.*, 117, B04301, doi:10.1029/2011JB008973, 2012.

Chen, X., and P. M. Shearer, Comprehensive analysis of earthquake source spectra and swarms in the Salton Trough, California, *J. Geophys. Res.*, 116, doi:10.1029/ 2011JB008263, 2011.

Chen, X., P. M. Shearer, F. Walter, and H. A. Fricker, Seventeen Antarctic seismic events detected by global surface waves and a possible link to calving events from satellite images, *J. Geophys. Res.*, 116, doi: 10.1029/2011JB008262, 2011.

ABSTRACT OF THE DISSERTATION

Aspects of earthquake triggering and seismicity clustering

by

Xiaowei Chen

Doctor of Philosophy in Earth Sciences

University of California, San Diego, 2013

Professor Peter M. Shearer, Chair

Earthquakes strongly cluster in space and time, driven both by earthquake-to-earthquake triggering and underlying physical processes, such as tectonic stress loading, increased pore pressure, etc. I explore both global and regional datasets to understand characteristics of these processes in different tectonic environments.

I study global seismicity using intermediate-period (35–70 s) Rayleigh waves recorded by the global seismic network. Applying a surface wave detect method identifies about 1000 previously un-cataloged earthquakes from 1997 to 2009, most of which are located in the southern ocean. I further analyze a small number of these events that are located in Antarctica to understand glacial-related triggering processes. Absolute and differential travel-times measured from waveform cross-correlation are used to obtain refined locations. A single-force model is applied

to the observed amplitudes at 50 Hz to obtain best-fitting force directions. Additionally, possible glacial calving events are identified from MODIS images. The combined results suggest that events on Vanderford and Ninnis glaciers are a result of calving processes.

To understand the general characteristics of earthquake clustering from a large dataset of earthquakes, I analyze seismicity in southern California. I use a high-resolution earthquake catalog based on waveform cross-correlation to study the spatial-temporal distribution of earthquakes. Parameters based on event location, magnitude and occurrence time are computed for isolated seismicity clusters. Spatial migration behavior is modeled using a weighted-least-squares method. Aftershock-like event clusters do not exhibit significant spatial migration compared with earthquake swarms. Two triggering processes are considered for swarms: slow slip and fluid diffusion, which are distinguished based on a statistical analysis of event migration. The results suggest fluid-induced seismicity is found across southern California, particularly within geothermal areas. In the Salton Sea geothermal field (SSGF), a correlation between seismicity and fluid injection activities is seen. Spatial-temporal variations of earthquake stress drops are investigated in different regions, and a distance-dependence of stress drop from the injection source is found in the SSGF, suggesting the influence of increased pore pressure. Temporal variation of stress drops within mainshock source regions shows that foreshocks and earthquake swarms have lower stress drops than background seismicity and aftershocks. These results, combined with the spatial migration observed for some large foreshock sequences, suggests an aseismic transient process is likely involved in foreshock triggering.

Chapter 1

Introduction

1.1 Overview of earthquakes and faulting

Rocks are moving and deforming due to the driving forces from active plate motion. Earthquakes occur as a result of the brittle failure of rocks, and faults are created from rock offsets. Different styles of plate boundaries are accompanied with different faulting mechanisms. At divergent boundaries, where new crust is created, extensional normal faulting mechanisms dominate. At convergence boundaries (subduction zones), where crust is recycled, compressional reverse faulting dominates. Strike-slip faulting is usually seen at transform fault boundaries.

Most earthquakes occur in the shallow crust from brittle failure of the rocks, and accommodate most of the fault motion. The upper crust is usually referred as the "seismogenic zone." At deeper depths, ductile deformation occurs and deformation is usually in the form of "fault creep". However, deeper earthquakes do occur in continental crust, which may reflect changes in the fault zone properties or stress changes due to other processes, such as gas or fluid [e.g., *Shelly and Hill*, 2011]. When and where earthquakes occur depends on the stress loading history, the strength of fault zones, and local geological features. Small earthquakes occur every day in California, however, large earthquakes (M>6) occur much less frequently and their average rate can be calculated based on earthquake moment release and stress loading histories from relative plate motions.

When earthquakes occur, they introduce changes in the surrounding (or

distant) stress field, often causing aftershocks, which produce event clustering in space and time. Statistical models based on Poisson processes have been proposed to explain the clustering due to aftershock triggering. These are termed "epidemic-type-aftershock-sequence" (ETAS) models [*Ogata*, 1998]. Some earthquake sequences are not associated with a clear large event, but appear associated with crustal transient processes, and their spatial-temporal evolution patterns are controlled by the transient process [e.g., *Lohman and McGuire*, 2007]. They are termed "earthquake swarms," and occur most often in volcanic, geothermal areas, and oceanic transform faults [*Roland and McGuire*, 2009; *Chen and Shearer*, 2011 and references therein].

1.2   Earthquake detection and relocation

Earthquake detection methods are usually based on P-wave amplitudes recorded by a seismic network. Earthquake magnitudes are observed to follow the Gutenberg Richter law:

$$log_{10}N_{(M \geq M_{min})} = a - bM_{min}, \qquad (1.1)$$

where the *b*-value is typically equal to 1.0, and *a* is a constant related to the total number of events in the catalog. Earthquake catalogs are thought to be complete above a certain threshold magnitude ("magnitude of completeness" M_c), which is about 1.2 for California [*Wiemer and Wyss,* 2000]. M_c varies with space and time, and is usually higher for regions with sparse networks or immediately after a large earthquake.

To obtain a more complete catalog to study earthquake triggering, different methods have been proposed to detect additional earthquakes. The method presented in Chapter 2 uses intermediate-period surface-wave signals to detect missing earthquakes in regions with relatively sparse seismic networks, such as the southern ocean and Arctic regions. In a region with a dense network, "matched-filter" methods are widely used. Waveform templates are constructed from cataloged events, and new events are identified based on their correlation with the templates. Application of these methods has detected over 10 times the number

of catalog events [e.g., *Shelly and Hill*, 2011]. These more complete earthquake catalogs have revealed detailed spatial-temporal patterns of seismicity, such as migration of earthquake swarms [*Shelly and Hill*, 2011], and migration of aftershock sequences [*Peng and Zhao*, 2009].

Waveform cross-correlation is also widely used in earthquake relocation. This can improve picking of weaker signals [e.g., *Buehler and Shearer*, 2012], and the differential times can also be directly used for large scale relocation. In Chapters 3 to 6, we use recently published high-resolution catalogs to analyze earthquake clustering behavior. These catalogs include: (1) Southern California (SoCal), *Lin et al.* [2007], *Hauksson et al.* [2012], both of these catalogs feature a two-staged relocation process. The first stage is done with the catalog phase picks and existing velocity model, the second stage uses differential times among similar event clusters; (2) Northern California (NoCal), *Waldhauser and Schaff*, [2008]. This catalog is based on the "double-difference" algorithm [*Waldhauser and Ellsworth*, 2002], which includes both catalog phase pick and differential times. These catalogs feature a precision of a few tens to a few hundred meters in terms of relative location and has greatly improved the understanding of relationships between earthquakes and tectonic processes.

1.3   Stress and loading

The recorded waveform at each station is a convolution of several terms, including the response at each station (both site response and instrumental response), the attenuation along the travel path, and the source spectra due to the earthquake rupture process. All the terms except the source term are often defined as the Green's function, which can be computed based on the known elastic properties of the material. The stress history at the source region is often represented by the moment tensor solution $M = \begin{bmatrix} M_{11} & M_{12} & M_{13} \\ M_{21} & M_{22} & M_{23} \\ M_{31} & M_{32} & M_{33} \end{bmatrix}$ The earthquake scalar

seismic moment M_0 can be derived from M from

$$M_0 = \frac{1}{\sqrt{2}} (\sum_{ij} M_{ij}^2)^{1/2} \tag{1.2}$$

[e.g., *Shearer*, 2009]. Earthquake focal mechanisms (strike, dip, rake) can be estimated from the double-couple part of the moment tensor. In Chapters 3 to 6, we explore the relationship of earthquake clustering characteristics with three major faulting styles: normal faulting, reverse faulting and strike-slip faulting. The styles of faulting are determined based on the rake ($-180° < \lambda < 180°$) of the fault plane [*Shearer*, 2009].

We obtain focal mechanism solutions from existing catalogs: (1) SoCal, HASH catalog [*Hardebeck and Shearer*, 2003] and YSH catalog [*Yang et al.*, 2012]; (2) NoCal, NCEDC (Northern California Earthquake Data Center) database. We calculate a parameter from λ which ranges from -1 to 1 using the formula [*Shearer et al.*, 2006]:

$$f = \begin{cases} \lambda/90 & \text{if } |\lambda| \leq 90; \\ (180 - |\lambda|) * (\lambda/|\lambda|) & \text{if } |\lambda| > 90. \end{cases} \tag{1.3}$$

where "-1" is normal faulting, "0" is strike-slip faulting, and "1" is reverse faulting. We test whether clustering behavior varies with faulting style, which would be helpful to understand possible relationships with the regional tectonic stress field. We find that normal faulting is usually associated with swarm-like sequences, in which the seismicity tends to migrate along a preferred direction (usually parallel to the fault strike). However, reverse faulting is usually associated with aftershock-like sequences, which do not exhibit spatial migration. These differing seismicity patterns could be related to differences in loading style [*Sibson*, 1993].

The principal stresses are designated as $\sigma_1 > \sigma_2 > \sigma_3$. From *Sibson* [1991], an *Andersonian* fault will lie at a reactivation angle relative to the maximum principal stress σ_1:

$$\theta_r = 0.5 \tan^{-1}(1/\mu) \tag{1.4}$$

The shear and normal stresses are then:

$$\tau = 0.5(\sigma_1 - \sigma_3) \sin(2\theta_r) \tag{1.5}$$

and

$$\sigma_n = 0.5[(\sigma_1 + \sigma_3) - (\sigma_1 - \sigma_3)\cos 2\theta_r]. \tag{1.6}$$

The static fault shear strength is:

$$\tau_f = \tau_0 + \mu(\sigma_n - P_f), \tag{1.7}$$

where τ_0 is the inherent strength of the fault, μ is the friction coefficient (about 0.75 from laboratory experiments), σ_n is the normal stress across the plane, and P_f the pore pressure within the fault zone [*Simpson*, 1986]. Failure occurs when τ exceeds the static strength τ_f.

Sibson [1991] analyzed the loading mechanisms related to the "end member" cases: reverse and normal faulting. The vertical stress (σ_v) is assumed constant during the loading process for dry crust ($P_f = 0$). In a compressional stress field, $\sigma_v = \sigma_3$, and therefore

$$\sigma_n = \sigma_v + \tan\theta_r\tau, \tag{1.8}$$

so the change in the frictional strength of a reverse fault is

$$\Delta\tau_f = \mu\Delta\sigma_n = \mu\tan\theta_r\Delta\tau. \tag{1.9}$$

In an extensional stress field, $\sigma_v = \sigma_1$, and therefore

$$\sigma_n = \sigma_v - \cot\theta_r\tau, \tag{1.10}$$

so the change in the frictional strength of a normal fault is

$$\Delta\tau_f = -\mu\cot\theta_r\Delta\tau. \tag{1.11}$$

Note that for reverse faulting, loading in shear stress will lead to an *increase* in both σ_n and τ_f, i.e., is "load-strengthening," while for normal faulting, loading will lead to a *reduction* in both σ_n and τ_f, i.e., is "load-weakening" (see Figure 1.1).

Thus, the post-failure effect is opposite for the two cases, where a stress drop in reverse faulting would accompany a reduction in strength, but would increase strength for normal faulting. This might explain the different seismcity patterns for the two end-member cases. The occurrence of foreshocks prior to large earthquakes
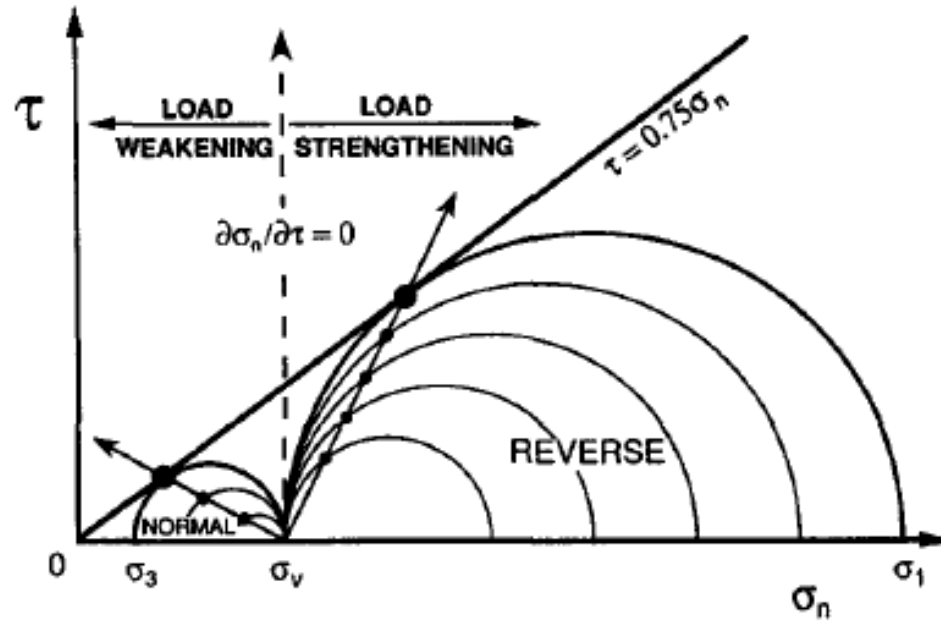
Figure 1.1: .

]Figure 2(a) in *Sibson* [1993]. Mohr diagram showing loading to failure of optimally oriented cohesionless reverse and normal faults with $\mu_s = 0.75$ from an initial lithostatic stress state in dry crust.

might be related to reduced fault strength toward the end of the "loading-cycle." And the swarm-like behavior in normal faulting regimes could be explained by the post-failure increased strength. A detailed analysis of loading history and fault strength changes would involve focal mechanism and stress inversion studies, and is a likely target for future research.

1.4   Source physics

Radiated seismic waves from a fault can often be modeled as resulting from a pure double-couple source, for which the trace and determinant of the moment tensor is zero. However, in some cases, for example, magma intrusion, explosion or landslide events, some non-double couple components are present. In Chapter 2, we try to explain seismic events in Antarctica with a centroid-single-force (CSF) model. The CSF model was initially proposed for landslide events by *Kanamori and Given* [1982], and has also been applied to glacial earthquakes in Greenland to obtain the best-fitting force direction [*Tsai et al.*, 2007]. The agreement between estimated force orientations and local ice-flow directions provides strong evidence for a correlation between seismic events and glacier sliding processes (e.g., *Tsai et al.* [2007]; *Nettles et al.* [2008]). In Chapter 2, we find the situation is less clear for the Antarctic events that we detect. Clusters of events on the Vanderford and Ninnis glaciers exhibit flow-parallel force directions, and some events are possibly associated with calving events identified from satellite images. However the temporal resolution for the calving events is several days and an exact match is hard to establish. Events on Ronnie Iceshelf exhibit different behavior with rift-parallel force directions, inconsistent with the more commonly observed glacier-related events, but may which relate to the rifting behavior in this region.

Other source parameters can be obtained from earthquake source spectra. In the log-frequency domain, the recorded displacement spectra can be modeled as a sum of different terms

$$D_{ij} = E_i + S_j + T_{k(i,j)} + R_{ij}. \tag{1.12}$$

where E_i is the event term, S_j is the station term, $T_{k(i,j)}$ is the propagation path

term and R_{ij} is the residual. Based on this equation, in regions with high seismicity and a dense seismic network, we can iteratively separate the different terms [*Shearer et al.*, 2006]. In Chapter 3, we apply this method to obtain source spectra for events in the Salton Trough. The resulting source spectra are a sum of the true source term and a near-source path term component that cannot be separated from the source term. To remove this ambiguity, we estimate an empirical Green's function (EGF) by computing the average misfit between theoretical spectra and stacked source spectra within different magnitude bins. From the final EGF-corrected source spectra, we fit a Brune-type source model [*Brune*, 1969]:

$$u(f) = \frac{\Omega_0}{1 + (f/f_c)^2} \tag{1.13}$$

and using the *Madariga* [1976] formula

$$f_c = \frac{0.42\beta}{(M_0/\Delta\sigma)^{1/3}} \tag{1.14}$$

we are able to obtain corner frequency (f_c), stress drop ($\Delta\sigma$), and moment magnitude (M_w). Figure 5.3 shows an example of fitting this source model to EGF-corrected source spectra.

Relationships between $\Delta\sigma$ variations and other factors are investigated in Chapters 3 and 5. In Chapter 3, I show that $\Delta\sigma$ is lower in the Salton Sea geothermal area, suggesting a relationship between stress drop and heat flux and temperature. Chapter 5 describes how foreshocks exhibit much lower $\Delta\sigma$ compared with immediate aftershock sequences for three $M > 7$ earthquakes in southern California. The three sequences appear associated with dilatational fault jogs, which may be related to reduced fault strength near the end of the loading cycle [*Sibson*, 1993].

1.5   Earthquake statistics

Aftershock sequences are one of the most commonly observed types of earthquake clustering and their statistical characteristics have been well studied. Two statistical laws that govern aftershock distributions are: (1) Båth's law: the average
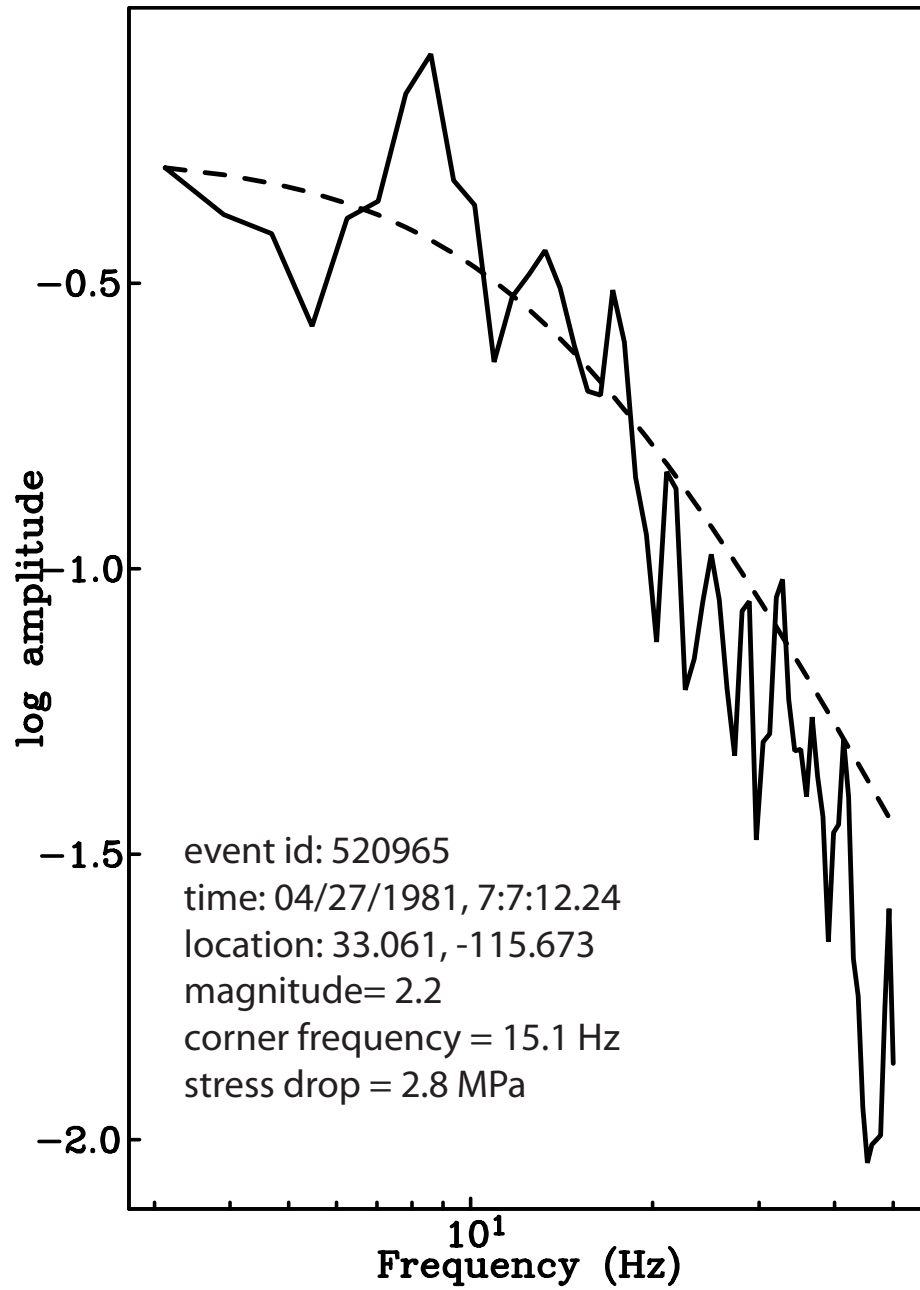
Figure 1.2: Example of model fit to an EGF-corrected source spectrum. Dashed line is predicted $u(f)$ from equation 3.2. Solid line is source spectrum. Fit is from 2 to 20 Hz.

magnitude difference between the largest aftershock and the mainshock $d_m = 1.2$; (2) Omori's law, the power-law decay of aftershocks with time:

$$n(t) = \frac{K}{(c+t)^p},$$ (1.15)

where K, c and p are constants, and $n(t)$ is the seismicity rate [Omori, 1894]. Larger earthquakes generate more aftershocks, and Ogata [1998] proposed the epidemic-type-aftershock-sequence (ETAS) model to explain temporal variations of seismicity:

$$n(t) = \mu + \sum_{t_i \leq t} \frac{K e^{\alpha(M_i - M_c)}}{(t - t_i + c)^p)},$$ (1.16)

where μ is the background seismicity rate, and α is the branching ratio that describes the magnitude-dependence of aftershock generation. More recent developments of this model have included the spatial decay of aftershock density [Ogata and Zhuang, 2006].

Parameters in equation 1.16 can be obtained via maximum likelihood methods as described in Ogata [1998] and many other studies. Simulated catalogs are able to explain many features of real catalogs, such as a reduced b-value for precursors, inverse Omori's law precursory behavior and spatial diffusion [Helmstetter et al., 2003]. However, seismicity resulting from processes other than earthquake-to-earthquake triggering tends to deviate from ETAS modeling predictions. For example, seismicity on the East Pacific Rise exhibits anomalously high foreshock-to-aftershock ratios [McGuire et al., 2005], induced seismicity in Oklahoma requires increased aftershock triggering efficiency (α) [Llenos and Michael, 2012], and earthquake swarms need an increased background seismicity rate (μ_0) [Hainzl et al., 2004]. The disagreement between ETAS models and catalog characteristics has been used to detect aseismic transients in regions with limited geodetic coverage [Llenos and McGuire, 2011].

The statistics of foreshocks are of special interest for earthquake forecasting and hazard analysis. There is currently no universal rule to explain the triggering process of foreshocks. In large catalog simulations, some studies have found that the averaged space-time behavior of foreshocks appears consistent with model predictions [Helmstetter et al., 2003]. However, a detailed comparison for the southern

California catalog suggests that the observed foreshock rate is much higher than model predictions [*Shearer*, 2012]. Individual foreshock sequences often exhibit "swarm-like" features, with spatial migration and no clear "mainshock" [*Kato et al.*, 2012; *Chen and Shearer*, 2013]. In Chapter 6, we show that foreshock occurrence is more frequent than predictions of ETAS-like models for southern California. These observations suggest that foreshock sequences may not originate from the same triggering process as aftershocks.

1.6   Role of fluids

From equation 1.7, changes in pore pressure will increase the probability of failure under the Coulomb failure criteria. The creation of pores (dilatancy) due to fault slip is an important mechanism for interactions between fluids and earthquake ruptures [*Yamashita*, 1999]. Earthquake sequence evolution is dependent on the rate of pore creation. With a high rate and small critical slip distance, earthquake swarms are likely to be observed, while mainshock-aftershock sequences are less likely to occur [*Yamashita*, 1999]. Swarms tend to have higher *b*-values (around 1.2 in geothermal areas [*Farrell et al.*, 2009], which means they contain a relatively higher portion of small events relative to large events.

Direct relationships between fluid pressure changes and seismicity have been observed and analyzed for both artificial (e.g., hydraulic fluid injection [*Shapiro et al.*, 2002]) and natural origins (e.g., water level changes [*El Hariri et al.*, 2010] of fluid perturbations. Fluid injection experiments aim to increase permeability at geothermal or tight-gas reservoirs for industrial purposes. Micro-earthquakes induced by these processes exhibit several features related to fluid pressure diffusion [*Shapiro et al.*, 2002; *Shapiro et al.*, 2005]. Pore pressure perturbations in space and time are controlled by the hydraulic diffusivity (D):

$$\frac{\partial p(t, \mathbf{r})}{\partial t} = D\nabla^2 p(t, \mathbf{r}), \tag{1.17}$$

where t is time and $\mathbf{r}$ is the location vector [*Shapiro et al.*, 2003]. The permeability-related features of induced seismicity follow the concept of a triggering front, where the fluid injection is approximated by a point source of pore pressure perturbation.
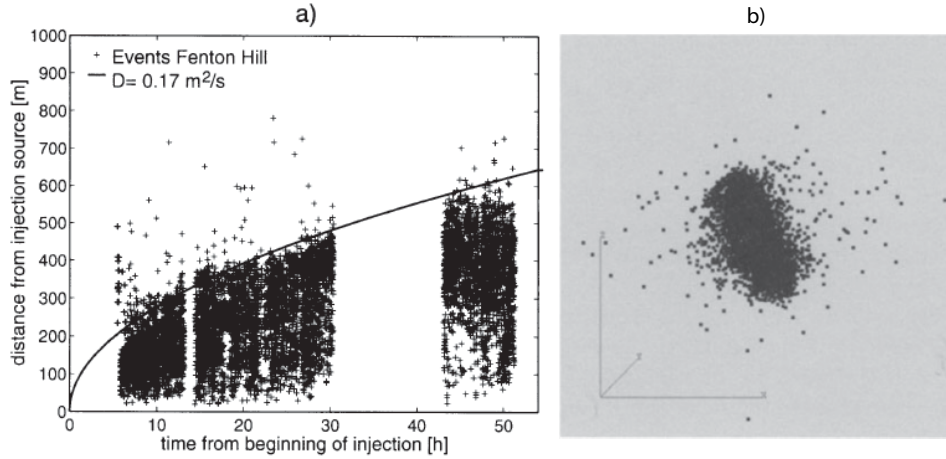
Figure 1.3: Example of the Fenton Hill microseismicity. (a) Event distance versus time (points), together with predicted seismicity onset for a homogeneous medium (curve0. (b) 3D view for a heterogeneous medium with axes rotated to principal diffusivity. (From *Shapiro et al.*, 2003]

In this model, at a given time t_0, events will occur at distances within the relaxation zone of the pore pressure perturbation, thus, in a time versus distance diagram, seismicity will be enclosed by an envelope function illustrating the triggering front [*Shapiro et al.,* 2003] (see Figure 1.3)

$$r = \sqrt{4\pi Dt} \tag{1.18}$$

It should be noted that a homogeneous, isotropic medium is assumed, and D is the scalar hydraulic diffusivity. In nature, the medium is likely heterogeneous and anisotropic, and the actual diffusivity will be a tensor. If we consider the 3D distribution of seismicity, it will look like an ellipsoid with half-axes equal to the square roots of the principal diffusivities [*Shapiro et al.*, 2003] (see Figure 1.3). Thus, the spatial-temporal distribution of the induced seismicity cloud is controlled by the diffusivity tensor. The relationship between the hydraulic diffusivity and permeability is derived from Darcy's law, and follows:

$$\mathbf{D} = N\mathbf{K}/\eta \tag{1.19}$$

where $\mathbf{K}$ is the permeability tensor, η is the dynamic viscosity and N is the poroelastic modulus, which relates to the bulk modulus and porosity [*Shapiro et al.*,

2003]. Natural permeability ranges between $10^{-17}-10^{-15}m^2$, and diffusivity ranges from 0.01 to 10 m^2/s [*Shapiro et al.*, 2003, and references therein].

Chapter 3 describes how within the Salton Sea geothermal field, the beginning of several earthquake swarms exhibit fluid-diffusive migration patterns, with diffusivities ranging from 0.1 to 0.4 m^2/s [*Chen and Shearer*, 2011]. Chapter 4 extends this analysis to all of southern California, showing that 18 out of 69 swarms are best explained with diffusive migration, with some of them located near active geothermal injection wells. The detailed correlations in the Coso geothermal field may warrant future investigation [*Chen et al.*, 2012]. As as discussed in *Sibson* [1993], the maximum permeability lies along the σ_2 direction, so a comparison between principal stresses and the permeability tensor may provide constraints on the theoretical solution. We also note that the range of diffusivities agrees with previous studies on fluid properties, with higher values in geothermal and volcanic areas, and lower values in dry (hot-dry-rock) reservoirs and natural fault zones (see Figure 1.4).

As mentioned before, the existence of pore fluids may reduce effective normal stress and fault frictional strength. Higher stress drops associated with higher applied shear stress have been observed in some regions, e.g., increased stress drop with depth and reverse faulting is found in the San Francisco Bay area using borehole data [*Hardebeck and Aron* 2009]. A negative correlation between stress drop and pore pressure perturbations during hydraulic injection events is also found for the Basel geothermal reservoir [*Allmann et al.*, 2010]. In the Salton Sea geothermal field, the situation is complicated with multiple active injection wells in a smaller region. It is difficult to compare stress drop with pore pressure perturbations directly. However, the pore pressure should decrease with distance away from the injection source, and we have found increased stress drop with distance away from the closest injection well, which is consistent with the single injection event model [*Chen and Shearer*, 2011]. It should be noted that individual stress drops vary over several magnitudes (from 0.01 to 10 MPa); these results are based on the median values within distance bins containing equal numbers of events. There have been other studies that reported no correlation between stress drop and depth [*Allmann*
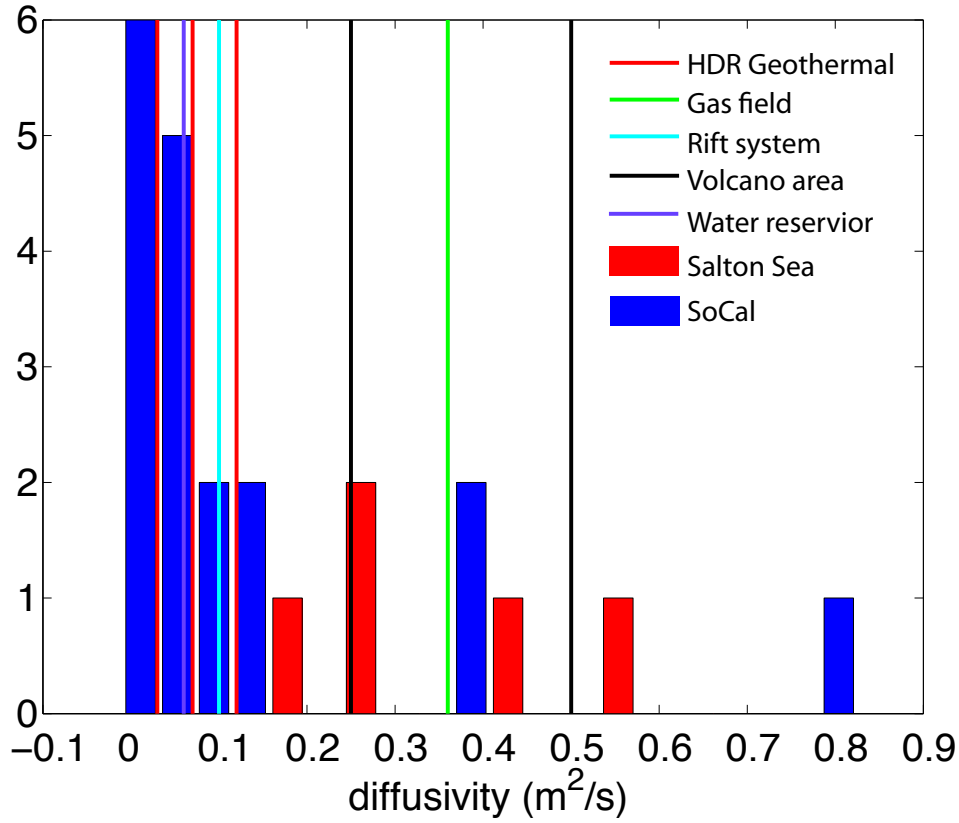
Figure 1.4: Histogram of the estimated fluid diffusivity distribution for swarms in the Salton Trough *Chen and Shearer*, 2011] and Southern California [*Chen et al.*, 2012]. The vertical lines are diffusivities from other studies at different environments: HDR-values from *Audigane et al.* [2002] and *Shapiro et al.*, [2005]; volcanic region from *Parotidis et al.*, [2005] and *Yukutake et al.*, [2011]; water reservoir from *El Hariri et al.*, [2010]; gas field from *Shapiro et al.*, [2005]; rift value from *Pacchiani and Lyon-Caen*, [2010].

and Shearer, 2007] or focal mechanism [*Shearer et al.*, 2006]. Thus, explanations for factors governing the variation of stress drops may be complex.

Other evidence for fluids includes the systemic rotation of σ_1 to lower angles to the fault plane inside the fault zone, suggesting high fluid pressure within active fractures sealed by low-permeable barriers [*Hardebeck and Hauksson*, 1999]. Tomography images of low Vp/Vs ratios within earthquake cluster source region, also supports the existence of water-filled cracks within fault zones [*Lin and Shearer*, 2009].

1.7   Structure of the thesis

Chapter 2, in full, is a reformatted version of a publication in Journal of Geophysical Research: Chen, X., P. M. Shearer, F. Walter, and H. A. Fricker, Seventeen Antarctic seismic events detected by global surface waves and a possible link to calving events from satellite images, *J. Geophys. Res.*, 116, doi: 10.1029/2011JB008262, 2011. I was the primary investigator and author of the paper, which describes how we detected and located 17 events in Antarctica, and analyzed best-fitting force directions with the CSF model to understand the relationship between the events and glacier movement.

Chapter 3, in full, is a reformatted version of a publication in Journal of Geophysical Research: Chen, X., and P. M. Shearer, Comprehensive analysis of earthquake source spectra and swarms in the Salton Trough, California, *J. Geophys. Res.*, 116, doi:10.1029/ 2011JB008263, 2011. I was the primary investigator and author of the paper, which describes how we analyzed source spectra of events in the Salton Trough and investigated their relationship with geothermal activities. We also studied 20 individual swarms in this region, and their migration behavior.

Chapter 4, in full, is a reformatted version of publication in Journal of Geophysical Research: Chen, X., P. M. Shearer, and R. E. Abercrombie, Spatial migration of earthquakes within seismic clusters in Southern California: Evidence for fluid diffusion, *J. Geophys. Res.*, 117, B04301, doi:10.1029/2011JB008973, 2012. I was the primary investigator and author of the paper, which describes

how we analyzed spatial migration behavior of 69 seismicity bursts in southern California, and investigated the role of fluids in the migration.

Chapter 5, in full, has been submitted to Geophysical Research Letters: Chen, X., and P. M. Shearer, California foreshock sequences suggest underlying aseismic process, submitted to *Geophysical Research Letters.* I am the primary investigator and author of the paper, in which we examine the foreshock sequences for three M>7 mainshocks in southern California. We apply the relocation and source spectra methods to analyze foreshock spatial patterns and compare their stress drops with those of immediate aftershock sequences.

Chapter 6, in full, is being prepared for publication: Analysis of foreshock sequences in California–implications of foreshock triggering process. I am the primary investigator and author of the paper. In this Chapter, we study the general behavior of foreshock occurrence patterns in California, and try to understand the relationship between precursors and fault zone properties.

References

Allmann, B. P., and P. M. Shearer (2007), Spatial and temporal stress drop variations in small earthquakes near parkfield, california, *Journal of Geophysical Research-Solid Earth*, *112*(B4), 17.

Allmann, B. P., A. Goertz, and S. Wiemer (2010), Stress drop variations of induces earthquakes at the basel geothermal site, *Geophysical Research Letters.*

Audigane, P., J. J. Royer, and H. Kaieda (2002), Permeability characterization of the soultz and ogachi large-scale reservoir using induced microseismicity, *Geophysics*, *67*(1), 204–211.

Brune, J. N. (1969), Tectonic stress and the spectra of seismic shear waves from earthquakes, *J. Geophys. Res.*, *75.*

Buehler, J. S., and P. Shearer (2012), Localized imaging of the uppermost mantle with usarray pn data, *J. Geophys. Res.*, *117.*

Chen, X., and P. M. Shearer (2011), Comprehensive analysis of earthquake source spectra and swarms in the salton trough, california, *J. Geophys. Res.*, *116*(B09309).

Chen, X., P. M. Shearer, F. Walter, and H. A. Fricker (2011), Seventeen antarctic seismic events detected by global surface waves and a possible link to calving events from satellite images, *J. Geophys. Res.*, *116*(B06311).

Chen, X., P. M. Shearer, and R. Abercrombie (2012), Spatial migration of earthquakes within seismic clusters in southern california: Evidence for fluid diffusion, *J. Geophys. Res.*, *117*(B04301).

El Hariri, M., R. E. Abercrombie, C. A. Rowe, and A. F. do Nascimento (2010), The role of fluids in triggering earthquakes: observations from reservoir induced seismicity in brazil, *Geophysical Journal International*, *181*(3), 1566–1574.

Farrell, J., S. Husen, and R. B. Smith (2009), Earthquake swarm and b-value characterization of the yellowstone volcano-tectonic system, *Journal of Volcanology and Geothermal Research*, *188*(1-3), 260–276.

Hainzl, S. (2004), Seismicity patterns of earthquake swarms due to fluid intrusion and stress triggering, *Geophysical Journal International*, *159*(3), 1090–1096.

Hardebeck, J. L., and A. Aron (2009), Earthquake stress drops and inferred fault strength on the hayward fault, east san francisco bay, california, *Bulletin of the Seismological Society of America*, *99*(3), 1801–1814.

Hardebeck, J. L., and E. Hauksson (1999), Role of fluids in faulting inferred from stress field signatures, *Science*, *285*, 236.

Hardebeck, J. L., and P. M. Shearer (2003), Using s/p amplitude ratios to constrain the focal mechanisms of small earthquakes, *Bulletin of the Seismological Society of America*, *93*(6), 2434–2444.

Hauksson, E., W. Yang, and P. M. Shearer (2012), Waveform relocated earthquake catalog for southern california (1981 to june 2011), *Bulletin of the Seismological Society of America*, *102*(5), 2239–2244.

Helmstetter, A., D. Sornette, and J. R. Grasso (2003), Mainshocks are aftershocks of conditional foreshocks: How do foreshock statistical properties emerge from aftershock laws, *Journal of Geophysical Research-Solid Earth*, *108*(B1), 24.

Kanamori, H., and J. W. Given (1981), Use of long-period surface-waves for rapid-determination of earthquake-source parameters, *Physics of The Earth and Planetary Interiors*, *27*(1), 8–31.

Kato, A., K. Obara, T. Igarashi, H. Tsuruoka, S. Nakagawa, and N. Hirata (2012), Propagation of slow slip leading up to the 2011 m-w 9.0 tohoku-oki earthquake, *Science*, *335*(6069), 705–708.

Lin, G. Q., and P. M. Shearer (2009), Evidence for water-filled cracks in earthquake source regions, *Geophysical Research Letters*, *36*, 5.

Lin, G. Q., P. M. Shearer, and E. Hauksson (2007), Applying a three-dimensional velocity model, waveform cross correlation, and cluster analysis to locate southern california seismicity from 1981 to 2005, *Journal of Geophysical Research-Solid Earth*, *112*(B12), 14.

Llenos, A. L., and J. J. McGuire (2011), Detecting aseismic strain transients from seismicity data, *Journal of Geophysical Research-Solid Earth*, *116*, 17.

Lohman, R. B., and J. J. McGuire (2007), Earthquake swarms driven by aseismic creep in the salton trough, california, *Journal of Geophysical Research-Solid Earth*, *112*(B4).

Madariaga, R. (1976), Dynamics of an expanding circular fault, *Bull. Seismol. Soc. Am.*, *66*, 639–666.

McGuire, J. J., M. S. Boettcher, and T. H. Jordan (2005), Foreshock sequences and short-term earthquake predictability on east pacific rise transform faults, *Nature*, *434*(7032), 457–461.

Nettles, M., T. B. Larsen, P. Elsegui, G. S. Hamilton, L. A. Stearns, A. P. Ahlstrm, J. L. Davis, M. L. Andersen, J. de Juan, S. A. Khan, L. Stenseng, G. Ekstrm, and R. Forsberg (2008), Step-wise changes in glacier flow speed coincide with calving and glacial earthquakes at helheim glacier, greenland, *Geophys. Res. Lett.*, *35*.

Ogata, Y. (1988), Statistical-models for earthquake occurrences and residual analysis for point-processes, *Journal of the American Statistical Association*, *83*(401), 9–27.

Ogata, Y. (1998), Space-time point-process models for earthquake occurrences, *Annals of the Institute of Statistical Mathematics*, *50*(2), 379–402.

Ogata, Y., and H. C. Zhuang (2006), Space-time etas models and an improved extension, *Tectonophysics*, *413*(1-2), 13–23.

Omori, F. (1894), On the aftershocks of earthquakes, *Journal of the College of Science, Imperial University of Tokyo*, *7*, 111–200.

Pacchiani, F., and H. Lyon-Caen (2011), Geometry and spatio-temporal evolution of the 2001 agios ioanis earthquake swarm (corinth rift, greece), *Geophysical Journal International*, *180*(1), 59–72.

Parotidis, M., S. A. Shapiro, and E. Rothert (2005), Evidence for triggering of the vogtland swarms 2000 by pore pressure diffusion, *Journal of Geophysical Research-Part B-Solid Earth*, *110*(B5), 12 pp.–12 pp.12 pp.

Peng, Z., and P. Zhao (2009), Migration of early aftershocks following the 2004 parkfield earthquake, *Nature*, *2*.

Roland, E., and J. J. McGuire (2009), Earthquake swarms on transform faults, *Geophysical Journal International*, *178*(3), 1677–1690.

Shapiro, S. A., E. Rothert, V. Rath, and J. Rindschwentner (2002), Characterization of fluid transport properties of reservoirs using induced microseismicity, *Geophysics*, *67*(1), 212–220.

Shapiro, S. A., S. Rentsch, and E. Rothert (2005), Characterization of hydraulic properties of rocks using probability of fluid-induced microearthquakes, *Geophysics*, *70*(2), F27–F33.

Shearer, P. M. (—2009—), *Introduction to Seismology*, second edition ed., Cambridge University Press.

Shearer, P. M., G. A. Prieto, and E. Hauksson (2006), Comprehensive analysis of earthquake source spectra in southern california, *Journal of Geophysical Research-Solid Earth*, *111*(B6).

Shelly, D. R., and D. P. Hill (2011), Migrating swarms of brittle-failure earthquakes in the lower crust beneath mammoth mountain, california, *Geophys. Res. Lett.*, *38*(20), L20,307.

Sibson, R. H. (1991), Loading of faults to failure, *Bull. Seismol. Soc. Am.*, *81*(6), 2493–2497.

Sibson, R. H. (1993), Load-strengthening versus load-weakening faulting, *J. Struct. Geol.*, *15*(2), 123–128.

Sibson, R. H. (2001), Seismogenic framework for hydrothermal transport and ore deposition, *Society of Economic geologists*, *14*, 25–50.

Simpson, D. W. (1986), Triggered earthquakes, *Annual Review of Earth and Planetary Sciences*, *14*, 21–42.

Tsai, V. C., and G. Ekstrom (2007), Analysis of glacial earthquakes, *Journal of Geophysical Research-Earth Surface*, *112*(F3).

Waldhauser, F., and W. L. Ellsworth (2002), Fault structure and mechanics of the hayward fault, california, from double-difference earthquake locations, *Journal of Geophysical Research-Solid Earth*, *107*(B3), 17.

Waldhauser, F., and D. P. Schaff (2008), Large-scale relocation of two decades of northern california seismicity using cross-correlation and double-difference methods, *J. Geophys. Res.*, *113*(B08311).

Wiemer, S., and M. Wyss (2000), Minimum magnitude of completeness in earthquake catalogs: Examples from alaska, the western united states, and japan, *Bulletin of the Seismological Society of America*, *90*(4), 859–869.

Yamashita, T. (1999), Pore creation due to fault slip in a fluid-permeated fault zone and its effect on seismicity: Generation mechanism of earthquake swarm, *Pure and Applied Geophysics*, *155*(2-4), 625–647.

Yang, W., E. Hauksson, and P. M. Shearer (2012), Computing a large refined catalog of focal mechanisms for southern california (1981-2010): Temporal stability of the style of faulting, *Bulletin of the Seismological Society of America*, *102*(3), 1179–1194.

Yukutake, Y. Y. Y., H. Ito, R. Honda, M. Harada, T. Tanada, and A. Yoshida (2011), Fluid-induced swarm earthquake sequence revealed by precisely determined hypocenters and focal mechanisms in the 2009 activity at hakone volcano, japan, *Journal of Geophysical Research-Solid Earth*, *116*, 13.

Chapter 2

Seventeen Antarctic seismic events detected by global surface waves and a possible link to calving events from satellite images

We detect 17 seismic events in Antarctica from 1997 to 2009 by applying a surface-wave detector to global seismic data. We locate these events using a waveform cross-correlation method and find that most occurred near the coast of Antarctica, and are clustered in three regions: four events are on the Ronne Ice Shelf, close to the location of a 1998 calving event; five events are near the Vanderford Glacier; and eight events are near the Ninnis Glacier. The observed Rayleigh and Love waves for these events have similar amplitudes and a two-lobed radiation pattern, matching the expected amplitude behavior of a single-force source model. Using such a model, we obtain best-fitting horizontal force directions for the 14 events that have relatively better signal-to-noise ratios. Analysis of coastline changes from MODIS images before and after the detected events show that two events on Vanderford Glacier and one event near Ninnis Glacier are

likely associated with calving events. Moreover, the inferred force directions for the seismic events appear consistent with local ice flow directions. Both satellite observations and modeling results strongly suggest a link between seismic events and calving processes in the two regions. However, the force directions on the Ronne Ice Shelf are aligned with observed rift propagation directions, suggesting that these events may arise from rifting processes.

2.1 Introduction

Since the 1970s, glaciologists have found that changes in ice dynamic processes can sometimes be fast enough (i.e., seconds to minutes) to generate seismic waves that can be recorded by seismometers. Previous observations include crevassing events with high frequency ($\sim$100 Hz) [*Neave and Savage*, 1970], calving events at frequencies of $\sim$1 to 3 Hz [*O'Neel et al.*, 2007; *Walter et al.*, 2010], and basal microseismicity from stagnant ice stream C in west Antarctica [*Anandakrishnan and Alley*, 1997]. Surface-wave energy is observed at some regions, such as repeating ice quakes with an excess of surface-wave energy from 0.1 to 1 Hz [*Danesi et al.*, 2007], teleseismically observed glacial earthquakes and earthquakes from stick-slip motion of ice streams with significant surface-wave energy lower than $\sim$0.5 Hz [*Ekström et al.*, 2003, *Wiens et al.*, 2008].

Most of the reported events have been detected using local seismic networks and generally have magnitudes ranging from -3 to 2.5 [*Walter et al.*, 2009; *Danesi et al.*, 2007]. The glacial earthquakes reported by *Ekström et al.* [2003] were different, however, in that they had larger sizes, indicating larger ice volumes involved in glacier displacement processes, and a relative lack of high frequency energy, which explains why they were missing from traditional catalogs despite equivalent magnitudes of 4.6 to 5.1. *Ekström* [2006] detected glacial earthquakes in Greenland, Alaska and Antarctica from a surface-wave detector. *Tsai and Ekström* [2007] focused on events in Greenland, where most of these glacial earthquakes are located. They analyzed 184 events that occurred in Greenland between 1995 and 2005, studied their temporal and spatial distributions as well as their source

mechanisms, and found that: (1) after relocation, events clustered in outlet glacier regions, indicating they are probably associated with fast ice flow; (2) a centroid single force (CSF) model fits waveforms better than traditional centroid moment tensor (CMT) solutions, indicating that these events are similar to landslides in mechanism, and their force directions are consistent with ice flow directions; (3) the temporal distributions are different in different regions, however, they generally have higher occurring rates in summer, when surface melting occurs. Also in Greenland, detailed satellite images reveal a strong correspondence between glacial earthquakes and ice-front retreat, and their occurrence agrees well with seasonal variations of calving rates [*Joughin et al.*, 2008]. *Amundson et al.* [2008] found a correlation between glacial earthquakes and calving events that include overturning icebergs, however, they found no recordable glacial response during glacial earthquakes as suggested by a glacier sliding model [*Tsai et al.*, 2008]. A direct link between calving events, glacial earthquakes and ice flow was established by *Nettles et al.* [2008] and *de Juan et al.* [2010] from GPS surveys and seismic records. Thus a variety of different studies now strongly link glacial earthquakes in Greenland with major calving events.

In Antarctica, only a small number of possible glacial earthquakes have been identified. More than 500 seismic events in West Antarctica have been recorded with two Global Seismic Network stations. The magnitudes of these events range from 3.6 to 4.2, with surface-wave energy between 20 and 150 s, however, they seem to result from stick-slip motion of Whillans Ice Stream [*Wiens et al*, 2008]. Furthermore, *Nettles and Ekström* [2010] reported detection of 14 Antarctic events from global surface waves between 1993 and 2008, which locate near the Antarctic coast.

Here, we describe results of applying a surface-wave detector to global seismic data from 1997 to 2009. Similar to *Ekström* [2006], we find hundreds of previously uncataloged earthquakes, including many possible glacial events in Greenland, Alaska, and Antarctica. The majority of these events are in Greenland, and many were previously included in the catalog of *Tsai and Ekström* [2007]. We focus our analysis on 17 events detected in Antarctica and compute refined

locations using waveform cross-correlation. These events are clustered in three regions: (i) the Ronne Ice Shelf, West Antarctica, (ii) near Vanderford Glacier, East Antarctica, and (iii) near Ninnis Glacier, East Antarctica. We model their generation mechanism with a centroid single-force model similar to that used in *Tsai and Ekström* [2007]. We also compare the computed force directions of the events with local ice flow directions (I. Joughin, personal communication, 2009) obtained from InSAR data [*Joughin*, 2002], deglaciation crustal response [*James et al.*, 1995; *James et al.*, 1998], rift propagation [*Larour et al.*, 2004; *Rignot and MacAyeal*, 1998] and satellite imaging of possible calving events, to determine the most likely source mechanisms for the events in each region.

2.2 Seismic Event Detection

Our seismic detection approach is similar to previous surface-wave detection methods used by *Shearer* [1994] and *Ekström* [2006], which work by performing a computer search for times and locations of possible events that predict seismic arrivals that match the observations. *Shearer* [1994] collected data from the IDA (International Deployment of Accelerometers) network, stacked seismograms from 564 events ($m_b \geq 6$) recorded at very long periods ($T \geq 60$ s), and used the first 3 hours of this time versus range image to construct a matched filter. Then using a global grid of candidate earthquake locations, he stacked seismograms with respect to source-receiver range to produce a time versus range function, which he cross-correlated with the matched filter to produce peaks of likely events as a function of time and location. Application of this method to 11 years of IDA data from 1981 to 1991 identified 4061 events, including 65% of cataloged events of $m_b \geq 5.5$ and 32 new events. *Ekström* [2006] used LHZ (long-period, high-gain seismometer, vertical component) seismograms from global networks with broad-band instrumentation and defined a $4^o \times 4^o$ grid of points as target locations. At each target location, he deconvolved a propagation operator for each station, and selected stations based on the observed noise level, probable signal level, and contribution to azimuthal coverage. He then calculated envelope functions, correlated

them with a template peak shape, and defined detections by high correlations occurring on multiple stations at the same time. Once an event was detected, the location was refined using a 0.25º × 0.25º grid, a quality grade was assigned, and a magnitude estimated based on the envelope-function amplitude. Analysis of data from 1993 to 2003 detected 24,412 events, including 9482 of 10,159 (93.3%) CMT earthquakes and 1301 new events not listed in the PDE (Preliminary Determinations of Epicenters), ISC (International Seismological Center) and REB (Reviewed Event Bulletin) catalogs.

In our approach, we begin by obtaining continuous VHZ (very-long-period, high-gain seismometer, vertical component) data archived at the IRIS DMC at a 0.1 Hz sample rate (10 s sample interval). We organize the data into monthly files and band-pass filter the seismograms between 0.014 and 0.028 Hz. We then apply an automatic gain control filter as described by *Shearer* [1991] to normalize the amplitudes by calculating a 2-minute short-term-average to 15-minute long-term-average (STA/LTA) ratio. In this way, we discard the polarity information of the data and use envelope functions with positive values only for stacking. We define 1654 5º × 5º grid points as candidate earthquake locations. The grid points are spaced at approximately equal distance, resulting in increased longitude spacing near the poles. At each target location, we align the envelope functions by source-receiver range and stack them along a predicted Rayleigh wave group-velocity travel-time curve, using 3.955 km/s as an approximate value for the globally average group velocity. To provide more uniform global contributions to the stack from regions that may have very different station densities, we weight each trace inversely by the number of traces within 30° bins in azimuth and distance from the target event location. The result of this stacking procedure is a function of space (discretized at 5° increments) and time (discretized at 10 s intervals) that contains peaks that most likely correspond to seismic events.

We compare the times and locations of these peaks with those of known events in the PDE, ISC and REB catalogs. If the time offset between a peak and an event in the catalog is less than 20 minutes and the distance offset is less than 20°, the peak is automatically associated with the catalog event. While this is the case

for most of our detections, some of the peaks do not correspond to catalog events. We use a graphical user interface (GUI) tool to plot record sections for unassociated peaks and visually check them to weed out false triggers (e.g., artifacts due to random alignment of noise spikes, second arriving Rayleigh wave misidentified as first arrival, etc.). We also use the GUI to examine cataloged events within a larger spatial and temporal range than used in our automatic association method in order to identify missed associations. Sometimes the occurrence of two or more events at similar times but different locations can confuse our algorithm, and these situations must be handled manually. For the confirmed "new" events, we assign a quality Grade (A, B or C), which depends on the coherence and robustness of the signal. Grade A is reserved for obvious events with well-defined arrivals over a wide distance range. Grade B is for weaker, more intermittent arrivals, but where an event is still clearly present. Grade C is for marginal signals where an event is likely but not conclusively present. Figure 2.1 shows examples of the GUI output for events assigned Grades B and C in Antarctica.

With this method, we detect 78% of the events in the Global Centroid Moment Tensor (CMT) catalog between 1997 and 2009, and 1100 new events not listed in the PDE, ISC and REB catalogs. Many of these new events were previously detected by *Ekström* [2006] using a similar surface-wave detection method. Our analysis here focuses on 17 uncataloged events found in Antarctica (14 Grade B and 3 Grade C), four of which were also identified by the surface-wave detection algorithm described by *Nettles and Ekström* [2010]. These events are clustered into three groups in the following locations: (i) the Ronne Ice Shelf, (ii) near Ninnis Glacier, and (iii) Vanderford Glacier. Waveforms for events with Grade C are generally poorly coherent, with an identifiable signal at very few stations, therefore, our analysis focuses on the 14 Grade B events. We also compute equivalent surface-wave magnitudes using the measured amplitudes at 50 s for the Grade B events.

2.3 Relocation

Our initial locations have a nominal accuracy of only 5° (556 km) because they are derived from a coarse grid of candidate locations and a single fixed Rayleigh-wave velocity. In order to estimate the locations more accurately, we apply a waveform cross-correlation approach to obtain more precise Rayleigh-wave arrival times for each station, and then search for the best-fitting location using a much finer grid at 0.5° spacing and a model of lateral variations in Rayleigh-wave group velocity. We relocate the events in two different ways: (i) single event location, in which we locate each event separately using the Rayleigh wave arrival times at the different stations recording the event; and (ii) relative event location for events within each cluster, in which we use differential arrival times among the different events recorded at the same station. We only perform relocation for the 14 Grade-B events because of the very low signal-to-noise of the three Grade-C events.

2.3.1 Absolute location for single events

To locate single events, we cross-correlate the envelope functions derived from the STA/LTA filter to obtain relative arrival times at each of the stations that recorded an event. By using the envelope functions, we do not need to correct for phase or polarity differences from the source and we also find that the effect of dispersion is small in our band-pass filtered data. We develop an iterative method to cross-correlate the envelope functions with a stack for each event (this stack is the sum of the aligned individual envelopes at each iteration). We use a 20-minute window and permit time shifts of ± 3.33 minutes with respect to a reference time defined by the assumed group velocity of 3.955 km/s. The final arrival times are obtained from the shifted traces with a precision of 10 s, and we use only times for which the correlation coefficient between the station envelope functions and the reference stack is 0.5 or greater. Figure 2.2 shows an example of aligned envelope functions from cross-correlation.

We then use these times to search for the best-fitting location using a 0.5° $\times$

0.5° grid of points for the Antarctic region. We do not attempt to solve for source depth as we do not have any depth resolution. For each grid point, we follow four steps: (1) Calculate the predicted arrival time at each station based on a Rayleigh wave group velocity map at 50 s obtained from Guy Masters [personal communication, 2010]. (2) Find the differences between the observed and predicted times, $dt^i = T^i - T^i_\Delta$. (3) Find the median of these differences, which we treat as the offset to the origin time, $dT_0 = \text{median}(dt)$. (4) Use the L1 norm to find the location that minimizes the absolute value of the residuals, $r^i = dt^i - dT_0$.

The L1 norm for a vector $\mathbf{x}$ is $|\mathbf{x}| = \sum |x_i|$, and the L2 norm is $|\mathbf{x}| = \sqrt{\sum |x_i^2|}$. The L1 norm will reduce the effect of outliers compared with the L2 norm, so it is more robust for low signal-to-noise data. To estimate the statistical uncertainty in our locations we apply a bootstrap approach, in which we randomly resample the available stations and apply our method to get a new location. Repeating this 100 times provides 100 different location estimates, which we use to compute an approximate confidence ellipsoid.

2.3.2   Relative locations for each cluster

Our method relies on the fact that closely-located events will generate similar waveforms at each station. In this case, we can preserve the polarity and phase information and cross-correlate the bandpass-filtered waveforms themselves rather than their envelope functions. For each group, we relatively relocate events using the following procedure:

(1) For each pair of events, cross-correlate the waveforms at each station using a 20-minute window to get relative arrival times for each pair of events at a resampled time interval of 0.1 s. Figure 2.3 shows an example of the alignment of seismograms that can be achieved. (2) Use the individual event locations as starting locations. (3) Keeping the other event locations fixed at their current locations, search for the best new location for each event using a grid-search method that minimizes the L1-norm misfit of the predicted and observed differential times with respect to the other events. (4) Update all the locations, keeping the centroid of the cluster fixed. (5) Iterate on steps 3 and 4 until a stable set of locations is

obtained.

We use only waveform pairs with correlation coefficients of 0.5 or higher in the location procedure. Using this method, we obtain relative locations for our 13 events, within the three clusters. Both the absolute locations and relative locations are listed in Table 2.1. We estimate the errors in relative location to be about 1 degree, much less than the absolute location error ellipses plotted in the figures. For the Vanderford Glacier cluster, there is considerable nearby seismicity in 2007 and 2008 listed in the PDE catalog, with two events with magnitudes larger than 5, and there are two other cataloged events in 1984. Because these events are located using body-wave arrivals, their absolute location accuracy is likely better than what we can achieve using low signal-to-noise surface waves. Thus, we use a catalog event (M 5.7 on November 4, 2007), as a reference to relocate events within this cluster, and find that three of our events have surface waves that are correlated with this event at several stations. Of these three, the 2005 event lies within the zone of catalog seismicity, the 2001 event locates on the coast to the east of the cataloged events, and the 2002 event lies offshore, however, they are within our location error estimates. The estimated locations for these events are listed in Table 2.2.

2.4   Source mechanisms

Centroid single force (CSF) [*Kanamori and Given*, 1982; *Kawakatsu*, 1989] modeling for un-cataloged seismic events in Greenland has indicated horizontal force directions parallel to local ice flow directions [*Tsai and Ekström*, 2007]. These results suggest that such events are associated with horizontal ice mass movement along the expected ice flow directions. Although the CSF model achieved a higher variance reduction than standard centroid moment tensor (CMT) [*Dziewonski et al.*, 1981] solutions, it should be noted that the single force model cannot always be distinguished seismically from shallow dipping dip-slip faulting earthquakes [e.g., *Dahlen*, 1993]. When the source depth approaches zero for a dip-slip fault, the dominant components in a double-couple solution are M_{xz} and M_{yz} ($\vec{x}$: north,

$\vec{y}$: east, $\vec{z}$: vertical), which are usually poorly constrained in practice; thus a modified moment tensor solution using surface point forces is preferred [*Dahlen*, 1993]. The observed Rayleigh wave amplitude measured at 50 s exhibits a two-lobed radiation pattern, and the Love wave, although it typically has a lower signal-to-noise ratio than the Rayleigh wave, has predicted amplitudes comparable in size to the Rayleigh wave. These properties closely match the seismic radiation observed from the Mt. St. Helens landslide, which was analyzed with amplitudes measured at different frequencies in fitting a CSF model [*Kanamori and Given*, 1982]. The surface-wave signal for the new events is seen only between about 35 and 70 s period. The lack of observations at longer periods results in an unstable full waveform inversion; therefore, we will solve only for the best-fitting single-force horizontal directions for a shallow source that can explain our observed Love and Rayleigh wave amplitudes at 50 s.

To perform our analysis, we first obtain horizontal-component seismograms for the events (which were detected using only vertical component data) and rotate them to obtain the transverse and radial components. Next we Fourier transform the Love waves on the transverse component and the Rayleigh waves on both the vertical and radial components to obtain an amplitude spectrum. Then we select waveforms based on their signal-to-noise ratios to perform the inversion. We correct the amplitudes for attenuation and geometrical spreading using *Kanamori and Given* [1981]:

$$A(\omega, \phi) = A_\Delta e^{\omega a \phi / 2QU} \sqrt{\sin \theta} \qquad (2.1)$$

where A_Δ is the amplitude at each station before correction, a is the Earth radius, ϕ is azimuth, θ is the angular distance between source and station, Q is the effective inverse attenuation along the path , and U is the group velocity. We obtain Q and U estimates from the PREM model [*Dziewonski and Anderson*, 1981] at 50 s period for Love and Rayleigh waves. Numerical experiments showed that slight changes in Q and U do not affect the overall radiation pattern after the attenuation correction; therefore, we use the same value for all stations. For Love waves, Q is 120, U is 4.36 km/s; for Rayleigh waves, Q is 150, U is 3.887 km/s (the reference velocity in

our group velocity map). Surface-wave amplitudes at 50 s period are affected both by focusing and de-focusing caused by lateral velocity variations and by attenuation heterogeneity. We correct for both effects by computing an amplification factor using a global phase velocity and Q map for Rayleigh [*Dalton and Ekström*, 2006] and Love waves at 50 s period (C. Dalton, personal communication, 2010).

From *Kanamori and Given* [1982], we calculate predicted amplitudes for the Love and Rayleigh waves using:

$$A_L = P_L \omega f_0 \hat{s}(\omega) \cos \alpha \sin(\phi_f - \phi_s) \tag{2.2a}$$

$$A_R = P_R \omega f_0 \hat{s}(\omega) \cos \alpha \sqrt{\epsilon^2 + \cos(\phi_f - \phi_s)^2} \tag{2.2b}$$

where $f_0 \hat{s}(\omega)$ is the source term, ϕ_f and ϕ_s are the azimuths of the horizontal projection of the force direction and the station, α is the angle of the force from horizontal, P_L and P_R are the excitation functions of the Love and Rayleigh waves (which can be obtained from normal mode theory), ϵ describes the relationship between the vertical and horizontal force components, which we treat as a variable from 0 to 1. $f_0 \hat{s}(\omega)$ and α scale the amplitudes and cannot be resolved separately; we only solve for ϕ_f and ϵ. We normalize the observed and predicted amplitudes of the vertical and transverse components, and then search for the combination of ϕ_f and ϵ that minimizes their difference using the L1 norm. We do not attempt to solve for the absolute amplitude of the source (which trades off with α), only the orientation of the point force that best fits our observed azimuthal amplitude variations. Because we use only amplitude information (disregarding the phase of the signals), ϕ_f can only be determined modulo 180º, so our results have two possible directions: ϕ_f and $\phi_f + 180º$. Results are listed in Table 2.1 and Figure 2.4 shows a comparison between predicted and observed Rayleigh and Love wave amplitudes as a function of station azimuth. We obtain solutions for the 14 Grade B events. To estimate the uncertainty of these solutions, we apply a bootstrap approach similar to that used in the location uncertainty estimation, in which we resample available stations to get a new solution, repeat 100 times, and then estimate the uncertainty from the resulting 100 solutions. The bootstrap results

constrain the range of the inferred force directions to within about 15° as given in Table 2.1. We generally obtain similar force directions among the different events in the three regions, with the exception of an event in 2008 near Ninnis Glacier, which is also in a somewhat different location than other events in the same region.

Although the Rayleigh and Love wave amplitudes observed at individual stations exhibit considerable scatter, the overall amplitude patterns are well captured by our inversion as seen in Figure 2.4. To test our approach, we also computed synthetic seismograms using an assumed near horizontal thrust fault, which is equivalent to a single horizontal force model in that they generate the same slip vector for the hanging wall (the sliding mass in CSF model) [*Dahlen*, 1993]. Thus when the vertical slip component is nearly zero, we can link the resolved force direction ϕ (slip vector $\vec{d}(x,y) = (\cos\phi, \sin\phi)$) with rake λ (assumed equal to 90° for a thrust fault) and strike ϕ_f in a CMT solution:

$$\vec{d}(x,y) = \begin{cases} \cos\lambda\cos\phi_f + \sin\lambda\sin\phi_f \\ -\cos\lambda\sin\phi_f + \sin\lambda\cos\phi_f \end{cases} \tag{2.3}$$

We then compute synthetic waveforms by converting the force direction to strike for a near-horizontal thrust fault with a time constant of 50 s, and using a Green's function calculated from 0.010 to 0.030 Hz and filtered from 0.014 to 0.028 Hz. An example comparison for an event on June 27, 1999 is shown in Figure 2.5, and the synthetic waveforms agree well with the observed waveforms.

2.5   Glacier Dynamic Sources

Over 100 un-cataloged seismic events located near the coastline in Greenland were detected with global surface waves [*Ekström et al.*, 2003 and 2006]. Those seismic events are linked to calving events at glacier termini given their spatial and temporal correlations from seismic, satellite and GPS observations [*Amundson et al.*, 2008; *Joughin et al.*, 2008; *Nettles et al.*, 2008]. It should be noted that episodes of rapid glacier-sliding provide an alternative explanation for the seismic radiation and observed CSF mechanisms. However, an absence of the expected

glacier motion during the seismic events in Greenland argues against this mechanism [*Amundson et al.*, 2008; *Nettles et al.*, 2008], therefore, a calving mechanism is preferred. In Antarctica, teleseismically recorded tidally-modulated stick-slip events near the grounding line of the Whillans Ice Stream have been associated with glacier motion recorded by GPS [*Wiens et al.*, 2008]. However, the distinct nucleation and stopping phases noted by *Wiens et al.* [2008] are not observed in our seismic waveforms. Both our study and the earlier catalog of *Ekström* [2006] identify a small number of new events near the Antarctic coastline and near glacier termini at some locations [*Nettles and Ekström*, 2010]. This suggests that these events may originate from similar processes as the Greenland events.

The Greenland events have the following characteristics: (1) locations are near fast-flowing outlet glaciers; (2) waveforms are best fitted with the CSF model, indicating horizontal point forces; (3) inferred force directions are parallel to glacier flow [*Tsai and Ekström*, 2007]; (4) seasonal variations are correlated with local ice flow rate and calving variations [*Joughin et al.*, 2008; *Nettles et al.*, 2008; *Nettles and Ekström*, 2010]. However, some of these properties cannot be clearly established for our 17 Antarctic events. Due to the limited detections over 12 years, seasonal variations are not clear, with an almost equal number of events in winter and summer, and the relatively larger location uncertainties prevent a definitive association with glacier termini. For events on Ronne Ice Shelf, the inferred force directions are nearly parallel to the coast and at large angles to the local ice flow vectors. This is untypical for glacial earthquakes, whose single force directions are generally flow-parallel (e.g., *Tsai and Ekström*, 2007). We nevertheless suggest glaciological sources for these Antarctic events, because they locate near calving fronts and fast-flowing outlet glaciers (including regions of active rifting) and they are generally separated from regions of cataloged seismicity.

In order to further explore possible connections between glacier calving and our Antarctic events, we analyze images taken with the moderate resolution imaging spectroradiometer (MODIS) onboard NASA's Aqua and Terra satellites. On 250 m resolution images, we compare the Antarctic coastline in the regions of interest before and after our seismic events, confining ourselves to the 14 grade B

events. As no MODIS images are available before 2002, and darkness prevents imaging during the winter, we limit the image analysis to two events in the Vanderford Glacier region and two events in the Ninnis Glacier region.

In order to identify possible calving events as glacial earthquake sources, we manually digitize and then compare the coastline before and after the target events. For the four analyzed Antarctic events, the availability of cloud-free MODIS images substantially limits the temporal resolution with which we can identify calving events. We therefore use the following procedure: First, we use the closest available cloud-free image of the entire region of interest including all local fast-moving outlet glaciers within several hundred kilometers of coastline. For three of the four investigated seismic events, we identify coastline changes that may represent calving events. We then focus on these candidate locations using images taken as close to the seismic event origin times as possible. Land-fast sea ice can complicate interpretations, because it is often difficult to distinguish from land-sourced ice. In addition, owing to its coarse temporal resolution, our procedure can miss calving events, because ice flow may fill in the missing ice before a cloud-free, post-calving image becomes available. Nevertheless, our analysis does identify possible individual calving events as candidates for causing the seismic events and thus provides potential constraints on their source mechanisms.

2.5.1 Ronne Ice Shelf

Four of our events (all Grade B) are clustered towards the front of the Ronne Ice Shelf, near Hemmen Ice Rise (HIR) west of Berkner Island (BI) (Figure 2.7). All four events occurred in either June or August 1999 and their waveforms are well-correlated, indicating that they have similar source mechanisms. Their force directions are consistent, and are mostly well constrained as indicated by the bootstrap test. The event occurring at 20:00 on August 4, 1999 shows ambiguity in the force direction with two separate peaks in the bootstrap result, but synthetic waveforms show a better fit with the force direction at about 120°, consistent with the other three events. This region was the site of a large calving event in October 1998 (which produced icebergs A-38 and A-39) [*Lazzara et al.*, 2008], however, the

calving itself is not detected with our method probably due to the large tabular iceberg involved in the calving event instead of a capsizing iceberg. There are no high-resolution MODIS images available for this region during this time period. In contrast to the documented Greenland glacial earthquakes [e.g., *Nettles and Ekström*, 2010], the force directions are perpendicular to the background ice-shelf velocity vector. This argues against a typical calving generating mechanism. Instead, the force direction is parallel to the rift propagation direction (see Figure 2 of *Rignot and MacAyeal* [1998]). Rift-related icequakes have been observed to concentrate at the rift tip as well as distribute along the rift, but at magnitudes lower than 3 [*Bassis et al.*, 2007; *Winberry and Anandakrishnan*, 2003]. It is possible that our detected events are associated with the development of a new rift system after the calving event in 1998. The spatiotemporal distribution of the relocated events may relate to the development of different rifts in this region [*Larour et al.*, 2004]. However, the physics of how rift-related ice movements could generate observable long-period seismic energy is not clear.

2.5.2   Vanderford Glacier

Five of our events (all Grade B) cluster near the calving front of Vanderford Glacier in Wilkes Land. Vanderford Glacier is located in a deep subglacial trench and is bounded to its north by Law Dome (Figure 2.8). *Pritchard et al.* [2009] showed that this glacier is currently undergoing dynamic thinning (Figure S8 in *Pritchard et al.,* [2009]). There has recently been high cataloged seismicity near 67°S, 110°E, in 2007 and 2008: about twenty events occurred during those two years, compared to only two events recorded before 2007. Two M > 5 earthquakes occurred in November 2007 and July 2008, and there were also two magnitude 5 cataloged earthquakes on May 19, 1984. These events locate in the valley that connects Vanderford Glacier and separates the Law Dome ice cap from the East Antarctic ice sheet, farther inland than the coastal regions where our new events are located. The CMT solutions for larger events exhibit considerable variations and include a substantial non-double-couple component for the 1984 event. Only the July 2008 event has a shallow thrust faulting mechanism, matching the mecha-

nism for a possible landslide event. However, the fault orientation is not consistent with the ice-flow directions. Therefore, it is likely that these cataloged events are of tectonic origin and are unrelated to our Antarctic events. The new events locate along the East Antarctic coastline, and their force directions are consistent with local ice flow directions (I. Joughin, personal communication, 2009) at different locations. The agreement indicates these events may relate to ice dynamic processes, such as calving, basal sliding or stick-slip motion similar to those that have been observed from West Antarctica's ice streams [*Wiens et al.*, 2008].

For events (4) and (5) of the Vanderford region (Table 2.1), we identified calving events on the MODIS images as possible seismic sources. Figure 2.9 shows a pair of images taken ten days before and five days after event (4). The images clearly show evidence of a calving event that occurred between the images. The calving area amounts to about 1.5 km^2, approximately corresponding to the size of a nearby iceberg (red arrow). Figure 2.10 illustrates another calving event on the Vanderford ice front. The three images were taken one day before, seven minutes after, and eight days after the origin time of event (5). Little change is apparent between the first and second image. However, assuming that a major calving event coincided with event (5), we expect ice debris to occupy the calved terminus portion immediately after the event. Thus, as the second image was taken within a few minutes of our event origin time, it is unlikely to exhibit any changes at our 250 m resolution. On the other hand, the third image, taken about a week after the event, does show evidence for a calving event with an area of about 2 km^2. The locations and expected horizontal force directions are within our estimated source uncertainties, which further supports the association between the seismic events and calving episodes. The sizes of icebergs involved in the calving events are comparable to the size of icebergs involved in glacial earthquakes observed in Greenland [*Amundson et al.*, 2008]. Considering the proximity of other events in this region, it is likely that they originate from the same mechanism as events (4) and (5), however, the lack of MODIS images prevents additional investigation.

2.5.3   Ninnis Glacier

Eight of our events (five Grade B events and three Grade C events) locate on George V Coast, of which four Grade B events cluster between Ninnis Glacier and Cook Iceshelf, while one event lies to their west and offshore (Figure 2.11). The waveforms of the Grade C events have lower signal-to-noise ratios, preventing the more detailed analyses we performed for the Grade B events. Therefore, we do not have CSF solutions and refined locations for these three events. Four of the Grade B events near Ninnis Glacier show force directions consistent with the local ice flow directions (I. Joughin, personal communication, 2009), while the event to their west has a force direction nearly parallel to the coastline. The agreement between local ice flow directions and computed force directions strongly suggests that those events are related to glaciological processes. This region has complex bathymetry, with floating Ninnis and Mertz glacier tongues close to Ninnis Bank and Mertz Bank and numerous small-grounded icebergs and deformed stationary sea ice [*Massom*, 2003]. There was one major calving event from Ninnis Glacier in 2000 and a calving event from Mertz Glacier in 2010. The calving event in 2000 was from the floating Ninnis glacier tongue, and the complete development of the crack is a slow but gradual process, which took 10 years to complete [*Massom*, 2003], and likely did not generate any discrete events fast and energetic enough to be seen with our surface wave detector.

The offshore seismic event with a force direction parallel to the coast line is aligned with the westward ocean currents within the East Wind Drift zone [*Massom* 2003]. However, interactions between drifting icebergs and sea ice are not likely to produce a recordable seismic surface wave. One possible explanation for this event is crustal uplift due to post-glacial rebound. Figure 13 of *James and Ivins* [1998] and Figure 3 of *Kreemer and Holt* [2000] show that the expected crustal motion is at a similar direction to this event, suggesting a possible link between them. There was an Mw 8.0 earthquake 500 km off the coast near Balleny Island in March 1998, close to the plate boundary, but the fault plane and moment tensor solution suggest that this was an intraplate earthquake [*Nettles et al.*, 1999]. Some studies suggested that this large earthquake may be caused by post-glacial rebound [*Kreemer and*

Holt, 2000; *Tsuboi et al.*, 2000], and the fault plane orientation agrees with the modeled crustal response from deglaciation [*Kreemer and Holt*, 2000]. However, detailed strain field analysis is beyond the scope of this paper.

For Ninnis events (3) and (4) (Table 2.1) MODIS images of the coastline are available. Figure 2.13 shows an image pair of the Mertz Glacier tongue taken six days before and six days after the origin time of event (4). The images illustrate the breakup of a large portion of the sea ice attached to the glacier front. Furthermore, the ice tongue loses an area of 2 km^2 or more over this time period. It should be noted that our epicentral location for the corresponding event is almost 250 km to the southeast of the calving event, which is near the upper limit of the location error estimates. Nonetheless, the expected force direction from this calving event is consistent with our estimated force direction, supporting an association with the detected seismic event.

For Ninnis event (3) the images do not reveal calving events as clearly as the previously presented cases. Near the event's epicenter a large intact sea ice cover exists, which complicates identification of coastline changes. However, some cloud-free images reveal potentially relevant ice front changes for a small ice stream approximately 300 km west of the Mertz glacier (Figure 2.12), almost 550 km away from the calculated seismic epicenter. Whereas this large distance calls into question the role of this calving event in generating the seismic event, we could not identify any ice front changes closer to the epicenter. Figure 2.12A shows that three weeks before the origin time of event (3) an intact sea ice cover embraces the glacier's front. Within 16 days after the event, the sea ice cover has completely disappeared and several large icebergs have detached from the terminus (Figure 2.12D). Whereas the sea ice cover inhibits detailed inspection closer to the event origin time, it is clear that significant changes are happening between one day before (Figure 2.12B) and three days after (Figure 2.12C) the event origin time. It is possible that the image changes are caused by iceberg collision or capsizing, which have been suggested as glacial earthquake sources [*Amundson et al.*, 2008; *Tsai et al.*, 2008].

2.6 Discussion

Our observations suggest a variety of potential generating mechanisms for seismic events in Antarctica. The three calving events revealed by satellite images as well as the agreement between calculated horizontal force directions and ice flow directions suggest an association with the observed seismic events. The termini conditions for Antarctica events are different from previous reported seismic events in Greenland. The three calving events in Antarctica are from floating glacier tongues, while events in Greenland are mostly from grounded termini or near floating termini. A contact with the ocean floor provides force coupling with the solid Earth, and excites seismic energy at the observed periods [*Amundson et al.*, 2008; *Nettles and Ekström*, 2010]. Observations of glacial earthquakes in Antarctica are rare, and there are several known large calving events missing from our list, e.g., two major events in 1998 and 2000 from the Ronne Ice Shelf, two in 2000 from the Ross Ice Shelf [*Lazzara et al.*, 2008], and one in 2000 from Ninnis Glacier [*Massom*, 2003].

One possible reason for the different levels of detection between Greenland and Antarctica events can be attributed to differences in calving styles. Observations and mechanical modeling studies point out that capsizing icebergs interacting with surrounding ice mélange are able to produce effective horizontal forces at a $\sim$50 s time scale [*Tsai et al.*, 2008; *Amundson et al.*, 2010], and are therefore a preferred mechanism. Grounded tidewater glaciers predominantly produce relatively narrow icebergs prone to capsizing and thus are more likely to generate glacial earthquakes. For Jakobshavn Isbræ, in Western Greenland, for example, this style of calving occurs mostly during later spring and summer. In early spring, however, the glacier loses its floating tongue, which temporarily develops during the winter, via the calving of tabular icebergs. As these icebergs have larger horizontal dimensions than vertical, they do not capsize [*Amundson et al.*, 2010]. This latter calving style is "quiet" in that it does not produce substantial amounts of low-frequency seismicity [*Nettles and Ekström*, 2010]. Although calving off grounded termini is typical for temperate tidewater glaciers, the current conditions at Greenland's outlet glaciers as well as recent observations at Columbia Glacier [*Walter et al.*, 2010]

demonstrate that calving styles can spontaneously change. This may be a side effect of glacier thinning, terminus retreat into deeper water [*Walter et al.*, 2010] or changing ocean temperatures [*Holland et al.*, 2008; *Murray et al.*, 2010].

For floating Antarctic ice shelves, calving mass loss occurs mostly via large tabular icebergs [*Lazzara et al.*, 2008], which do not capsize and thus produce little low-frequency energy. Iceberg capsizing does play an important role during occasional ice shelf collapses as observed at the Larsen A and B Ice Shelves [*MacAyeal et al.*, 2003]. However, even such sudden ice shelf disintegration processes cause few or no glacial earthquakes [*Nettles and Ekström*, 2010]. This suggests that in addition to calving style, lack of seismic coupling to the Earth inhibits transmission of low-frequency seismic energy during calving events off floating ice fronts.

The present analysis of global seismograms and satellite images indicates that, although less frequently than in Greenland, Antarctic ice fronts occasionally calve capsizing icebergs, transferring low-frequency seismic energy into the Earth. For the three likely calving events identified from satellite imagery, the narrow and irregular shapes of the icebergs make it possible to produce capsizing icebergs during the calving process. For the Vanderford events, the geometry of the calved portion and its relative proximity to grounding lines (about 20 km, see Figure 2.9) may enable energy transmission to the solid Earth.

Similar to the mélange in Greenland's fjords, an intact sea ice cover near the calving fronts may play an important role during the generation of low-frequency seismicity. The Mertz glacier calving event pushed away part of the sea ice in front of the glacier tongue. The location of the calving event is close to Mertz Bank, with depths shallower than about 500 m and "trapped" small icebergs [*Massom*, 2003]. The presence of small icebergs and sea ice possibly provide resistant forces similar to ice mélange. Moreover, considering the thickness of Mertz Glacier is approximately 300 to 600 m [*Legrésy et al.*, 2004], the contact of a capsizing iceberg with the ocean floor is highly possible. However, a detailed mechanical force analysis for these calving events will require bathymetry and ice thickness data, as well as images with higher temporal resolution (our current temporal resolution is several days).

2.7   Conclusions

Our results, as well as those of *Ekström* [2006], show that global surface-wave detectors applied to continuous records from the global seismic network are capable of identifying hundreds of new seismic events that are not listed in existing earthquake catalogs. Most of these are tectonic earthquakes that are either too small, or radiate too little body-wave energy, to be detected using standard methods. However, there are also many seismic events detected in Greenland, which have been linked to calving events by several different studies [*Amundson et al.*, 2008; *Joughin et al.*, 2008; *Nettles et al.*, 2008], and a small number of seismic events in Antarctica. Due to their poor signal-to-noise and the sparse global station distribution near Antarctica, it is difficult to obtain accurate locations and resolve source mechanisms for those events. We use waveform-correlation and a global Rayleigh wave velocity model at 50 s to relocate these events, and find generally good agreement with glacier termini at Vanderford Glacier and Ninnis Glacier. Bootstrap resampling tests show that the horizontal force directions estimated using a CSF source model are well constrained. Satellite images link three seismic events with apparent calving events that are either close to grounding lines or surrounded by sea ice cover. Based on their locations, force directions, and satellite evidence, we associate events near Vanderford Glacier and Ninnis Glacier with calving events or other ice dynamic processes. However, one exception is the event in 2008 near Ninnis Glacier, which is best explained by post-glacial rebound. Events on the Ronne Ice Shelf are not near any fast-flowing glacier termini but are very close to rifts and islands, and are likely best explained by processes related to rift propagation, considering that their force directions are parallel to local rift directions. Detection of additional Antarctic events by local seismic networks would help to draw stronger conclusions, and complementary observation methods such as GPS, InSAR and satellite images with higher temporal resolution would aid in distinguishing between different generating mechanisms.

Acknowledgments

Chapter 2, in full, is a reformatted version of a publication in Journal of Geophysical Research: Chen, X., P. M. Shearer, F. Walter, and H. A. Fricker, Seventeen Antarctic seismic events detected by global surface waves and a possible link to calving events from satellite images, *J. Geophys. Res.*, 116, doi: 10.1029/2011JB008262, 2011. I was the primary investigator and author of the paper, which describes how we detected and located 17 events in Antarctica, and analyzed best-fitting force directions with the CSF model to understand the relationship between the events and glacier movement.

References

Amundson, J. M., M. Truffer, M. P. Lüthi, M. Fahnestock, M. West, and R. J. Motyka (2008), Glacier, fjord, and seismic response to recent large calving events, Jakobshavn Isbræ, Greenland, *Geophysical Research Letters, 35*, L22501, doi:10.1029/2008GL035281.

Amundson, J. M., M. Fahnestock, M. Truffer, J. Brown, M. P. Lüthi, and R. J. Motyka (2010), Ice mélange dynamics and implications for terminus stability, Jakobshavn Isbræ, Greenland, J. Geophys. Res., 115, F01005, doi:10.1029/2009JF001405.

Anandakrishnan, S and R. B. Alley (1997), Stagnation of ice stream C, West Antarctica by water piracy, *Geophys. Res. Lett.*, *24*(3), 265-268, doi: 10.1029/96gl04016

Bassis, J. N., H. A. Fricker, R. Coleman, Y. Bock, J. Behrens, D. Darnell, M. Okal,

and J. B. Minster (2007), Seismicity and deformation associated with ice-shelf rift propagation, *Journal of Glaciology, 53*(183), 523-536,

Dahlen, F. A. (1993), Single-force representation of shallow landslide sources, *Bulletin of the Seismological Society of America, 83*(1), 130-143.

Dalton, C. A., and G. Ekström (2006), Global models of surface-wave attenuation, *J. Geophys. Res., 111*, B05317, doi:10.1029/2005JB003997.

Danesi, S., S. Bannister, and A. Morelli (2007), Repeating earthquakes from rupture of an asperity under an Antarctic outlet glacier, *Earth and Planetary Science Letters, 253*(1-2), 151-158.

de Juan, J., P. Elósegui, M. Nettles, T. B. Larsen, J. L. Davis, G. S. Hamilton, L. A. Stearns, M. L. Andersen, G. Ekström, A. P. Ahlstrøm, L. Stenseng, S. A. Khan, and R. Forsberg (2010), Sudden increase in tidal response linked to calving and acceleration at a large Greenland outlet glacier, *Geophys. Res. Lett.*, 37, L12501, doi:10.1029/2010GL043289.

Dziewonski, A. M., and D. L. Anderson (1981), Preliminary reference Earth model, *Physics of The Earth and Planetary Interiors, 25*(4), 297-356.

Dziewonski, A. M., and T. A. Chou, J. H. Woodhouse (1981), Determination of earthquake source parameters from waveform data for studies of global and regional seismicity, *Journal of Geophysical Research, 86*(NB4), 2825-2852.

Ekström, G., M. Nettles, and G. A. Abers (2003), Glacial Earthquakes, *Science, 302*(5645), 622-624.

Ekström, G. (2006), Global Detection and Location of Seismic Sources by Using Surface Waves, *Bulletin of the Seismological Society of America, 96*(4A), 1201-1212.

Ekström, G., M. Nettles, and V. C. Tsai (2006), Seasonality and Increasing Frequency of Greenland Glacial Earthquakes, *Science, 311*(5768), 1756-1758.

Holland, P. R., A. Jenkins and D. M. Holland (2008), The response of ice shelf basal melting to variations in ocean temperature, *Journal of Climate, 21*(11), 2558-2572.

James, T. S., and E. R. Ivins (1995), Present-day Antarctic ice mass changes and crustal motion, *Geophysical Research Letters, 22*(8), 973-976.

James, T. S., and E. R. Ivins (1998), Predictions of Antarctic crustal motions driven by present-day ice sheet evolution and by isostatic memory of the Last Glacial Maximum, *Journal of Geophysical Research-Solid Earth, 103*(B3), 4993-5017.

Joughin, I. (2002), Ice-sheet velocity mapping: A combined interferometric and speckle-tracking approach, *Annals of Glaciology, 34*, 195-201.

Joughin, I., I. Howat, R. B. Alley, G. Ekström, M. Fahnestock, T. Moon, M. Nettles, M. Truffer, and V. C. Tsai (2008), Ice-front variation and tidewater behavior on Helheim and Kangerdlugssuaq Glaciers, Greenland, *J. Geophys. Res., 113*, F01004, doi:10.1029/2007JF000837.

Kanamori, H., and J. W. Given (1981), Use of Long-Period Surface-Waves for Rapid-Determination of Earthquake-Source Parameters, *Physics of The Earth and Planetary Interiors, 27*(1), 8-31.

Kanamori, H., and J. W. Given (1982), Analysis of long-period seismic waves excited by the May 18, 1980, eruption of Mount St. Helens: a terrestrial monopole, *J. Geophys. Res., 87*, 5422-5432.

Kawakatsu, H. (1989), Centroid single force inversion of seismic-waves generated by landslides, *J. Geophys. Res., 94*, 12363-12374

reemer, C., and W. E. Holt (2000), What caused the March 25, 1998 Antarctic plate earthquake?: Inferences from regional stress and strain rate fields, *Geophys. Res. Lett., 27*(15), 2297-2300.

Larour, E., E. Rignot, and D. Aubry (2004), Modelling of rift propagation on Ronne Ice Shelf, Antarctica, and sensitivity to climate change, *Geophys. Res. Lett., 31*, L16404, doi:10.1029/2004GL020077.

Lazzara, M. A., K. C. Jezek, T. A. Scambos, D. R. MacAyeal, and C. J. van der Veen (2008), On the recent calving of icebergs from the Ross Ice Shelf, *Polar Geography, 23*(3), 201-212.

Legrésy, B, A. Wendt, I. Tabacco, F. Rémy, and R. Dietrich (2004), Influence of tides and tidal current on Mertz Glacier, Antarctica, *J. Glaciology, 50*, 170.

MacAyeal, D. R., T. A. Scambos, C. I. Hulbe, and M. A. Fahnestock (2003), Catastrophic ice-shelf break-up by an ice-shelf-fragment-capsize mechanism, *J. Glaciology, 49*, 164.

Massom, R. A. (2003), Recent iceberg calving events in the Ninnis Glacier region, East Antarctica, *Antarctic Science, 15*(2), 303-313.

Murray, T., K. Scharrer, T. D. James, S. R. Dye, E. Hanna, A. D. Booth, N. Selmes, A. Luckman, A. L. C. Hughes, S. Cook and P. Huybrechts (2010), Ocean regulation hypothesis for glacier dynamics in southeast Greenland and implications for ice sheet mass changes, *J. Geophys. Res., 115*, F02026, doi:10.1029/2009JF001522.

Neave, K. G., and J. C. Savage (1970), Icequakes on the Athabasca Glacier, *J. Geophys. Res., 75*(8), 1351-1362.

Nettles, M., and T. C. Wallace, S. L. Beck (1999), The March 25, 1998 Antarctic plate earthquake, *Geophys. Res. Lett., 26*(14), 2097-2100

Nettles, M., and T. B. Larsen, P. Elósegui, G. S. Hamilton, L. A. Stearns, A. P. Ahlstrøm, J. L. Davis, M. L. Andersen, J. de Juan, S. A. Khan, L. Stenseng, G. Ekström, R. Forsberg (2008), Step-wise changes in glacier flow speed coincide with calving and glacial earthquakes at Helheim Glacier, Greenland, *Geophys. Res. Lett., 35*, L24503, doi:10.1029/2008GL036127.

Nettles, M., and G. Ekström (2010), Glacial earthquakes in Greenland and Antarctica, *Annu. Rev. Earth Planet. Sci. 2010., 38*, 467-91, doi: 10.1146/annurev-earth-040809-152414

O'Neel, S., H. P. Marshall, D. E. McNamara, and W. T. Pfeffer (2007), Seismic detection and analysis of icequakes at Columbia Glacier, Alaska, *Journal of Geophysical Research-Earth Surface, 112*, F03S23, doi:10.1029/2006JF000595.

Pritchard, H. D., R. J. Arthern, D. G. Vaughan, and L. A. Edwards (2009), Extensive dynamic thinning on the margins of the Greenland and Antarctic ice sheets, *Nature, advanced online publication*, doi:10.1038/nature08471.

Rignot, E., and D. R. MacAyeal (1998), Ice-shelf dynamics near the front of the Filchner-Ronne Ice Shelf, Antarctica, revealed by SAR interferometry, *Journal of Glaciology, 44(147),* 405-418.

Scambos, T. A., T. M. Haran, M. A. Fahnestock, T. H. Painter, and J. Bohlander (2007), MODIS-based Mosaic of Antarctica (MOA) data sets: Continent-wide surface morphology and snow grain size, *Remote Sensing of the Environment, 111*(2-3), 242-257, doi:10.1016/j.rse.2006.12.020.

Shearer, P.M. (1991), Imaging global body-wave phases by stacking long-period seismograms, *J. Geophys. Res., 96*(B12), 20353-20364.

Shearer, P. M. (1994), Global Seismic Event Detection Using a Matched-Filter on Long-Period Seismograms, *J. Geophys. Res., 99*(B7), 13713-13725.

Tsai, V. C., and G. Ekström (2007), Analysis of glacial earthquakes, *J. Geophys. Res., 112*, F03S22, doi:10.1029/2006JF000596.

Tsai, V. C., J. R. Rice, and M. Fahnestock (2008), Possible mechanisms for glacial earthquakes, *J. Geophys. Res., 113*, F03014, doi:10.1029/2007JF000944.

Tsuboi, S., M. Kikuchi, Y. Yamanaka, and M. Kanao (2000), The March 25, 1998 antarctic earthquake: Great earthquake caused by postglacial rebound, *Earth Planets and Space, 52*(2), 133-136.

Walter, F., J. F. Clinton, N. Deichmann, D. S. Dreger, S. E. Minson, and M. Funk (2009), Moment Tensor Inversions of Icequakes on Gornergletscher, Switzerland, *Bulletin of the Seismological Society of America, 99*(2A), 852-870.

Walter, F., S. O'Neel, D. McNamara, W. T. Pfeffer, J. N. Bassis, and H. A. Fricker (2010), Iceberg calving during transition from grounded to floating ice: Columbia Glacier, Alaska, *Geophysics Research Letters, 37*L15501, doi:10.1029/2010GL043201, 2010.

Wiens, D. A., S. Anandakrishnan, J. P. Winberry, and M. A. King (2008). Simultaneous teleseismic and geodetic observations of the stick-slip motion of an Antarctic ice stream, *Nature*, 435, 770-774, doi: 10.1038/nature06990.

Winberry, J. P., and S. Anandakrishnan (2003), Seismicity and neotectonics of West Antarctica, *Geophysical Research Letters, 30*(18), 1931, doi:10.1029/2003GL018001.

Table 2.1: Locations and CSF solutions for all events. Locations are in the format of (latitude, longitude)

Area name	index	Time	Absolute Location	Relative Location	CSF ($\phi_f(\sigma)$, $\epsilon(\sigma)$)	Ms
Ronne Ice Shelf	(1)	06/02/1999, 17:41:0.0	-78.4° , 310.4°	-78.1° , 310.5°	119° (2°), 0. (0.2)	4.53
	(2)	06/27/1999, 15:39:20.0	-77.5° , 311.1°	-77.7° , 310.2°	121° (3°), 0.25 (0.15)	4.56
	(3)	08/04/1999, 8:20:50.0	-77.2° , 311.3°	-77.3° , 310.3°	138° (0.8°), 0. (0.2)	4.36
	(4)	08/04/1999, 20:54:50.0	-77.4° , 308.6°	-77.4° , 310.4°	112° (25°), 0. (0.1)	4.33
Vander-ford Glacier	(1)	08/09/1997, 12:0:30.0	-67.3° , 109.0°	-66.8° , 109.5°	159° (2.5°), 0. (0.3)	4.28
	(2)	08/30/2001, 3:47:50.0	-66.1° , 108.9°	-66.5° , 110.4°	154° (1.8°), 0. (0.2)	4.51
	(3)	05/25/2002, 1:58:20.0	-66.6° , 112.6°	-66.7° , 110.1°	153° (4°), 0. (0.15)	4.34
	(4)	01/31/2004, 4:33:0.0	-66.4° , 110.5°	-66.8° , 110.3°	142° (8°), 0.35 (0.3)	4.24
	(5)	11/13/2005, 0:17:50.0	-67.4° , 109.5°	-67.0° , 110.2°	159° (5°), 0. (0.1)	4.39
Ninnis Glacier	(1)	04/04/1997, 12:20:30.0	-68.4° , 150.5°	-68.3° , 152.3°	35° (2°), 0 (0.3)	4.22
	(2)	03/14/1998, 10:35:30.0	-68.0° , 150.2°	-68.4° , 151.5°	10° (3°), 0 (0.13)	4.54
	(3)	01/24/2004, 8:40:30.0	-68.1° , 152.9°	-68.2° , 150.0°	24° (10°), 0. (0.15)	4.37
	(4)	11/02/2007, 10:2:50.0	-68.7° , 149.8°	-68.3° , 149.6°	30° (3°), 0.2 (0.1)	4.52
	(5)	06/18/2008, 0:5:30.0	-68.6° , 157.9°	N/A	87° (12°), 0. (0.3)	4.55
Grade C events	C1	03/02/2005, 21:28:0	-67.2° , 136.5°	N/A	N/A	N/A
	C2	05/25/2005, 14:10:40	-72.5° , 142.6°	N/A	N/A	N/A
	C3	05/14/2007, 13:46:30	-72.5° , 155.5°	N/A	N/A	N/A

Table 2.2: Locations relative to Mw 5.7 event on 11/04/2007 at (-67.27° , 111.53°)

Time	Location (latitude, longitude)
08/30/2001, 3:47:50.0	-66.90° , 108.95°
11/13/2005, 0:17:50.0	-67.00° , 111.50°
05/25/2002, 1:58:20.0	-65.25° , 107.00°
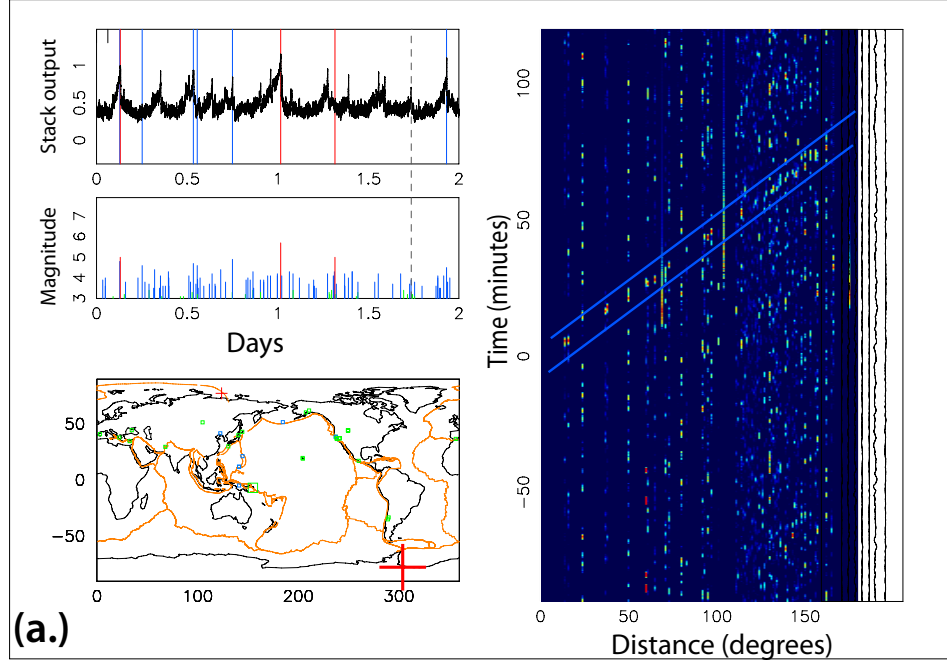
Figure 2.1: Examples from the GUI display for checking detected events. (a) Grade B event in Antarctica, June 2, 1999; (b) Grade C event in Antarctica, May 14, 2007. In both figures, the upper left panel displays the output of our detector in a 2-day interval, with peaks indicating the times of likely events. The red and blue lines show detected (associated) catalog events of M>5 and M>3.5, respectively. The dashed line shows the time of an unassociated peak selected by the user for examination. The right panel shows a record section plot of seismograms for an assumed event at the time of this peak and the best-fitting location given by the algorithm, the different colors indicate the amplitude of the stacked seismograms, red means high amplitude while dark means low amplitude. The blue lines indicate the predicted Rayleigh wave arrivals. This location is plotted as the large red cross in the map view, which also shows catalog events within 120 minutes of the target event as squares (blue means the time offset is less than 30 minutes, and green means the time offset is between 30 and 120 minutes). The small red cross shows the target event antipode. The middle left panel shows catalog event magnitudes. Figure continued on the following page.
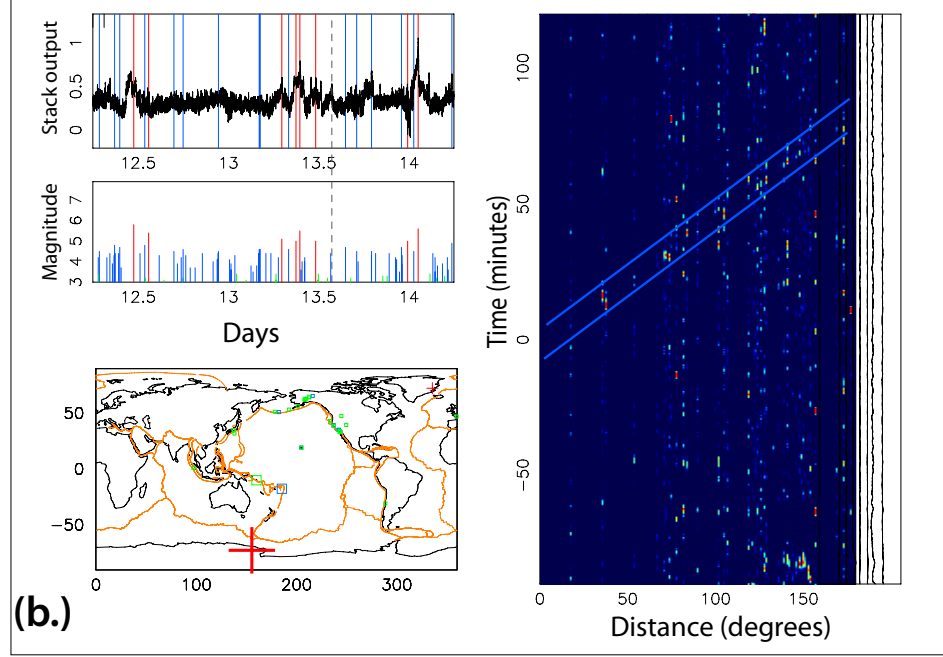
Figure 2.1: Figure continued from previous page. Examples from the GUI display for checking detected events. (a) Grade B event in Antarctica, June 2, 1999; (b) Grade C event in Antarctica, May 14, 2007. In both figures, the upper left panel displays the output of our detector in a 2-day interval, with peaks indicating the times of likely events. The red and 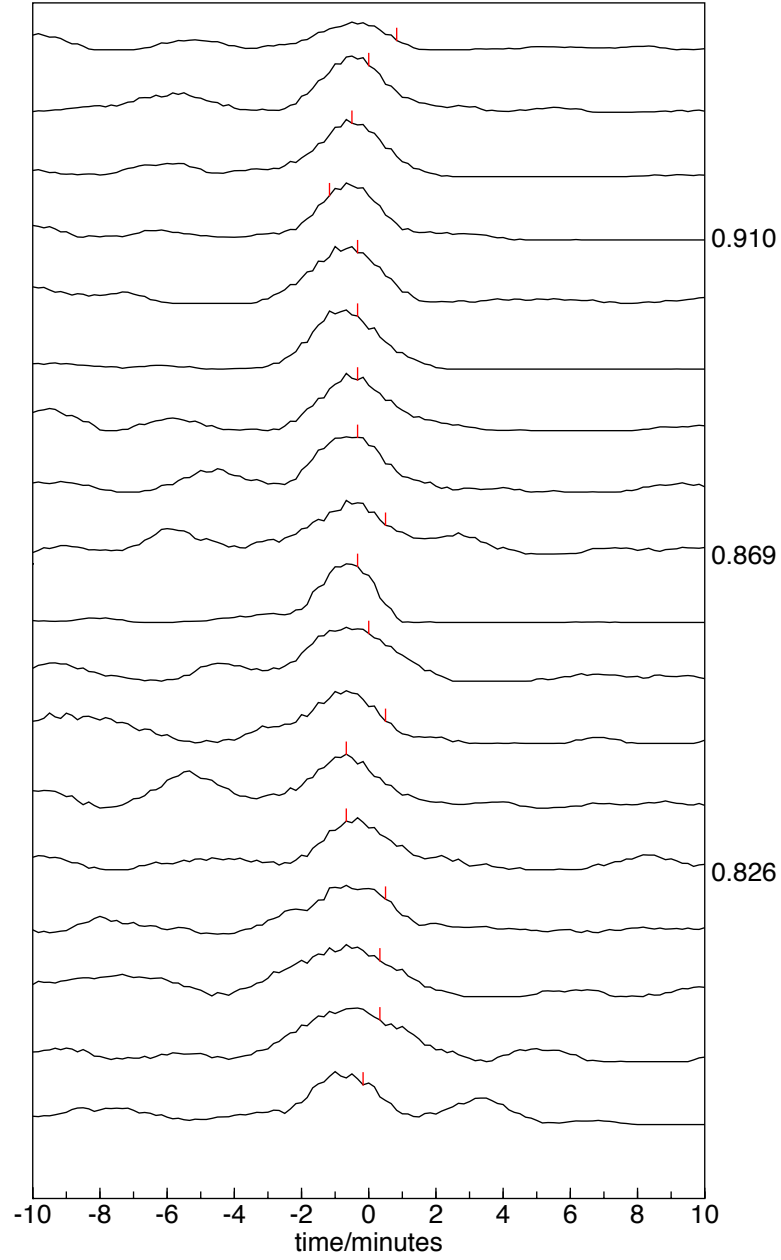blue lines show detected (associated) catalog events of M>5 and M>3.5, respectively. The dashed line shows the time of an unassociated peak selected by the user for examination. The right panel shows a record section plot of seismograms for an assumed event at the time of this peak and the best-fitting location given by the algorithm, the different colors indicate the amplitude of the stacked seismograms, red means high amplitude while dark means low amplitude. The blue lines indicate the predicted Rayleigh wave arrivals. This location is plotted as the large red cross in the map view, which also shows catalog events within 120 minutes of the target event as squares (blue means the time offset is less than 30 minutes, and green means the time offset is between 30 and 120 minutes). The small red cross shows the target event antipode. The middle left panel shows catalog event magnitudes.

Figure 2.2: Envelope functions calculated from the STA/LTA filter aligned using our cross-correlation method for an event in Antarctica occurring on June 27, 1999. Red ticks indicate predicted arrival times at the original location. Traces are sorted by correlation coefficient (plotted at right) between the traces and a weighted stack of all the traces (see text).
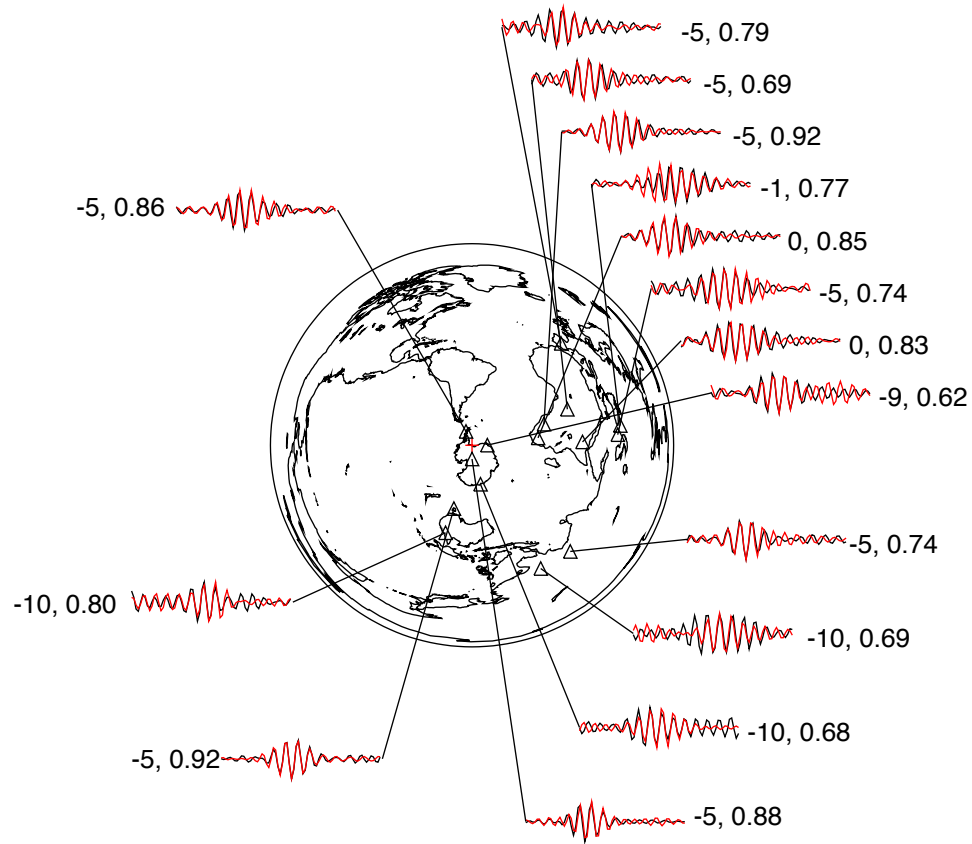
Figure 2.3: Waveform comparison between two events on the Ronne Ice Shelf. Each time series is 700 s (70 samples) long. The black line is for an event on June 2, 1999; the red line is for an event on June 27, 1999. The first number shows the time shifts in samples (10 s per sample) necessary to align the traces; the second number is the correlation coefficient between the two traces.
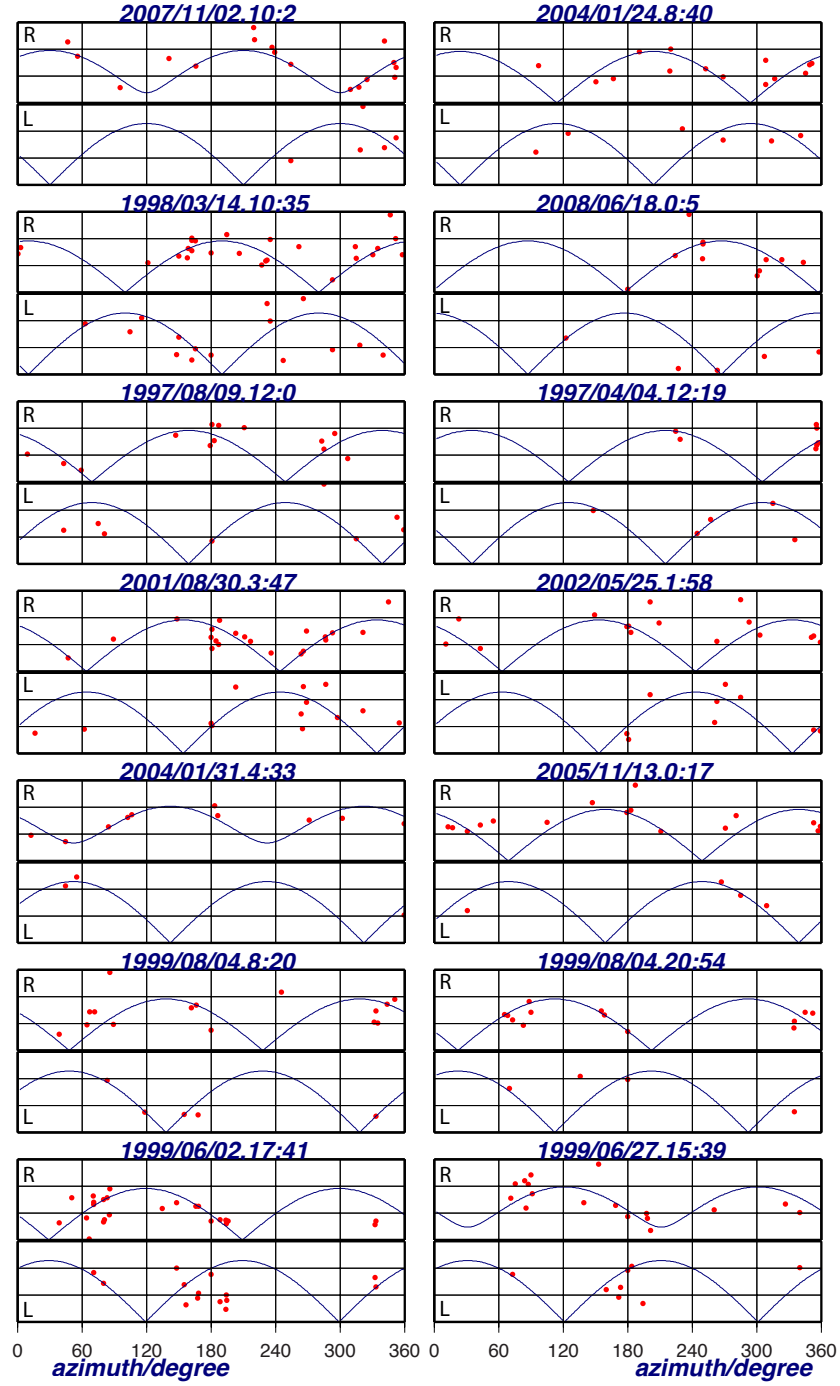
Figure 2.4: Observed versus predicted amplitudes from a centroid single force (CSF) model. Red dots are observed amplitudes; blue lines are predicted amplitudes using our method. Only relative amplitudes are plotted. "R" indicates Rayleigh wave, "L" indicates Love wave.
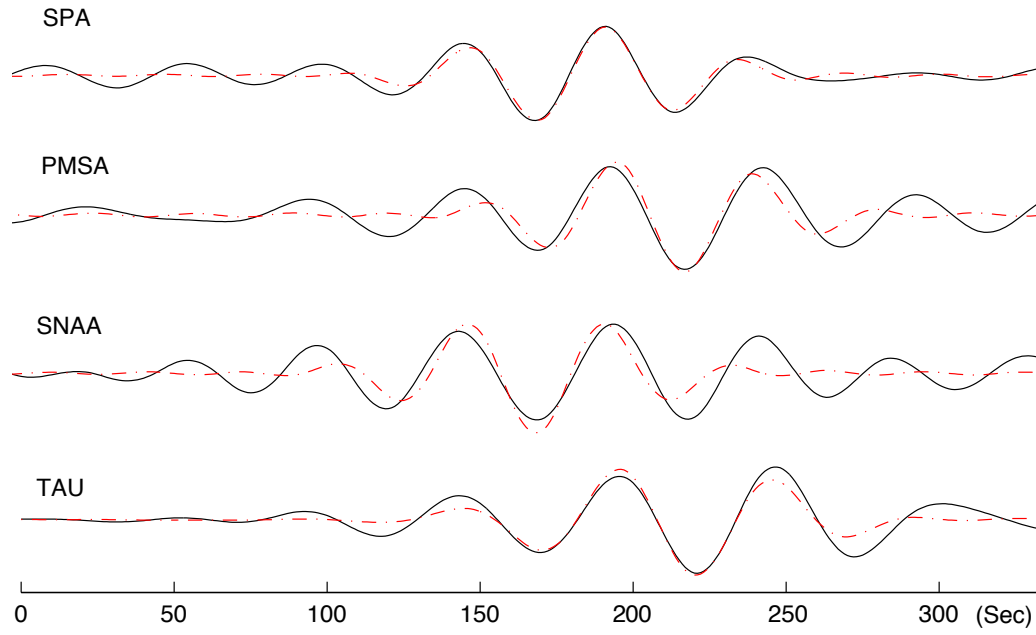
Figure 2.5: Synthetic waveforms (dashed line) versus recorded waveforms (solid line) at four stations on the "VHZ" channel for a June 27, 1999, event on the Ronne Ice Shelf. Waveforms are filtered between 0.014 Hz and 0.028 Hz. Synthetic waveforms are generated with an equivalent double-couple source instead of CSF source.
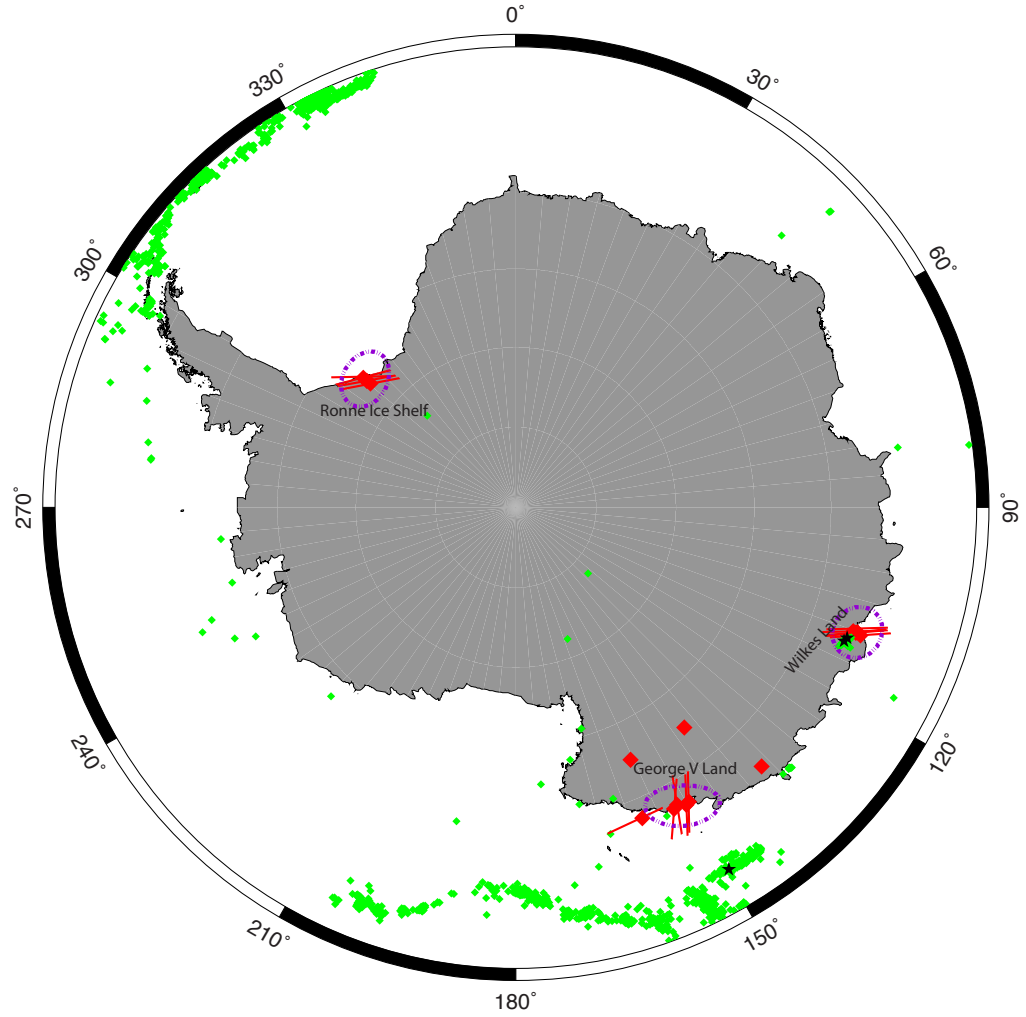
Figure 2.6: Antarctic map with our new events (red) and existing catalog events (green). Black stars are catalog events greater than M 5. The red lines are our computed force directions. Purple circles are 95% absolute location uncertainties.
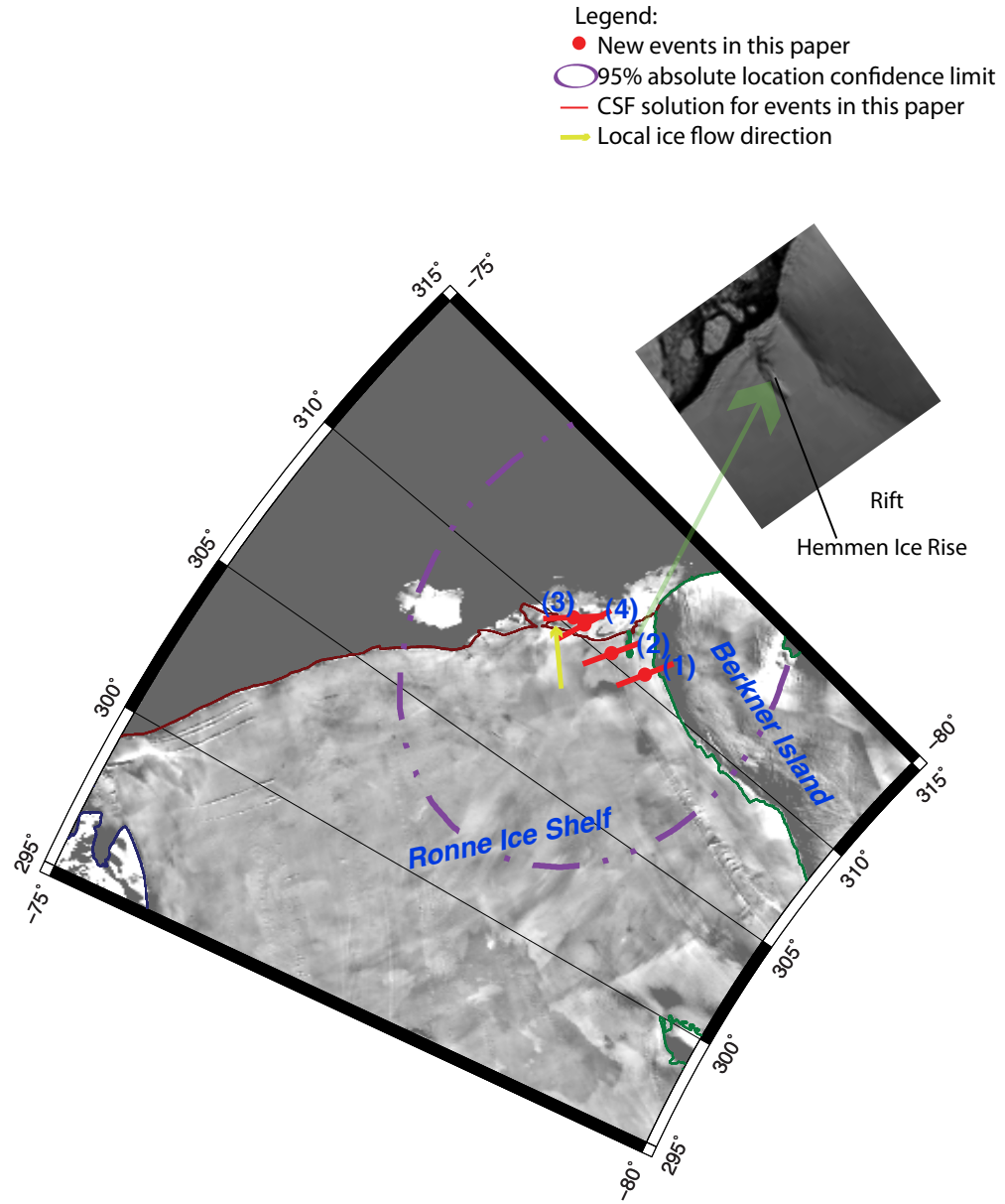
Figure 2.7: Map for events in the Ronne Ice Shelf. The background is the MOA image with 60% transparency, solid grey is ocean. The red line is the ice front, the green line delimits islands and ice rises. A close-up of a rift and the Hemmen Ice Rise are shown in the MOA satellite image. Index numbers of events in each region correspond to events in Table 2.1. Coastline and grounding lines are from *Scambos et al.* [2007].
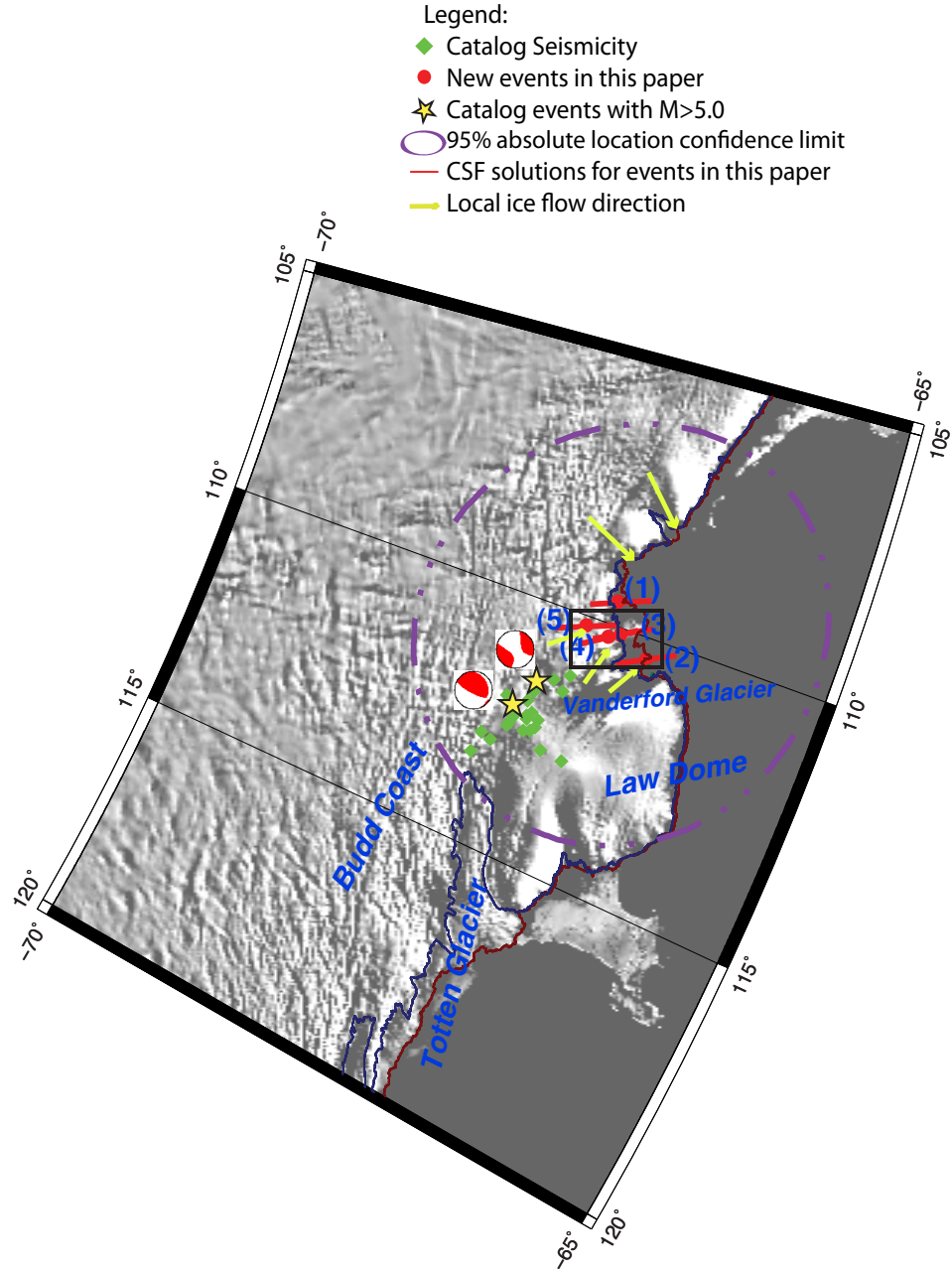
Figure 2.8: Map for events near Vanderford Glacier. The background is the MOA image with 60% transparency, solid grey is ocean. The blue line is the glacier grounding line; the red line is the ice front. Index numbers of events in each region correspond to events in Table 2.1. Coastline and grounding lines are from *Scambos et al.* [2007]. The black box indicates the approximate locations of MODIS images in Figure 2.9 and 2.10. Moment tensor solutions for two M≥5 catalog events are from the Global CMT project.
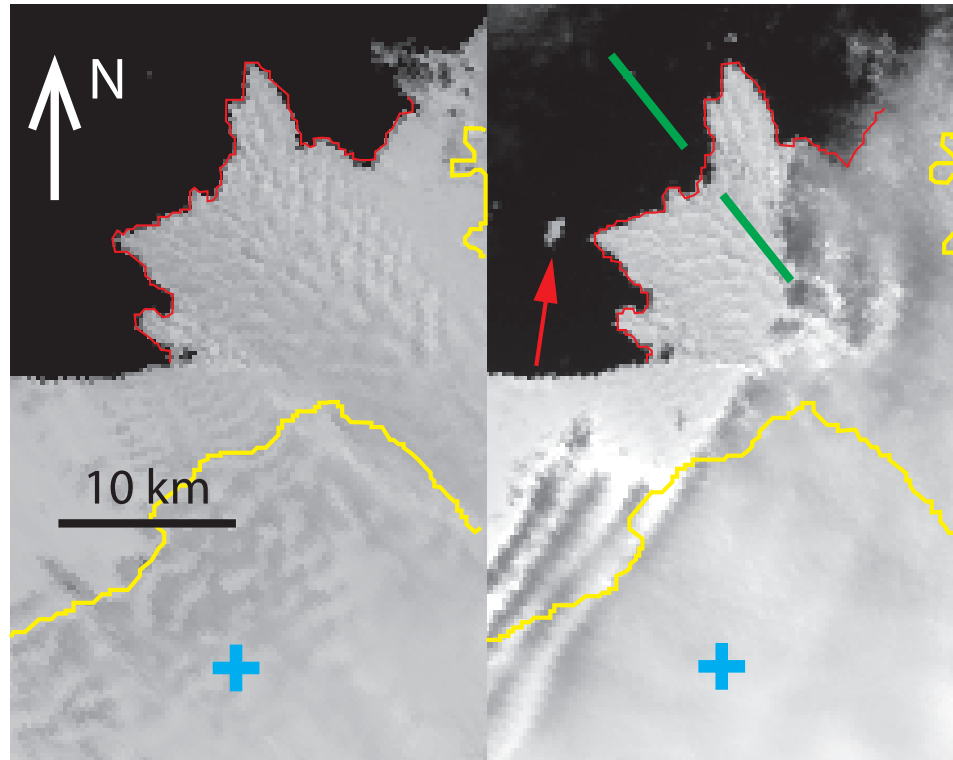
Figure 2.9: MODIS images depicting a calving event as a possible source for event 4 in the Vanderford region (Table 2.1). The images were taken on January 21 and February 5, 2004, ten days before and five days after the event origin time, respectively. The red line traces the pre-calving ice front, whereas the yellow line marks the ice sheet grounding line [*Scambos et al.* 2007]. The cyan cross indicates the nominal seismic event location (the entire image is within the location error ellipse) and the green lines show the estimated horizontal force directions (±180°). The red arrow points to an iceberg, which likely detached during the calving event.
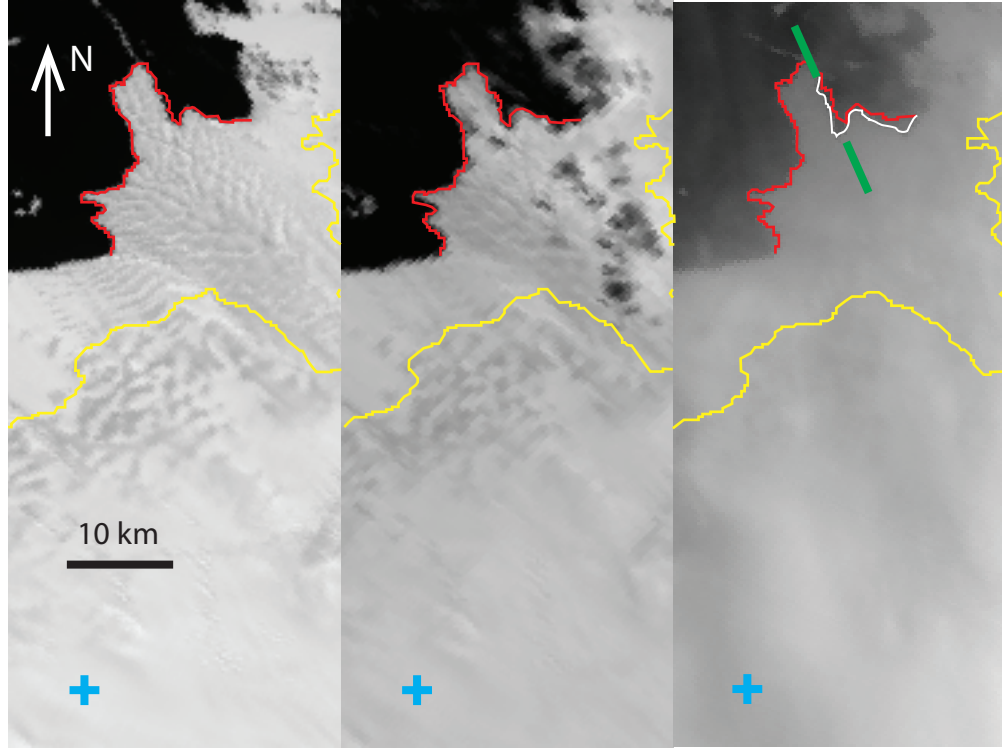
Figure 2.10: MODIS images depicting a calving event as a possible source for event 5 in the Vanderford region (Table 2.1). The images were taken on November 12, November 13, and November 21, 2005. This corresponds to one day before, seven minutes after, and eight days after the event origin time. The red line traces the pre-calving ice front, whereas the yellow line marks the ice sheet grounding line [*Scambos et al.* 2007]. Due to poor lightening, a white line is added to the right figure tracing the after-calving ice front, to better highlight the calving event. The cyan cross indicates the nominal seismic event location (the entire image is within the location error ellipse) and the green lines show the estimated horizontal force directions (±180°).
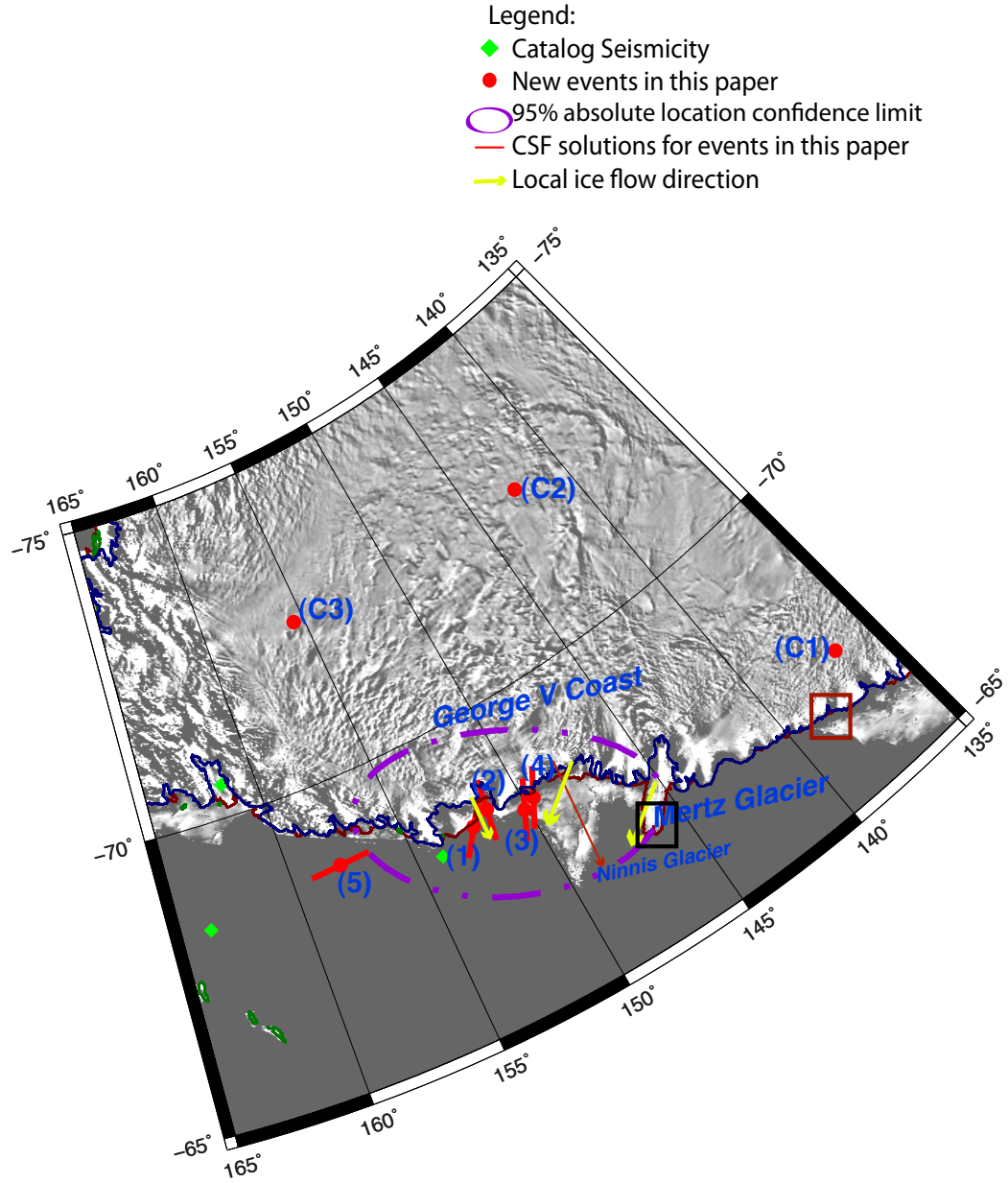
Figure 2.11: Map for events near Ninnis Glacier. The background is the MOA image with 60% transparency, solid grey is ocean. The blue line is the glacier grounding line; the red line is the ice front. Index numbers of events in each region correspond to events in Table 2.1. Coastline and grounding lines are from *Scambos et al.* [2007]. The red box indicates the approximate location of MODIS images in Figure 2.12. The black box indicates the approximate location of images in Figure 2.13.
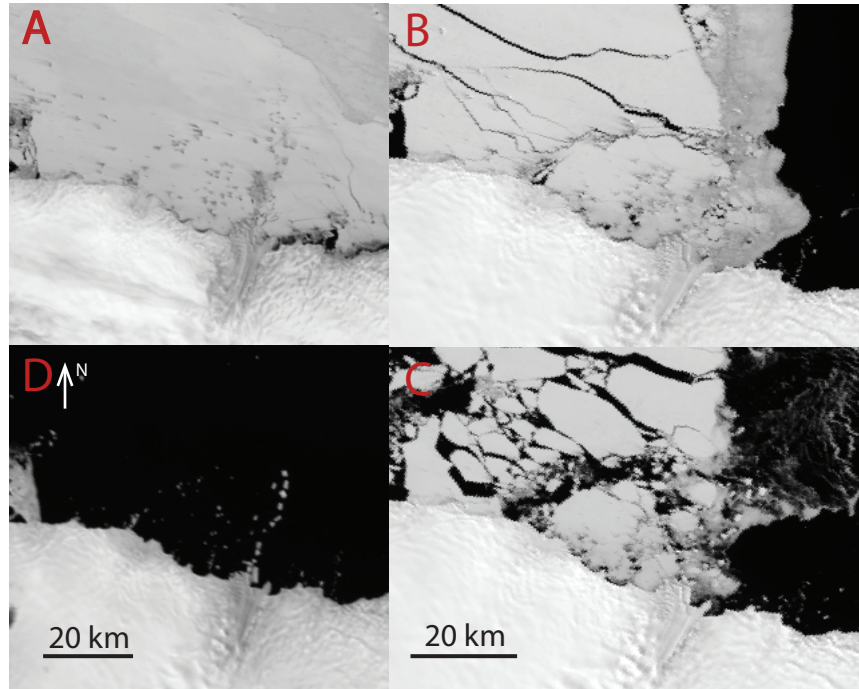
Figure 2.12: MODIS images of a changing glacier tongue in the Ninnis region. The images were taken on January 2, 2004 (A; 22 days before the calving event), January 23 (B; one day before the calving event), January 27 (C; four days after the calving event) and February 9 (D; 16 days after the calving event). This ice front locates almost 550 km away from the calculated seismic epicenter making the association between glacial earthquake and depicted ice front changes somewhat speculative.
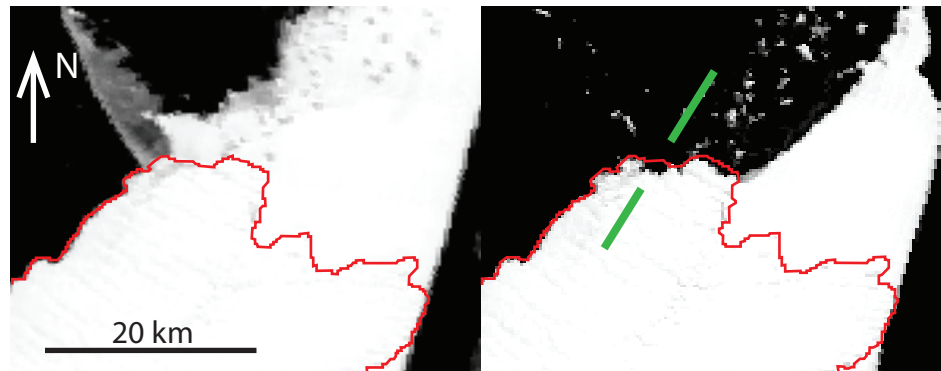
Figure 2.13: MODIS images depicting a calving event as a possible source for event 4 in the Ninnis region (Table 2.1). The images were taken on October 27 and November 8, 2004, six days before and six days after the event origin time, respectively. The red line traces the pre-calving ice front. The epicentral location is about 250 km to the southeast. The green lines show the estimated horizontal force directions ($\pm 180°$).

Chapter 3

Comprehensive analysis of earthquake source spectra and swarms in the Salton Trough, California

We study earthquakes within California's Salton Trough from 1981 to 2009 from a precisely relocated catalog. We process the seismic waveforms to isolate source spectra, station spectra and travel-time dependent spectra. The results suggest an average P-wave Q of 340, agreeing with previous results indicating relatively high attenuation in the Salton Trough. Stress drops estimated from the source spectra using an empirical Green's function (EGF) method reveal large scatter among individual events but a low median stress drop of 0.56 MPa for the region. The distribution of stress drop after applying a spatial-median filter indicates lower stress drops near geothermal sites. We explore the relationships between seismicity, stress drops and geothermal injection activities. Seismicity within the Salton Trough shows strong spatial clustering, with 20 distinct earthquake swarms with at least 50 events. They can be separated into early-$M_{\max}$ and late-$M_{\max}$ groups based on the normalized occurrence time of their largest event. These swarms generally have a low skew value of moment release history,

ranging from -9 to 3.0. The major temporal difference between the two groups is the excess of seismicity and an inverse power-law increase of seismicity before the largest event for the late-M_{max} group. All swarms exhibit spatial migration of seismicity at a statistical significance greater than 85%. A weighted L1-norm inversion of linear migration parameters yields migration velocities from 0.008 to 0.8 km/hour. To explore the influence of fluid injection in geothermal sites, we also model the migration behavior with the diffusion equation, and obtain a hydraulic diffusion coefficient of approximately 0.25 m^2/s for the Salton Sea geothermal site, which is within the range of expected values for a typical geothermal reservoir. The swarms with migration velocities over 0.1 km/hour cannot be explained by the diffusion curve, rather, their velocity is consistent with the propagation velocity of creep and slow slip events. These variations in migration behavior allow us to distinguish among different driving processes.

3.1   Introduction

The SAF (San Andreas Fault) to IF (Imperial Fault) step-over produces regional extension and block rotation within the Salton Trough. The newly discovered hinge zone by *Brothers et al.* [2009] marks the northern limit of active extension and separates the Salton Sea into two sub-basins. High surface temperatures are found along the southern shoreline of the Salton Sea where a buried spreading center is located and maximum subsidence occurs [*Schmitt and Hulen*, 2008; *Svensen et al.*, 2009; *Brothers et al.*, 2009]. The northern end of the Imperial Fault defines a separate subsidence pull-apart basin, the Mesquite Basin [*Brothers et al.*, 2009]. High seismicity is found within the rapidly subsiding basins, whereas the seismicity in the Brawley seismic zone exhibits a ladder-like pattern consistent with block rotation. There are two major geothermal sites in the study region: the Salton Sea geothermal site (at the southern end of the Salton Sea), and the Brawley geothermal site (within the Brawley Seismic Zone).

Previous studies have noted that this region has lower Brune-type stress drops compared to other areas of California, possibly due to high heat flow [*Shearer*

et al., 2006]. Spatial variations of stress drop may reflect the relative strength of fault zones, for example, in the San Andreas Fault zone lower stress drops are found along the creeping section compared to the locked section [*Allmann and Shearer*, 2007]. In order to accurately estimate stress drops from body-wave spectra, the source spectrum needs to be deconvolved from propagation path effects. This is typically done using the empirical Green's function (EGF) method. The traditional approach of estimating the EGF from nearby smaller earthquakes generally requires these events to be at least one magnitude unit smaller than the target event [*Hough and Kanamori*, 2002]. The fact that multiple events are recorded at many stations provides an alternative way to isolate the source spectrum using stacking and a multi-event EGF method [*Shearer et al.*, 2006]. This method allows us to study both earthquake source parameters and lateral variations in attenuation. Here we extend the *Shearer et al.* [2006] results to a much longer time interval, obtaining stress drop estimates from 1981 to 2009, to study the anomalously low stress drops in the Salton Trough in detail.

Researchers have noted that regions with higher heat flow tend to have more seismic swarms than mainshock-aftershock sequences [*Enescu et al.*, 2009] and swarms are often observed in volcanic regions [*Farrell et al.*, 2009; *Fischer*, 2003; *Hayashi and Morita*, 2003]. Most seismic swarms appear driven by an underlying physical change, such as fluid migration or slow slip, and often exhibit spatial migration behavior [*Hayashi and Morita*, 2003; *Lohman and McGuire*, 2007]. A study of the 2000 Vogtland swarm revealed evidence for magma intrusion during the swarm activity from ETAS (epidemic type aftershock sequence) modeling [*Hainzl and Ogata*, 2005]. There have been three well-documented large swarms in 1981, 2005 and 2009 in the Salton Trough. InSar and GPS measurements suggest that the 2005 swarm was driven by aseismic slip along the northeast direction [*Lohman and McGuire*, 2007]. In addition to the three large swarms, there have been many smaller swarm episodes. Here we analyze the migration behavior for a more complete list of swarms and identify preferred migration directions that appear related to the stress orientation. We also estimate migration velocities, which can be used to estimate hypothetical fluid diffusion rates. These results help to

clarify the relationship between the material properties and tectonics in the Salton Trough and its ongoing seismicity.

3.2   Data and processing

Shearer et al. [2006] studied P-wave source spectra for earthquakes in southern California from 1989 to 2001, a period when the seismic network was relatively stable in terms of instrumentation. They obtained stress drop values for over 60,000 events and found spatially coherent patterns in average stress drop, with generally higher values for the eastern Transverse ranges and lower stress drops in the Salton Trough region. In order to make a comprehensive analysis of stress drops in the Salton Trough, we analyze earthquake source spectra for events from 1981 to 2009. We select 14,197 events within our study region (shown by green box in Figure 3.1) from a precisely relocated catalog (G. Lin, personal communication 2009) obtained using the method described in *Lin et al.* [2007b]. We then obtain the event waveforms archived at the Southern California Earthquake Data Center, which are filtered to a uniform 100 Hz sampling rate. Displacement spectra are computed with 1.28 s windows starting at the picked P arrival times (operator pick if available, otherwise an autopick). Spectra are selected for analysis that have P-wave signal-to-noise ratios (SNR) ≥ 3 for frequency bands of 5 to 10 Hz, 10 to 15 Hz, and 15 to 20 Hz. Event source spectra E_i, station terms S_j and travel-time path spectra $T_{k(i,j)}$ are separated from displacement spectra using the iterative robust-mean method from *Shearer et al.* [2006] using the equation:

$$D_{ij} = E_i + S_j + T_{k(i,j)} + R_{ij} \tag{3.1}$$

At each station, there is usually more than one trace for each component since we use different channels, so we solve for a separate station term for each channel. For the same channel, there might be station term changes during the period from 1981 to 2009 owing to instrumental changes, which often show up as changes in sample rate. We identify systematic changes in resolved parameters from the whole database without considering station term changes and separate them into

three periods: 1981 to 1985, 1985 to 1988 and 1988 to 2010. During each period, we find the sample rate for each channel at each station, and solve for a separate station term for each sample rate. We use an iterative robust least squares method [*Shearer et al.*, 2006] to isolate event terms, station terms and travel-time terms. In this processing, we solve for a total of 9397 event terms and 503 station terms.

3.3 Stress drop

The stress drop $\Delta\sigma$ can be estimated from the event term E_i. To consider only the best-resolved events, we restrict our analysis to the 3332 events with P-wave spectra stacked from at least five different stations that satisfy our SNR criteria. Our computed event terms only provide relative spectral shapes among different events and include common path effects that cannot be isolated from travel-time terms. To obtain absolute spectral shapes, we apply the multiple-event empirical Green's function (EGF) method used in *Shearer et al.* [2006] to all of our events. We calibrate the measured relative seismic moment Ω_0 to the absolute moment M_0 using the local magnitude M_L by fitting a linear relationship between $\log(\Omega_0)$ and M_L: $M_L = 1.0 \log_{10}\Omega_0 + 2.19$. We limit our analysis to events with magnitudes lower than 3.5 due to amplitudes "clipping" for larger events.

The source spectra are stacked at 0.2 increments in calibrated-magnitude bins. We first solve for a single regional EGF by fitting a theoretical source model for binned spectra with magnitudes from 1.5 to 2.9, for which all the binned stacked spectra are reasonably smooth. The theoretical spectral model used here was first proposed by *Brune* [1970]:

$$u(f) = \frac{\Omega_0}{1 + (f/f_c)^2} \tag{3.2}$$

where Ω_0 is the long-period amplitude and f_c is the corner frequency. The P-wave corner frequency f_c can be related to stress drop $\Delta\sigma$ by using the *Madariaga* [1976] relation:

$$f_c = \frac{0.42\beta}{(M_0/\Delta\sigma)^{1/3}} \tag{3.3}$$

where β is shear-wave velocity (assumed to be 3.5 km/s). We use the method in *Shearer et al.* [2006] to find the best fitting stress drop and the EGF. Next, we correct the individual source spectra by subtracting the EGF, find the best-fitting corner frequency f_c for each event, and compute $\Delta\sigma$ from equation (3.3). The individual event stress drops exhibit considerable variation but have a median value around 0.5 MPa.

By correcting the event spectra with a single EGF, we are implicitly assuming a uniform attenuation model for the whole region. However, there exists the possibility of lateral variations in material properties which could cause quakes in regions of higher local attenuation than the assumed model to have lower measured corner frequencies and inferred stress drops. For example, *Shearer et al.* [2006] noted that events in the Coso geothermal field have increased stress drops after considering a spatially variable EGF model, and *Allmann and Shearer* [2007] found that an observed temporal variation of stress drops before and after the 2004 Parkfield earthquake can be partially accounted for by a change in attenuation.

In order to test for the effect of possible spatial variations in attenuation, we use a multiple-EGF method to solve for a separate EGF for each individual event using only the closest nearby events. The seismicity is unevenly distributed in this region, with relatively few events near Bombay Beach in the Salton Sea and the Brawley geothermal site, whereas intensive seismicity is found within the Salton Sea geothermal field and the Mesquite Basin region. Considering this difference, we use at least 100 closest neighboring events for each event in the lower seismicity regions, and events within a 2 km radius for each event in the higher seismicity regions. We solve for an EGF for each event using the same procedure as was applied earlier for all events and the same magnitude range. Then the corner frequency and stress drop are calculated from the EGF-corrected source spectrum.

The resulting stress drops after correction for attenuation effects reflects the variations among event source spectra and may indicate the relative strength of fault zones. The individual-event stress drops follow a normal distribution in the log-domain with a median value of 0.56 MPa and values ranging from 0.1 MPa to 3.7 MPa. However, there is a clustering of poorly resolved high stress

drops and high corner frequency events, which is probably due to the lower SNR cutoff and the limited frequency band used in the inversion. As in the case of the constant EGF analysis, individual stress drops have considerable variation and we apply the spatial-median filter by finding the median value for 100 closest events to resolve spatial variations in average stress drop (Figure 3.2b). Note that because of the minimum signal-to-noise criteria for the spectra, stress estimates are obtained for only 25% of the seismicity in the region (3332 out of 14,197 events). We observe spatial variations in median stress drop, with lower stress drops near the southern coast of the Salton Sea and the Brawley geothermal field, whereas higher stress drops are found toward the boundary of the active extension zone. We find that the smoothed spatially coherent pattern is robust regardless of the choice of the number of neighboring events, and thus reflects source property changes among the different regions. The overall distribution of stress drops is much lower than that found for Southern California earthquakes from 1989 to 2001 [*Shearer et al.*, 2006], suggesting relatively weaker fault zones in the Salton Trough. Similar to *Shearer et al.* [2006], we observe no relationship between stress drop and magnitude, suggesting self-similarity among different sized events. We do not observe any clear relationship with depth, probably because the seismicity is confined to a narrow depth zone within each area and any systematic depth variation in stress drop may be masked by larger variations between regions.

3.4   Attenuation

Using a single EGF, we can compute an average P-wave attenuation quality factor (Q_P) for the Salton Trough region from the travel time terms. In order to be consistent with equation (3.1), we add the computed EGF and the travel-time term to get the true path spectra. We assume that the theoretical spectrum for attenuation is:

$$A_k = A_0 e^{-\omega t(k)/2Q_P} \tag{3.4}$$

In the log domain, the spectrum has a linear relationship with frequency. A best-fitting Q_P of 340 is found for the Salton Trough region, substantially lower than the average value of 560 found for all of southern California by *Shearer et al.* [2006]. This result is consistent with the high attenuation observed in the Salton Trough region by *Schlotterbeck and Abers* [2001] and *Hauksson and Shearer* [2006].

The difference in results between the new multiple EGF approach and the single EGF method can be related to changes in the attenuation parameter t^* (an integrated measure of the attenuation along the raypath: $t^* = \int_s Q_P^{-1} dt$). We obtain Δt^* by least-square fitting to the spectra ratio between the two EGFs in the log domain, a positive Δt^* indicates an increase in attenuation compared to the regional average. As shown in Figure 3.3, increased attenuation with Δt^* of 0.008 s is seen within the newly identified hinge zone within the Salton Sea, the southern coast of the Salton Sea, and the Mesquite Basin, where rapid subsidence and sedimentation is suggested [*Brothers et al.*, 2009]. A crustal tomography map reveals low-velocity anomalies beneath the southern Salton Sea and west of the Imperial Fault at seismogenic depths [*Lin et al.*, 2007a; *Schmitt and Hulen*, 2008], thus higher attenuation in these regions might be expected. Overall, 90% of our observed P-wave Δt^* are from -0.006 to 0.008 s. Using the average travel time of 10 s considered in the travel-time spectra, these variations correspond to Q_P ranging from about 280 to 410, although larger variations are expected for localized anomalies.

3.5 Geothermal activities

Relatively lower stress drop values (by approximately 0.12 MPa or about 20% lower than the median) are observed within the geothermal areas, including the southern coast of the Salton Sea and the Brawley geothermal field. The highest seismicity rate in the Salton Trough is seen within the Salton Sea geothermal field where continuous injection and production activities have been conducted since 1982. Injection-induced seismicity has been observed in several geothermal reservoirs in an effort to create an EGS (enhanced geothermal system) to increase

the permeability of the material or fluid content [*Majer et al.*, 2007]. One well-known example is the Geysers geothermal area in northern California. Although the situation in the Salton Sea is different from the HDR (hot-dry-rock) type reservoir of the Geysers [*Majer et al.*, 2007], since the Salton region is already fluid-rich and the injection activities are mainly for water circulation purposes [*Goldsmith*, 1976; *Lin et al.*, 2007], the increased pore pressure during injection can trigger earthquakes if the fault zones are near-critical due to reduced effective stress [*Goertz-Allmann et al.*, 2011].

To understand the possible relationship between seismicity and geothermal activities in this region, we focused on a 7 km NE cross-section (see Figure 3.4 and 3.5), where about 50% of the total seismicity is located. The cross-section view (Figure 3.4b) shows that the seismicity clustered into three major separated areas, where each area spans a depth range of about 4 km. The vertical distribution of seismicity is similar to other geothermal sites, i.e., the Geysers [*Ross et al.*, 1999]. The locations of the three clusters correlate with the location of injection wells (see Figure 3.5), and the initiation of high seismicity coincides with the start of injection activities (see Figure 3.5b and 3.5c). It should be noted that Figure 3.4 only includes events with stress drop estimates, while Figure 3.5 includes all events with magnitude greater than 1.0, regardless of their stress drop estimates.

To further analyze the relationship between stress drop and distance from geothermal wells, for all events occurring after the start of geothermal activities in the Salton Trough (first record was in 1982), we find the distance to the nearest injection well for each event. We then sort the events according to their distance to the nearest injection wells, and separate them into 10 bins, each with an equal number of events. We find the median stress drop and distance for each bin, and apply a bootstrap method (with resampling) to estimate uncertainties in the median stress drop. Shown in Figure 3.6, the median stress drop increases with distance from the injection wells to about 2.5 km, a radius which includes about 55% of the events. Beyond 2.5 km, the increasing relationship is not clear, which is probably due to reduced fluid influence at greater distance. Similar relationships have been observed by *Goertz-Allmann et al.* [2011], who found the stress drop

increases with pore pressure for up to 300 m within a geothermal reservoir in Switzerland and suggest that reduced effective stress due to increased pore pressure could explain the relationship.

3.6   Swarm activity

Statistical simulations of earthquake clusters using ETAS triggering models [e.g., *Ogata*, 1988] show a higher probability of seismic swarms in regions with higher heat flow and geothermal activities [*Enescu et al.*, 2009]. There have been three major swarms of hundreds of events in the Salton Trough region since 1981. The swarms in 1981 and 2005 were associated with aseismic slip [*Lohman and McGuire*, 2007] and exhibited spatial migration along the cross-section direction (see Figure 3.7 and 3.8). The swarms in 1981 and 2005 start with low stress drop events, evolving to higher stress drops near the time of the largest earthquake in the sequence (see Figure 3.7 and 3.8). The variation of stress drops within each swarm is similar to the pattern of stress drop increase with distance from geothermal wells.

In addition to the major swarms, there have been a number of smaller swarms in the Salton region, likely promoted by the relatively high flow. To study swarm properties in more detail and possibly relate them to tectonic features, we have complied a more complete list of swarms. We begin by searching for seismic 'bursts' using similar criteria as *Vidale and Shearer* [2006], who found 71 seismic bursts in Southern California. We require: (1) there are at least 50 events within a radius of 4 km in 14 days following the initial event; (2) no more than 20% of the events occur between 4 and 8 km from the initial event during the same 14 days; (3) there are fewer than 5 events in the prior 14 days within the same 4 km radius. Using these criteria, we identify 34 seismic bursts, which include some clusters with seismicity distributed within separate distinct areas within the 4 km radius. Visual examination of the spatial and temporal distributions of each burst shows that several bursts are subsets of the 1981 and 2005 swarm groups (the spatial extent and duration of which are beyond our burst selection criteria),

and we associate these bursts to the larger swarms. After visual examination, we identify 20 distinct bursts or burst groups. Although in principle these bursts could include simple mainshock-aftershock sequences, we find that all of them exhibit swarm-like behavior to some extent. Thus we will henceforth refer to them simply as swarms rather than bursts, although we recognize that some are more 'swarm-like' than others. The location and time of each swarm is shown in Figure 3.9. These swarms span two separate periods, from 1981 to 1987 and from 1999 to 2009 (see Figure 3.9). They tend to cluster in four major regions: near Bombay Beach, the southern shoreline of the Salton Sea, the middle Brawley Seismic Zone, and the northern end of the Imperial Fault. Most of the swarm seismicity is distributed between 0 and 10 km depth, with shallower events in the north and deeper events near the Imperial Fault (see Figure 3.9b).

3.6.1 Temporal behavior

For each swarm, we normalize the time for each event since the beginning of the sequence by the mean time delay: $t_i = (T_i - T_0)/mean(T_i - T_0, i = 1...N)$. Next we consider the normalized timing of the largest event in the sequence, t_{max}. We classify 6 swarms with $t_{max} \leq 0.4$ as early-$M_{\max}$ (more similar to mainshock-aftershock sequences) and 14 swarms with $t_{max} \geq 0.6$ as late-$M_{\max}$ (more swarm like). We use the skew of moment release history $F(t) = \int_{t_0}^{t} M_0 \, dt$ to further quantify the difference between early-$M_{\max}$ and late-$M_{\max}$ swarms. As described in *Roland and McGuire* [2009], a larger positive value is observed for pure aftershock sequences ($t_{max} = 0$) while a lower or even negative value is observed for swarms (which generally have larger t_{max}). For each event, the moment is estimated from the catalog magnitude: $M_0(i) = 10^{(1.5*M_L(i)+9.1)}$ (N-m). We do not use the calibrated magnitudes estimated from the spectral analysis because it did not include all the events. The centroid time of moment release is obtained from the weighted mean time: $\bar{t} = \frac{\sum_1^N t_i \times M_0(i)}{\sum_1^N M_0(i)}$. Individual moment is normalized by $m_0(i) = \frac{M_0(i)}{\sum_1^N M_0(i)}$ so that $F(t \rightarrow \infty) = 1$. The third central moment of this sequence is: $\mu_3 = \sum_1^N (t_i - \bar{t})^3 m_0(i)$, the standard deviation: $\sigma = \sqrt{\sum_1^N (t_i - \bar{t})^2 m_0(i)}$. The skew of moment release of each sequence is

$skew = \mu_3/\sigma^3$. The skew values for the early-$M_{\max}$ group are mostly above 1.8 with one exception at -0.29, the late-$M_{\max}$ groups have values between -9 and 1.5, generally lower than the other group. Although the early-$M_{\max}$ sequences usually have higher skew values, all the values fall within the range for swarm-like sequences in *Vidale and Shearer* [2006], from -5 to 5 [*Roland and McGuire*, 2009].

Next, we examine the temporal distribution of events by checking the seismicity decay rate. The observed decay rate for most aftershock sequences follows t^{-p}, that is Omori's Law [*Omori*, 1895], where p is typically close to unity. For each sequence, we compare the time history of seismicity relative to the largest event with $\sim t^{-1}$ predictions. Our results for individual sequences show a variety of patterns that often exhibit a mixture of swarm-like and aftershock-like behavior. To analyze the general features, we stack the seismicity rate within each group according to event time relative to the largest event in each sequence. For the late-$M_{\max}$ group, to limit the effect of large sequences, we consider separately the three bursts with more than 400 events and the eleven bursts with fewer than 200 events. Shown in Figure 3.10, the highest seismicity rate occurred near the time of the largest event, and later seismicity followed a power-law decay. The major difference lies in the events before the largest event: the late-$M_{\max}$ group (Figure 3.10a, b) has nearly as much seismicity leading up to the largest event as occurs later, while the early-$M_{\max}$ group has very few early events and behaves more like a mainshock-aftershock sequence. For the three largest swarms, event subclusters occurred about 30 hours before the peak subcluster, and the two subclusters within each burst occurred at different faults due to the large spatial extent of the bursts (Figure 3.9a).

Figure 3.10b shows a power-law increasing trend of seismicity before the occurrence of the largest event. The post-peak decay is described by Omori's Law; while the pre-peak buildup is sometimes called inverse Omori's Law. Similar temporal distributions are observed for simulated swarm activity based on a self-organization model [*Hainzl*, 2003], and the 2000 Vogtland swarm in Bohemia, which is suggested to have been triggered by fluid intrusion and driven by post-seismic creep [*Hainzl*, 2004]. Therefore, the temporal distribution of activity indicates

there is possible fluid involvement in the triggering mechanism for swarms in the late-$M_{\max}$ group.

3.6.2 Spatial distribution

Most swarms except the three largest are confined to a narrow region. Following *Vidale and Shearer* [2006], we find the eigenvalues and eigenvectors for the covarience matrix of demeaned hypocentral coordinates of the events within each swarm. For the three large swarms, the events break up into smaller clusters and we use visual inspection to study separately the spatial distribution for each area. The relative sizes of the eigenvalues define the general shape of the cluster, with $\lambda_1 >> \lambda_2, \lambda_3$ for a linear distribution, $\lambda_1 \approx \lambda_2 >> \lambda_3$ for a planar distribution, and $\lambda_1 \approx \lambda_2 \approx \lambda_3$ for a spherical distribution. We find that most bursts are linearly distributed along strike, or on a nearly vertical fault plane, while four of them show spherical distributions. Similar to *Vidale and Shearer* [2006], we find that the best fitting planes are mostly near vertical with dip angles ranging from $65°$ to $89°$ with the majority greater than $80°$. Most smaller swarms are distributed within a narrow depth range of 1 km, and extend longer distances along strike. General information for each swarm, including its temporal and spatial distribution is listed in Table 3.1.

3.6.3 Spatial-temporal migration

In an initial visual examination, we plot occurrence time versus distance along strike, and find that all our observed bursts exhibit seismicity migration. This is in contrast to typical mainshock-aftershock sequences, which usually do not exhibit spatial migration behavior [*Vidale and Shearer*, 2006], they tend to occur across the entire aftershock region immediately after the mainshock. In addition, the magnitude difference between the largest event within even the early-$M_{\max}$ group and the next largest event is usually less than 0.3, far lower than the Båth's Law average value of 1.2 [*Båth*, 1965], and the skew values are lower than typical aftershock sequences [*Roland and McGuire* 2009]. This is why we refer to all 20 of

our observed bursts as swarms, rather than aftershock sequences.

In order to quantify swarm migration behavior, we develop a weighted L1-norm method to find the best-fitting migration vector. Observations suggest that the seismicity front is migrating with time, and plots of event time versus distance along the migration direction exhibit an upper triangle shape. Thus we need to weight the misfit between predicted and observed times in a way that accounts for this behavior to obtain robust inversion results. We consider two types of migration:

$$\text{unilateral}: s_0(\vec{s} \cdot (\vec{X}_i - \vec{X}_0)) + t_0 = t_i \tag{3.5a}$$

$$\text{bilateral}: s_0 |\vec{s} \cdot (\vec{X}_i - \vec{X}_0)| + t_0 = t_i \tag{3.5b}$$

in which s_0 is the migration slowness ($s_0 = 1/v_0$, where v_0 is velocity), $\vec{s}$ is the unit migration direction vector, $\vec{X}_i$ are the 3-D coordinates for each event, $\vec{X}_0$ is the starting location for migration, t_0 is the starting time of migration, and t_i is the occurrence time of each event. We use a grid search approach over θ, ϕ, $\vec{X}_0$, v_0, and t_0 to find the best fitting parameters (see Appendix A for details). To estimate the statistical significance of the migration and uncertainties for migration parameters, we use a bootstrap resampling method (see Appendix B).

We find that most swarms migrate with probability greater than 95%, with a few having lower probabilities between 85% and 90%. The parameters θ and ϕ tend to trade off with each other since they are included in the inversion of the unit migration vector, so they usually have a larger variation range. A better approach is to estimate the total angular uncertainty in the migration directions, and the swarms usually have uncertainty estimates ranging from 10° to 20°. Migration modeling results for 20 swarms are listed in Table 3.2. The migration velocities range from 0.008 to 0.8 km/hour, with about 65% below 0.1 km/hour, lower than typical creep rates and aseismic slip rates [*Lohman and McGuire*, 2007; *Roland and McGuire*, 2009]. There is considerable scatter in plots of event time versus distance for individual swarms. To better show the overall migration features, we combine results from all the swarms by plotting event time versus normalized distance (distance/v_0 where v_0 is the estimated migration velocity) in Figure 4.1a. Notice

again the upper triangular nature of the migration behavior, in which activity continues for some time following its onset at a given location.

The linear migration behavior is consistent with the assumption that aseismic slip (slow slip or creep) propagates along pre-fractured fault zones, modifies the localized stress field and triggers seismicity. However, as shown in Figure 3.5, some events are possibly induced seismicity from geothermal activities. The temporal distribution for the late-$M_{\max}$ group is also similar to swarms triggered by a fluid intrusion process [*Hainzl*, 2003]. Considering that swarms within the geothermal fields generally have migration velocities slower than typical aseismic slip rates, and their proximity to injection wells, it is possible that their migration behavior is controlled by fluid diffusion. In this case, instead of linear migration, the fluid-triggered seismicity front should follow the diffusion curve: $r = \sqrt{4\pi D t}$, where D is the diffusion coefficient and r is the distance for each event from the initiating point of fluid intrusion. The migration of induced seismicity away from injection wells has been used in different regions to estimate the hydraulic diffusion of the medium [*Audigane et al.* 2002; *Shapiro et al.* 2005].

In order to explore possible fluid involvement, we find the best-fitting diffusion coefficient by modeling $r^2 = 4\pi D(t - t_0)$ using a similar fitting procedure to that used for linear migration. We also use a bootstrap approach to estimate the statistical significance of the migration parameters. We find four of the swarms, and the initial 100 hours for the swarm in 1981, are better fit with a diffusion curve than with linear migration. The results are listed in Table 3.3. Figure 4.1b shows event time versus normalized distance (i.e., divided by $\sqrt{4\pi D}$) for these four swarms and the fit of the diffusion curve to the seismicity front. The estimated diffusion coefficients range from 0.2 to 0.6 m^2/s, within the range of values for reservoirs [*Shapiro et al.* 2005]. The swarms are located within the Salton Sea and Brawley geothermal fields, close to geothermal wells, especially the three swarms that occurred within active injection periods. The physically reasonable diffusion coefficients we obtain and the timing related to injection activities suggest that fluid movement is involved in the propagation of seismicity.

3.6.4   Stress drop and migration

As shown in Figures 3.7c and 3.8c, in some cases there is an increase of average stress drop with time as the swarm evolves. To find the relationship between stress drop and migration for other swarms, we divided events within each swarm into 8 bins with equal number of events, and found the median stress drop and time for each bin. The results exhibit a great deal of scatter and there is no clear trend of average stress drop with time. We also compared the stress drop values for swarm events with nearby non-swarm events but found no significant difference. Nonetheless, there are some variations in average stress drop among the different swarms. Swarms with migration velocities lower than 0.1 km/hour are mostly located within the lower stress drop regions, and their median stress drop is 0.25 MPa lower than swarms with faster migration velocities. This observation agrees with the results shown in Figure 3.6, since most of the slower migrating swarms are located within the Salton Sea geothermal field (see Figure 3.12), where stress drops are lower than average.

3.6.5   Migration and tectonics

The swarms are distributed in four distinct regions: (1) the southern end of the SAF (the newly discovered hinge zone that separates the Salton Sea into northern and southern sub-basins), (2) the southern shoreline of the Salton Sea (geothermal field), (3) the middle of the Brawley Seismic Zone (Brawley geothermal field), and (4) the northern end of the Imperial Fault (Mesquite basin). We refer to these regions by number in the following text. The major migration direction is NE-SW (around $45° \pm 180°$), and there are two swarms migrating at a faster velocity along the SAF parallel direction (NNW-SSE, around $145° \pm 180°$) (see Figure 3.12b).

The general NE-SW direction changes from N60°E in region 4 to N30°E in region 1. The more northern trend in the Salton Sea was also noticed in *Brothers et al.* [2009]. The migration behaviors are different among the four clustered regions, which may be related to differences in material properties and the regional stress field. We plot the focal mechanism solutions from the SCSN (Southern California

Seismic Network) moment tensor group and *Hardebeck and Shearer* [2005] to compare with the migration directions, shown in Figure 3.12. A parameter f_{type} from -1 (normal) to 0 (strike-slip) to 1 (reverse) is computed for each event based on the method in *Shearer et al.* [2006]. The majority of events involve strike-slip faulting, and the beach ball orientations generally agree with the migration direction in each region. Several normal faulting events are seen along the southern coast of the Salton Sea and the Mesquite Basin, consistent with the expected source mechanism for rapid subsidence regions.

Region 1 marks the northern end of active extension and agrees with a hinge zone discovered by a seismic reflection survey [*Brothers et al.*, 2009]. The 2009 swarm exhibits complex migration behavior. It ruptured three parallel NE striking faults and the seismicity migrated both bilaterally along the NE direction at each fault and unilaterally along the NNW direction from the northernmost fault to the southernmost fault. The 2009 swarm is encompassed within a region of increased Coulomb stress resulting from the slip transient that occurred within the southern Salton Sea from 2003 to 2009 [*Crowell et al.*, 2009], indicating an aseismic process is involved. The 2001 swarm unilaterally migrated along the NNE direction, which agrees with the fault plane of its largest event and the N15° E striking faults imaged during the seismic survey [*Brothers et al.*, 2009]. The 1985 swarm is confined to a narrow linear fracture zone and migrates along the SAF fault strike direction at a velocity around 0.3 km/hour, close to the propagation velocity of creep events and slow earthquake sequences on the SAF [*Linde et al.*, 1996; *King et al.* 1973; *Burford* 1977], and thus is most likely triggered by aseismic slip.

The highest seismicity rate and most of the swarms occurred in region 2. Shown in Figures 3.5 and 3.6, as well as the diffusion modeling plotted in Figure 4.1b, the seismicity clustering and migration are at least partially controlled by geothermal injection/production activities. The NE-SW migrating swarms follow the first installation of geothermal injection wells in 1982, with average migration velocities below 0.04 km/hour, which is about an order of magnitude lower than the reported creep events and historical large swarms [*Roland and McGuire*, 2009].

However, a swarm before the injection activities within this region did not exhibit migration behavior [*Gilpin and Lee*, 1978]. Similar movement was also found during a trilateration/GPS survey between 1987.95 and 1995.11, when increased injection and production were conducted. GPS stations located within the geothermal field moved significantly along a 250° azimuth, which is anomalous compared to the expected tectonic motion, suggesting it is caused by the geothermal wells located to the south and southwest [*Anderson et al.*, 2003]. Both the prior observations and geodetic measurements indicate that fluid diffusion may have a significant influence on the seismicity patterns.

Although fluid diffusion is involved in the migration of swarms, the regional stress field resulting from the SAF-IF step-over is important. From Figure 3.12, the focal mechanism solutions for this region are primarily strike-slip faulting with several normal faulting events. Assuming the principal fault plane aligns with the NE-SW trend of seismicity and the overall NNW-SSE trending plate motion, the focal mechanisms indicate the NNW-SSE strike-slip faults are coupled by NE-SW left-lateral strike-slip faults, and the normal faulting accounts for extension between a series of parallel strike-slip faults. The overall swarm migration behavior in this region shows a similar pattern with NE-SW migrating swarms bounded by NNW-SSE migrating swarms, reflecting changes in the principal stress. A study of two seismic swarms in 1975 from a microearthquake survey prior to our analysis period reveals no migration of epicenters, with normal faulting striking N65°E for the larger swarm and strike-slip faulting for the smaller swarm with either N60°W for left-lateral motion or N30°E for right-lateral motion [*Gilpin and Lee*, 1978], consistent with the distribution in Figure 3.12.

The swarm in 1981 bounds the NE-SW oriented faults and migrated at N30°W, parallel to the nearby strike-slip faults (see Fig. 7). The seismicity started with a cluster of high stress drop events at depth and migrated upward during the initial 150 hours. Then a burst of low-stress drop events occurred, followed by along-strike migration and increasing stress drop. There is little spatial migration after the largest event occurred, possibly due to the coseismic deformation from the M 5.8 mainshock. The temporal behavior of the seismicity exhibits two subclusters,

each shows power-law increasing and decreasing seismicity rate features (see Figure 3.10a). Such a migration pattern resembles seismicity triggered by a fluid intrusion process [*Hainzl and Fischer*, 2002]. After the initiation of seismicity, self-organized stress transfer and post-seismic creep among successive events possibly drive the migration of the swarm [*Hainzl*, 2003, 2004].

The large swarm in August, 2005, is located within an area with a cluster of continous injection wells, and exhibits NE-SW migration during the initial 10 hours (see Fig. 8). However, the migration behavior is not clear after several magnitude 4 events occurred 10 hours later (see Figure 3 in *Lohman and McGuire* [2007]). Modeling with diffusion curves results in a larger misfit than linear migration, and the existence of aseismic slip has been confirmed by GPS and InSAR measurements [*Lohman and McGuire*, 2007; *Crowell et al.*, 2009]. The strain rate suddenly jumped in August 2005, which coincides with the high seismicity. Increased left-lateral motion is found along the N66°E Obsidian Buttes Fault (identified in a field survey), which coincides with the location and migration direction of the 2005 swarm [*Crowell et al.*, 2009]. The increased pore fluid pressure from multiple injection wells nearby may have contributed to bringing the fault to a critical failure point, while the aseismic slip is the major factor in driving the swarm seismicity.

Region 3 is within the Brawley geothermal site and has low average stress drops, suggesting a weak region. Active exploration of geothermal energy lasted from 1983 to 1986, and the swarm occurring in 1986 exhibits apparent diffusion migration, possibly due to the increased fluids during the injection period. Three swarms in 1983, 1986 and 2008 show consistent fault planes striking NE-SW, which generally agrees with the preferred extensional stress orientation resulting from the step-over between the San Andreas and Imperial faults. The 1999 swarm occurred along a NNW striking fault plane. However, all the swarms exhibit consistent migration directions, indicating the regional stress field is controlling the migration. The migration velocities are between 0.06 and 0.4 km/hour, within the range of nearby creep events and aseismic slip driven swarms [*Lohman and McGuire*, 2007; *Roland and McGuire*, 2009].

The focal mechanisms show that the Mesquite Basin is actively subsiding and the swarm in 2000 probably marks the southern limit for this basin. This region is seismically active, and four swarms are identified during our study period. Three swarms show consistent migration directions approximately N50°E, and locate at the northern boundary of the seismicity. Their location and orientation are consistent with the northern boundary fault of the swarm in 1975 [*Johnson and Hadley*, 1976]. The 2000 swarm is further south on the Imperial Fault and migrates bilaterally along a NS direction at 0.4 km/hour. Both the velocity and migration direction are similar to the beginning of the swarm in 1975 [*Johnson and Hadley*, 1976], suggesting the four swarms are triggered by a similar process to that of the swarm in 1975. The Brawley fault is proposed to explain the overall NNW trend of the Brawley Seismic Zone, and the swarm in 1975 ruptured the Brawley fault. The NE northern boundary fault accommodates the extension between the Imperial Fault and the Brawley Fault [*Hill et al.*, 1975; *Johnson and Hadley*, 1976]. The swarms in the Mesquite Basin have migration behavior that cannot be modeled as fluid diffusion, and the velocities ranging from 0.1 to 0.4 km/hour are consistent with the observed slow slip event propagation velocity of 0.14 km/hour from creepmeters in the southern Imperial Fault zone [*Glowacka et al.*, 2001]. Thus the slow slip events are the best explanation for the observed swarm migration behavior in this region.

3.7 Discussion

Our Brune-type stress drop estimates depend upon the assumed source model and care should be taken in comparing the absolute stress drop values with those of other studies, which may have made different modeling assumptions. However, our results can be compared with other stress drops in Southern California and Parkfield, which were calculated using the same method [*Shearer et al.*, 2006; *Allmann and Shearer*, 2007]. The average stress drop of 0.56 MPa is similar to the estimates in *Shearer et al.* [2006], significantly lower than the rest of Southern California and the Parkfield section. High heat flow in the Salton Trough is a likely

cause as other studies also observe relatively low stress drops within geothermal areas, i.e., the Coso geothermal field and triggered earthquakes within the Salton Sea geothermal field [*Hough et al.*, 1999; *Hough and Kanamori*, 2002]. Analysis of spatial variations of stress drop within the Salton Trough shows the median stress drop within geothermal fields is 0.12 MPa lower than other areas. We observe increasing median stress drop with distance from injection wells up to 2.5 km away. Using the median wellhead pressure of 1 Mpa, constant pressure for 30 days (the median duration of injection events), and assuming a diffusion coefficient of 0.25 m^2/s, we calculate the pore pressure perturbation using the method of *Dinske and Shapiro* [2009]. We obtain roughly a 0.02 MPa pore pressure change 0.05 km away and about a 0.001 MPa change 0.6 km away by the end of the injection event, and the perturbation drops rapidly at greater distance. The perturbation beyond 1 km based on this simple calculation for a single injection event is too low to account for the stress drop variations. There are usually multiple injection events occurring around the same time at different locations and it is possible that the combined fluid level and pressure perturbations would have a greater impact.

Induced seismicity has been well documented and studied in the Geysers geothermal field [e.g., *Majer et al.*, 2007], where there is a general long-term temporal correlation between water injection and seismicity. Figure 3.5b and c show a correlation of increased seismicity with injection activities within local clusters. To check this relationship over a longer time span than the LSH catalog and to examine the seismicity rate before and after injection events began in 1982, we use the un-relocated SCEC catalog to obtain additional events between 1933 and 1981. We only consider events with magnitudes larger than 3 to account for the low magnitude completeness level for the older parts of the catalog. As shown in Figure 3.13b, the seismicity within the Salton Sea geothermal field remained at a low level before the injection started, and increased significantly (by approximately six times) after that. The Bombay Beach region is generally seismically quiet until the 2001 and 2009 swarms. Within the northern Imperial Fault and the Brawley Seismic Zone, the seismicity is dominated by periodic seismic bursts, with the highest seismicity rate during the aftershock sequence of the 1979 Mw 6.4 Imperial Valley

earthquake, and a relatively quiet period after that. The changes of long-term seismicity rate indicate that seismicity events within the Salton Sea geothermal field are strongly influenced by geothermal activities, while tectonic stress accumulation is the dominant effect in other regions within the Salton Trough. The difference is also suggested in the earthquake swarm migration behavior.

Using similar criteria as *Vidale and Shearer* [2006], we identified 20 distinct seismic bursts. Analysis of the temporal and spatial distribution of these bursts indicates they all have low seismic moment skew values and spatial migration behavior with a statistical significance greater than 85%. Therefore, despite differences in the timing of their largest event, we consider all of the bursts to be swarms rather than mainshock-aftershock sequences. Modeling of the seismicity front shows that the migration directions are generally consistent among local areas. Several of the swarms are better-fit with a diffusion curve than a linear migration velocity. These swarms are mostly located within the Salton Sea geothermal field, and three may have been triggered by nearby injection events. The swarm located within the Brawley geothermal field occurred around the end of the injection period when fluid levels may have been greatest. The previous observed creep rates and aseismic slip rates within this region are between 0.1 and 0.4 km/hour [*Roland and McGuire*, 2009], which are about an order of magnitude higher than the migration velocities within the Salton Sea geothermal field, but agree with the estimated migration rates for other regions. The observed migration behavior also suggests differences among the driving force for swarms within different areas, with fluid diffusion involved in the geothermal field and slow slip or creep events involved for the other swarms.

3.8   Conclusion

Analysis of the source spectra for 3332 earthquakes in the Salton Trough from 1981 to 2009 with a multiple-event EGF method reveals variations in both attenuation and stress drop. Estimated lateral variations in attenuation involve Δt^* values from -0.006 to 0.008 s, with higher attenuation within subsidence basins.

Computed Brune-type stress drops range from 0.1 to 3.7 MPa with a median value of 0.56 MPa. The stress drops are much lower than most regions in Southern California. Lower stress drops are observed within the geothermal fields and a dependence on distance from injection well locations is suggested. Detailed analysis shows that the geothermal activities strongly influence the seismicity within the Salton Sea geothermal field. 20 distinct swarms are identified from the precisely relocated catalog. The swarms may be divided into two groups, depending upon the relative timing of their largest event. A power-law decay of seismicity rate after the largest event is observed for all groups, while a power-law increase is seen building up to the largest event for the late-$M_{\max}$ group. Two subclusters are seen for the three large swarms within the late-$M_{\max}$ group. Consistent swarm migration directions are observed within each local area. Estimated swarm migration velocities range from 0.008 to 0.8 km/hour, and diffusion coefficients range from 0.2 to 0.6 m^2/s. Slow tectonic slip events are a likely driving mechanism for most of the swarms, but fluid diffusion may also drive swarms within the active geothermal fields.

Appendix

Migration modeling

We develop a weighted L1-norm method to find the best-fitting migration vector, using the parameterizations in Equations 3.5a and 3.5b. We use a grid search approach over θ, ϕ (negative for upward migration), $\vec{X}_0$, v_0, and t_0 to find the best fitting parameters:

(1) For each azimuth θ from 0 to 2π, and vertical angle ϕ from $-\frac{\pi}{2}$ to $\frac{\pi}{2}$ (for bilateral migration), we calculate the migration vector:

$$\vec{s} = \begin{cases} \cos\phi\cos\theta \\ \cos\phi\sin\theta \\ \sin\phi \end{cases} \qquad (3.6)$$

(2) Using the migration vector, we find the starting location $\vec{X_0}$ for bilateral migration by grid searching the 3-D coordinates over the swarm region. For unilateral migration, the starting location trades off with t_0, so we set $\vec{X_0}$ as the location for the first event.

(3) The distance along the migration direction is $D_i = \vec{s} \cdot (\vec{X_i} - \vec{X_0})$. We loop over possible velocities by finding an initial velocity from the interquartile range of distance and time, then set the interval as $dv = 0.1 \times \log_{10}(v_0)$ (max(dv)=0.01, units are km/hour). In this way, we have different ranges for velocities at different levels, which increases the efficiency of the search.

(4) At each possible v_0, we set $t_0 = 0$, calculate t_i^p from equations (3.5a) and (3.5b), then set $dt_i = t_i - t_i^p$. We find t_0 from $\min(dt_i)$ to $\max(dt_i)$ which can minimize $\sum w_i \times |dt_i - t_0|$, where the weight w_i is defined as:

$$
w_i = \begin{cases}
|dt_i - t_0|; & (dt_i - t_0) < 0 \\
1; & (0 \leqslant dt_i - t_0 < 0.5) \\
1/\sqrt{(dt_i - t_0)}; & (dt_i - t_0 \geqslant 0.5)
\end{cases}
\tag{3.7}
$$

This weighting approach accounts for the upper-triangular nature of the time versus distance behavior by applying the L1-norm only within a 1/2 hour window, and penalizing earlier arrivals more than late arrivals outside of this window.

(5) Update $dt_i^{new} = dt_i - t_0$, then using the same weighting procedure, find the combination of parameters that minimizes $\sum w_i^{new} \times |dt_i^{new}|$.

Applying this method to the Salton swarm sequences produces results that generally agree with the trends that can be seen from visual inspection. For a swarm on 03/15/2004, which only lasted about 2 hours, the duration is too short for the inversion method to obtain a reliable result. Instead of solving for t_0, we find that setting t_0 to the time of the first event gives the best result for this swarm.

For diffusion curve modeling, the migration follows: $r = \sqrt{4\pi D t}$, where D is the diffusion coefficient and r is the distance for each event from the location of fluid intrusion. For convenience, we model $r^2 = 4\pi D(t - t_0)$ using the linear method, in which $r^2 = |X - X_0|^2$. We apply a similar grid search method and

weighing procedure to find the best-fitting diffusion coefficient and misfit for the true dataset.

Statistical tests

We perform two statistical tests for the significance of our swarm migration parameters. We first check whether we obtain a significantly better fit to the data than what might be expected by random chance. For this test, we randomly scramble (shuffle) the occurrence times for the events in the swarm, but keep their true locations. In this way, all actual time migration behavior is removed. Then we run the inversion process for the new set of data, and calculate the best-fitting parameters and resulting misfit. This process is repeated 100 times, and we estimate the probability that migration is resolved as the fraction of times the true dataset produces a lower misfit than the time-scrambled data sets. With this method, we find that most swarms migrate with probability greater than 95%, with a few having lower probabilities between 85% and 90%.

The second test is to estimate confidence limits for the migration parameters using a bootstrap resampling method. We treat the time and location for each event as a 4-D dataset $X(x_i, y_i, z_i, t_i, i = 1....N)$, and randomly resample the dataset by generating the random integer sequence $I(i_i, i = 1.....N)$ and a new dataset $X_n = X(x_k, y_k, z_k, t_k, k = i_i, i = 1....N)$. A new set of best-fitting parameters is solved for each new dataset, and the range is found from 100 separate resampling results. Tests of this approach applied to the synthetic dataset show that the estimated dip angle will generally have a larger uncertainty than the azimuth. The parameters θ and ϕ tend to trade off with each other since they are included in the inversion of the unit migration vector, so they usually have a larger range. A better approach is to estimate the total angular uncertainty in the migration directions, which generally produces uncertainty estimates for the real data set of 10° to 20°.

For the diffusion modeling, we apply the same bootstrap procedure to find the migration significance and estimated uncertainties in the diffusion coefficient.

To determine whether we obtain a better with a diffusion curve, we apply the second bootstrap test for the same dataset with both linear migration and the diffusion curve with 100 times resampling. Then we use the cumulative density function to compare the misfit distributions from the two migrations, and check if the diffusion curve has a lower misfit than the linear migration. The five datasets with lower misfits using the diffusion curve are listed in Table 3.3.

Acknowledgements

Chapter 3, in full, is a reformatted version of a publication in Journal of Geophysical Research: Chen, X., and P. M. Shearer, Comprehensive analysis of earthquake source spectra and swarms in the Salton Trough, California, *J. Geophys. Res.*, 116, doi:10.1029/ 2011JB008263, 2011. I was the primary investigator and author of the paper, which describes how we analyzed source spectra of events in the Salton Trough and investigated their relationship with geothermal activities. We also studied 20 individual swarms in this region, and their migration behavior.

References

Allmann, B. P., and P. M. Shearer (2007), Spatial and temporal stress drop variations in small earthquakes near parkfield, california, *Journal of Geophysical Research-Solid Earth*, *112*(B4), 17.

Audigane, P., J. J. Royer, and H. Kaieda (2002), Permeability characterization of the soultz and ogachi large-scale reservoir using induced microseismicity, *Geophysics*, *67*(1), 204–211.

Anderson, G., D. C. Agnew and H. O. Johnson (2003), Salton trough regional

deformation estimated from combined trilateration and survery-mode GPS data, *Bull. Seismol. Soc. Am., 93*(6), 2402-2414.

Båth, M. (1965), Lateral inhomogeneities of the upper mantle, *Tectonophysics, 2*(6), 483-514.

Brothers, D. S., N. W. Driscoll, G. M. Kent, A. J. Harding, J. M. Babcock and R. L. Baskin (2009), Tectonic evolution of the Salton Sea inferred from seismic reflection data, *Nature Geosci, 2*(8), 581-584.

Brune, J. N. (1969), Tectonic stress and the spectra of seismic shear waves from earthquakes, *J. Geophys. Res., 75.*

Burford, R. O. (1977), Bimodal distribution of creep event amplitudes on the San Andreas fault, California, *Nature, 268,* 424-426.

Crowell, B. W., Y. Bock, and D. T. Sandwell (2009), Interseismic Strain Accumulation in the Imperial Valley and Implications for Triggering of Large Earthquakes in Southern California, *Eos Trans. AGU, 90*(54), Fall Meet. Suppl., Abstract T33E-02.

Dinske, C., and S. Shapiro (2010), Interpretation of microseismicity induced by time-dependent injection pressure, *SEG Expanded Abstr., 29*, 21252129.

Enescu, B., S. Hainzl and Y. Ben-Zion (2009), Correlations of seismicity patterns in southern California with surface heat flow data, *Bull. Seismol. Soc. Am., 99*(6), 3114-3123.

Farrell, J., S. Husen, and R. B. Smith (2009), Earthquake swarm and b-value characterization of the yellowstone volcano-tectonic system, *Journal of Volcanology and Geothermal Research, 188*(1-3), 260–276.

Fischer, T. (2003), The Augues-December 2000 earthquake swarm in NW Bohemia: the first results based on automatic processing of seismograms, *Journal of Geodynamics, 35*(1-2), 59-81.

Gilpin B., and T. C. Lee (1978), Micro-earthquake study in Salton Sea geothermal area, California, *Bull. Seismol. Soc. Am., 68*(2), 441-450.

Glowacka, E., J. J. Gonzalez, F. A. Nava, F. Farfan, and G. Diaz de Cossio (2001), Monitoring surface deformation in the Mexicali Valley, BC, Mexico, *the 10th FIG International Symposium on Deformation Measurements,* CA. Inst. of Technol., Organe, CA.

Goertz-Allmann, B. P., A. Goertz, and S. Wiemer (2010), Stress drop variations of induces earthquakes at the basel geothermal site, *Geophysical Research Letters*, 38 (L09308), doi:10.1029/2011GL047498.

Goldsmith, M (1976), Geothermal development and the Salton Sea, *Energy, 1*, 367-373.

Gunasekera, R. C., G. R. Foulger and B. R. Julian (2003), Reservoir depletion at the Geysers geothermal area, California, shown by four-dimensional seismic tomography, *J. Geophys. Res., 108*(B3), 2134, doi:10.1029/2001JB000638.

Hainzl, S. and T. Fischer (2002), Indications for a successively triggered rupture growth underlying the 2000 earthquake swarm in Vogtland/NW Bohemia, *J. Geophys. Res., 107*(B12), 2338, doi:10.1029/2002JB001865.

Hainzl, S. (2003), Self-organization of earthquake swarms, *Journal of Geodynamics, 35*(1-2), 157-172.

Hainzl, S. (2004), Seismicity patterns of earthquake swarms due to fluid intrusion and stress triggering, *Geophysical Journal International, 159*(3), 1090-1096.

Hainzl, S., and Y. Ogata (2005), Detecting fluid signals in seismicity data through statistical earthquake modeling, *J. Geophys. Res., 110*, B05S07, doi:10.1029/2004JB003247.

Hardebeck, J. L. and P. M. Shearer, Using S/P Amplitude Ratios to Constrain the Focal Mechanisms of Small Earthquakes, *Bull. Seismo. Soc. Am.*, 93, 2434-2 444, 2003.

Hauksson, E., and P. M. Shearer (2006), Attenuation models (Q_p and Q_s) in three dimensions of the southern California crust: Inferred fluid saturation at seismogenic depths, *J. Geophys. Res., 93*, B05302, doi:10.1029/2005JB003947.

Hayashi, Y. and Y. Morita (2003), An image of a magma intrusion process inferred from precise hypocentral migrations of the earthquake east of the Izu peninsula, *Geophysical Journal International, 153*(1), 159-174.

Hill, D. P., P. Mowinckel and L. G. Peake (1975), Earthquake, active faults, and geothermal areas in the Imperial Valley, California, *Science, 188*, 1306-1308.

Hough, S. E., J. M. Lees and F. Monastero (1999), Attenuation and source properties at the Coso geothermal area, California, *Bull. Seismol. Soc. Am., 89(6)*, 1606-1619.

Hough, S. E. and H. Kanamori (2002), Source properties of earthquakes near the Salton Sea triggered by the 16 October 1999 M 7.1 Hector Mine, California, Earthquake, *Bull. Seismol. Soc. Am., 92*(4), 1281-1289.

Johnson, C. E. and D. M. Hadley (1976), Tectonic implications of Brawley earthquake swarm, Imperial-Valley, California, January 1975, *Bull. Seismol. Soc. Am., 66*(4), 1133-1144.

Kanamori, H. (1977), The energy release in great earthquakes, *J. Geophys. Res.*, *82*, 2981-2987.

King, C. Y., R. D. Nason and D. Tocher (1973), Kinematics of fault creep, *Phil. Trans. Roy. Soe. Lond., Ser. A.,* 274, 344-360.

Lin, G., P. M. Shearer, E. Hauksson, and C. H. Thurber (2007a), A three-dimensional crustal seismic velocity model for southern California from a composite event method, *J. Geophys. Res., 112*, B11306, doi:10.1029/2007JB004977

Lin, G., P. Shearer and E. Hauksson (2007b), Applying a three-dimensional velocity model, waveform cross correlation, and cluster analysis to locate southern California seismicity from 1981 to 2005, *J. Geophys. Res., 112*, B12309, doi:10.1029/2007JB004986

Linde, A. T., M. T. Gladwin, M. J. S. Johnston, R. L. Gwyther and R. G. Bilham (1996), A slow earthquake sequence on the San Andreas fault, *Nature, 383,* 65-68.

Lohman, R. B. and J. J. McGuire (2007), Earthquake swarms driven by aseismic creep in the Salton Trough, California, *J. Geophys. Res., 112*, B04405, doi:10.1029/2006JB004596.

Madariaga, R. (1976), Dynamics of an expanding circular fault, *Bull. Seismol. Soc. Am., 66,* 639-666.

Majer, E. L., R. Baria, M. Stark, S. Oates, J. Bommer, B. Smith, and H. Asanuma (2007), Induced seismicity associated with enhanced geothermal systems, *Geothermics, 36(3)*, 185-222.

Ogata, Y. (1988). Statistical models for earthquake occurrences and residual analysis for point-processes, *J. Am. Statist. Assoc. 83,* 9-27.

Omori, F. (1895), On the aftershocks of earthquakes, *J. Coll. Sci. Imp. Univ. Tokyo, 7*, 111-200.

Roland, E. and J. J. McGuire (2009), Earthquake swarms on transform faults, *Geophysical Journal International, 178(3),* 1677-1690.

Ross, A., G. R. Foulger and B. R. Julian (1999), Source processes of industrially-induced earthquakes at the Geysers geothermal area, California, *Geophysics, 64(6)*, 1877-1889.

Schlotterbeck, B. A. and G. A. Abers (2001), Three-dimensional attenuation variations in southern California, *J. Geophys. Res., 106,* B2, 30719-30735.

Schmitt, A. K. and J. B. Hulen (2008), Buried rhyolites within the active, high-temperature Salton Sea geothermal system, *Journal of Volcanology and Geothermal Research, 178*(4), 708-718.

Shapiro, S. A., S. Rentsch and E. Rothert (2005), Characterization of hydraulic properties of rocks using probability of fluid-induced microearthquakes, *Geophysics, 70(2),* F27-F33.

Shearer, P. M, G. A. Prieto and E. Hauksson (2006), Comprehensive analysis of earthquake source spectra in southern California, *J. Geophys. Res., 111*, B06303, doi:10.1029/2005JB003979.

Svensen, H., Ø. Hammer, A. Mazzini, N. Onderdonk, S. Polteau, S. Planke, and Y. Y. Podladchikov (2009), Dynamics of hydrothermal seeps from the Salton Sea geothermal system (California, USA) constrained by temperature monitoring and time series analysis, *J. Geophys. Res., 114*, B09201, doi:10.1029/2008JB006247.

Vidale, J. E., and P. M. Shearer (2006), A survey of 71 earthquake bursts across southern California: Exploring the role of pore fluid pressure fluctuations and aseismic slip as drivers, *J. Geophys. Res. 111*, B05312, doi:10.1029/2005JB004034.

Table 3.1: Information for each swarm. The spatial distribution is determined using an eigenvalue analysis (see text). The larger swarms (1981, 2005, 2009) divide naturally into subswarms, for which we show separate strikes and dips. We set the duration as the median of the time delay from the first event in the sequence.

index	starting time	location		spatial distribution			duration	t_{max}	skew
		lat	lon	strike	dip	shape	(days)		
1	04/20/1981, 18:49	33.095	-115.629	45.6	89.9	line	5.5	1.10	-9.36
	04/25/1981, 04:01	33.097	-115.626	169.6	86.3	plane			
2	05/07/1983, 11:49	33.151	-115.623	52.2	87.1	plane	3.5	0.79	1.48
3	07/11/1983, 22:05	33.194	-115.527	165.4	87.5	sphere	2.2	0.86	-1.36
4	11/14/1983, 16:23	33.035	-115.559	41.4	87.2	line	0.6	0.79	0.97
5	08/20/1985, 16:23	33.306	-115.682	-26.3	86.4	line	0.07	0.65	0.67
6	02/17/1986, 09:35	32.946	-115.543	232.3	86.6	line	0.23	0.17	2.0
7	08/02/1986, 23:55	33.032	-115.579	27.3	85.6	line	1.0	2.23	0.22
8	06/28/1987, 10:56	33.164	-115.657	49.7	81.8	line	4.84	1.37	-0.38
9	10/18/1999, 20:32	33.047	-115.569	-11.7	78.9	sphere	0.49	0.08	-0.29
10	05/10/2000, 23:25	33.157	-115.636	179.7	81.2	plane	1.57	0.00	3.49
11	06/14/2000, 19:05	32.892	-115.506	184.2	70.8	plane	0.17	0.00	2.04
12	11/13/2001, 13:43	33.317	-115.703	43.4	87.3	plane	0.33	0.83	1.00
13	03/01/2003, 03:05	32.917	-115.528	227.9	82.5	line	0.23	0.71	-0.16
14	04/08/2003, 20:58	33.171	-115.603	42.9	76.7	line	5.12	0.78	1.12
15	05/23/2003, 15:39	32.937	-115.551	46.7	70.2	sphere	0.48	1.17	0.29
16	03/15/2004, 23:56	33.196	-115.577	-19.6	85.9	plane	0.04	0.30	2.83
17	08/31/2005, 09:32	33.176	-115.601	47.3	88.8	line	14.5	1.02	-0.34
	09/01/2005, 10:24	33.147	-115.641	45.8	89.1	line			
18	09/15/2005, 0:57	33.242	-115.529	166.4	75.3	sphere	4.89	1.30	-0.59
19	06/02/2008, 02:30	33.028	-115.556	228.4	83.3	line	0.33	0.17	1.80
20	03/21/2009, 12:41	33.314	-115.725	57.0	83.3	plane	4.37	0.69	0.93
	03/25/2009, 05:22	33.289	-115.716	48.9	85.5	line			

Table 3.2: Migration parameter estimates. "U" and "B" indicate the migration style: unilateral or bilateral. Each index corresponds to the same swarm in Table 3.1.

index	migration	azimuth (deg)		dip (deg)		velocity (km/hour)	
		original	range	original	range	original	range
1	100%, U	341.1	-71.6, 6.35	-65.9	-76.4, -55.8	0.024	0.021, 0.025
	100%, U	155.5	132.0, 167.5	15.4	14.3, 23.4	0.071	0.065, 0.076
2	100%, U	246.0	208.2, 247.2	-62.5	-63.6, 2.82	0.015	0.013, 0.022
3	100%, U	10.9	8.6, 20.1	64.7	53.2, 71.6	0.039	0.023, 0.038
4	99%, U	204.8	199.0, 246.0	-1.8	-20.1, 13.1	0.058	0.046, 0.061
5	100%, U	330.8	-25.7, 10.9	-20.1	-33.8, -8.64	0.263	0.223, 0.333
6	86%, B	243.7	220.8, 243.6	47.5	45.2, 52.1	0.110	0.070, 0.128
7	94%, B	30.4	7.5, 41.9	75.0	59.4, 76.4	0.030	0.020, 0.044
8	100%, U	75.1	62.5, 79.7	-33.8	-48.7, -17.8	0.0079	0.007, 0.008
9	86%, U	195.6	156.6, 208.2	61.3	45.2, 83.0	0.090	0.060, 0.175
10	100%, U	1.76	-11.99, 15.52	13.1	9.12, 17.1	0.041	0.037, 0.045
11	100%, B	1.86	-2.35, 6.06	-7.5	-15.5, 9.7	0.338	0.307, 0.432
12	100%, U	204.8	193.3, 208.2	-0.62	-9.7, 10.7	0.367	0.274, 0.373
13	98%, B	59.1	45.4, 60.3	-55.6	-63.3, -52.7	0.091	0.078, 0.108
14	85%, U	41.9	25.8, 61.3	6.26	-6.35, 38.3	0.033	0.015, 0.036
15	98%, U	80.8	67.1, 80.8	23.4	-1.8, 33.8	0.150	0.114, 0.168
16	96%, U	138.3	130.3, 142.9	77.3	26.8, 84.2	0.856	0.645, 0.959
17	99%, U	200.2	196.7, 226.5	-22.4	-29.2, -6.35	0.134	0.117, 0.165
	98%, U	210.5	208.2, 213.9	-32.7	-49.9, -36.1	0.089	0.077, 0.122
18	95%, U	133.7	129.1, 142.9	63.6	45.2, 76.8	0.080	0.079, 0.092
19	86%, U	234.6	199.1, 252.9	34.9	1.7, 47.5	0.316	0.193, 0.619
20	100%, B	62.5	54.6, 63.6	53.2	42.9, 53.3	0.015	0.015, 0.018
	100%, B	41.9	42.0, 53.3	-40.7	-78.4., -34.9	0.036	0.035, 0.039

Table 3.3: Hydraulic diffusion coefficient (range represents m^2/s) for four swarms, swarm index corresponds to index numbers in Table 3.1.

| index	date	significance	coefficient	range
1	04/20/1981	100%	0.597	0.558, 0.631
2	05/07/1983	100%	0.446	0.419, 0.473
7	08/02/1986	94%	0.193	0.173, 0.213
8	06/28/1987	100%	0.279	0.211, 0.347
14	04/08/2003	100%	0.299	0.251, 0.347
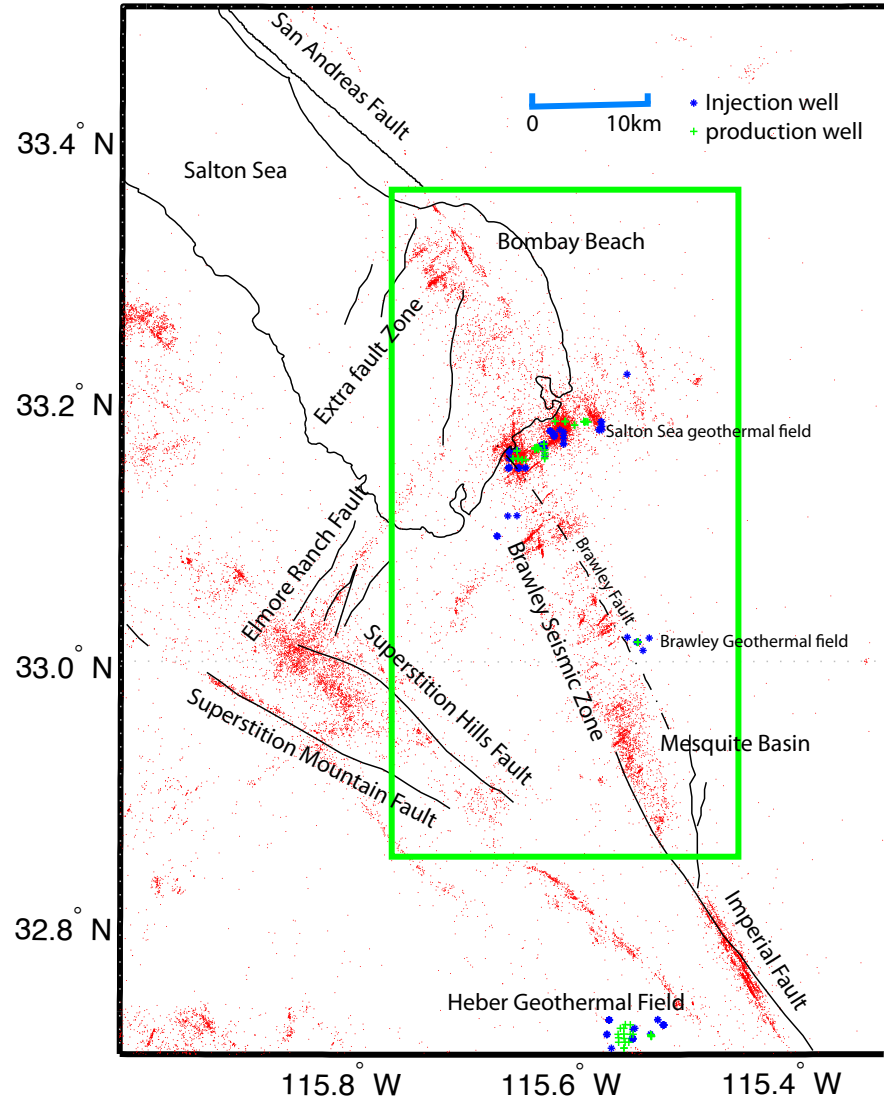
Figure 3.1: Map view of seismicity from 1981 to 2009 in the Salton Trough. The green box is the study region in this paper. Dashed lines are the estimated Brawley fault location from *Hill et al.* [1975].
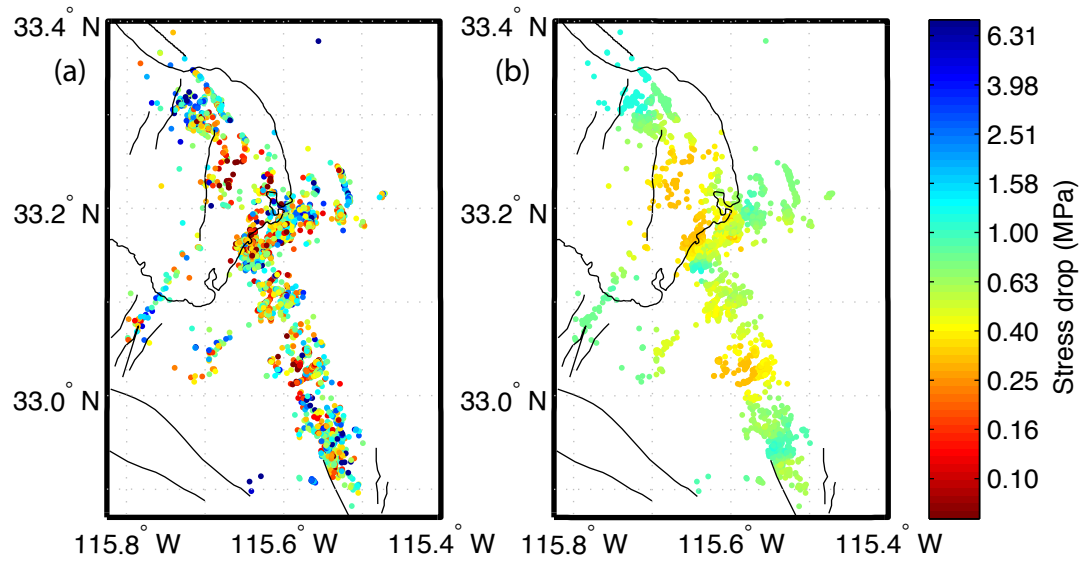
Figure 3.2: Figure (a) is a map view of stress drop estimates for 3332 events obtained using the multiple EGF method. Figure (b) is a map view of smoothed stress drop estimates by applying a spatial median filter.
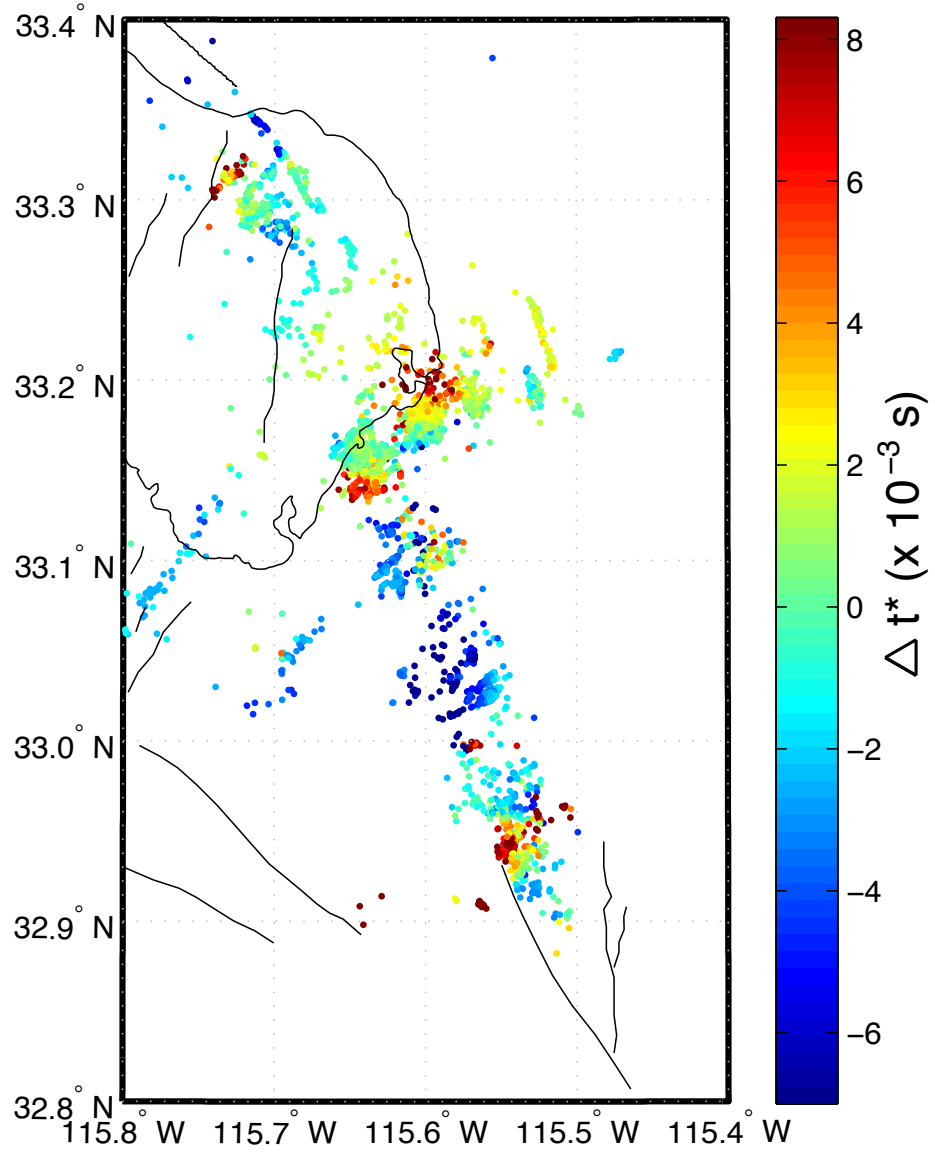
Figure 3.3: Map view of Δt^* variations calculated by a least-squares fit to the spectral ratio between the spatially varying EGF and the constant EGF. Colors show Δt^* in seconds, with red indicating more attenuation while blue is less attenuation.
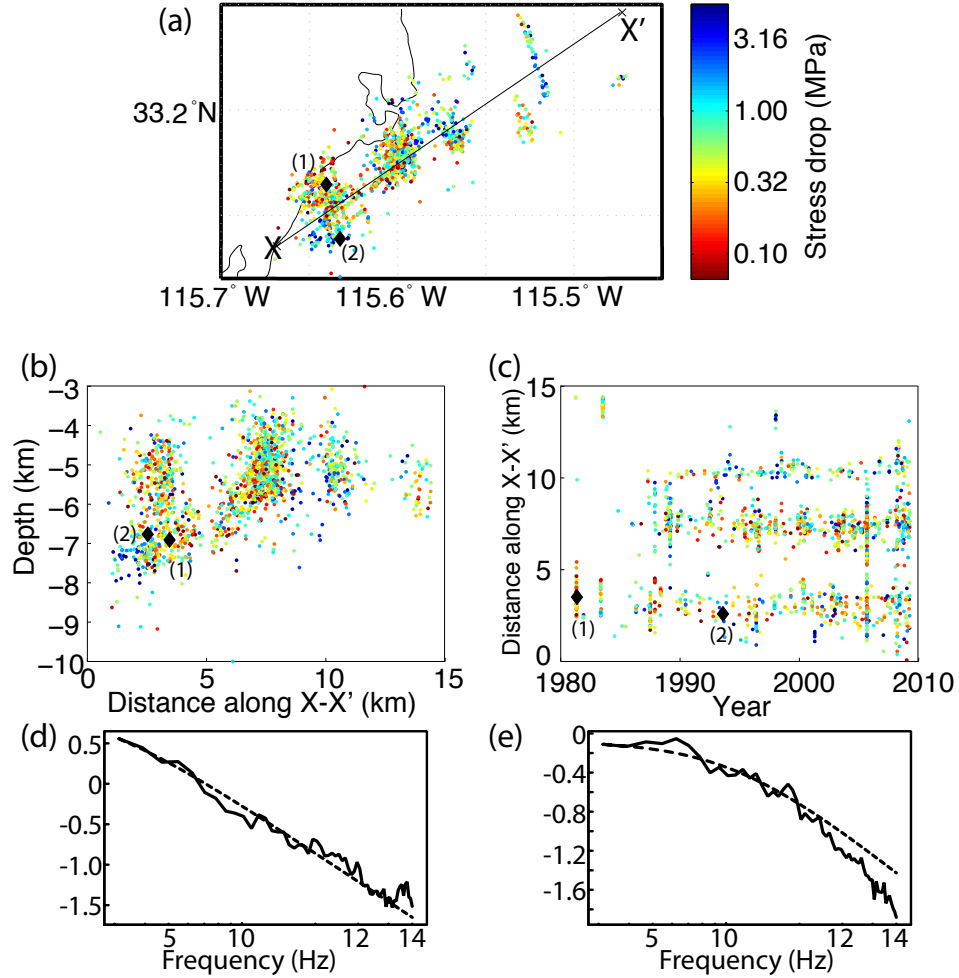
Figure 3.4: (a) Map view of stress drops near the Salton Sea geothermal site (same region as Figure 3.5). (b) Cross-section along profile X-X'. (c) Event distance along profile X-X' versus occurrence time and colored by stress drop. (d) Spectrum of a low stress drop event (event 1) with stress drop of 0.12 MPa, corner frequency of 2.8 Hz and magnitude of 2.4. (e) Spectrum for a high stress drop event (event 2) with stress drop of 4.9 MPa, corner frequency of 16 Hz and magnitude of 2.1. The black solid lines in (d) and (e) are EGF-corrected source spectra and the black dashed lines are theoretical spectra. The diamonds in Figure (a), (b) and (c) show the locations and times for the two events.
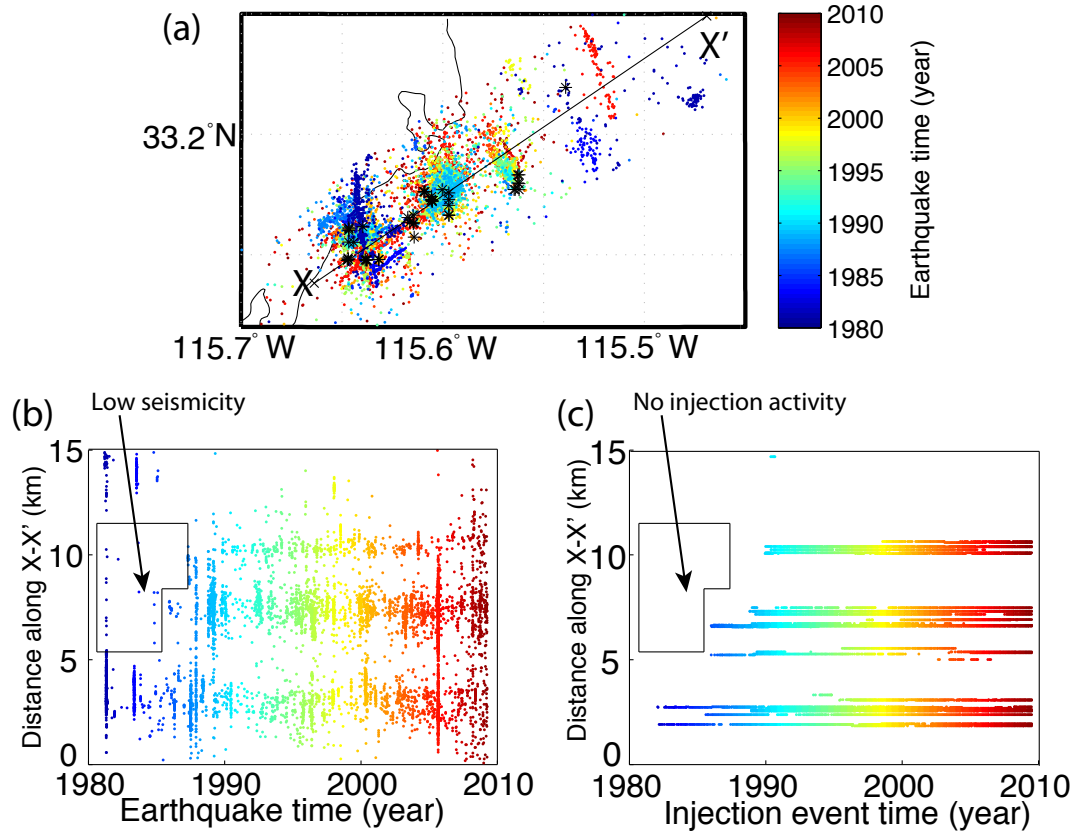
Figure 3.5: (a) Map view of seismicity near the Salton Sea geothermal site (same region as Figure 3.4). Events are colored by occurrence time, black stars are locations of injection wells. (b) Event distance along profile X-X' versus occurrence time. (c) Injection event distance along profile X-X' versus injection time.
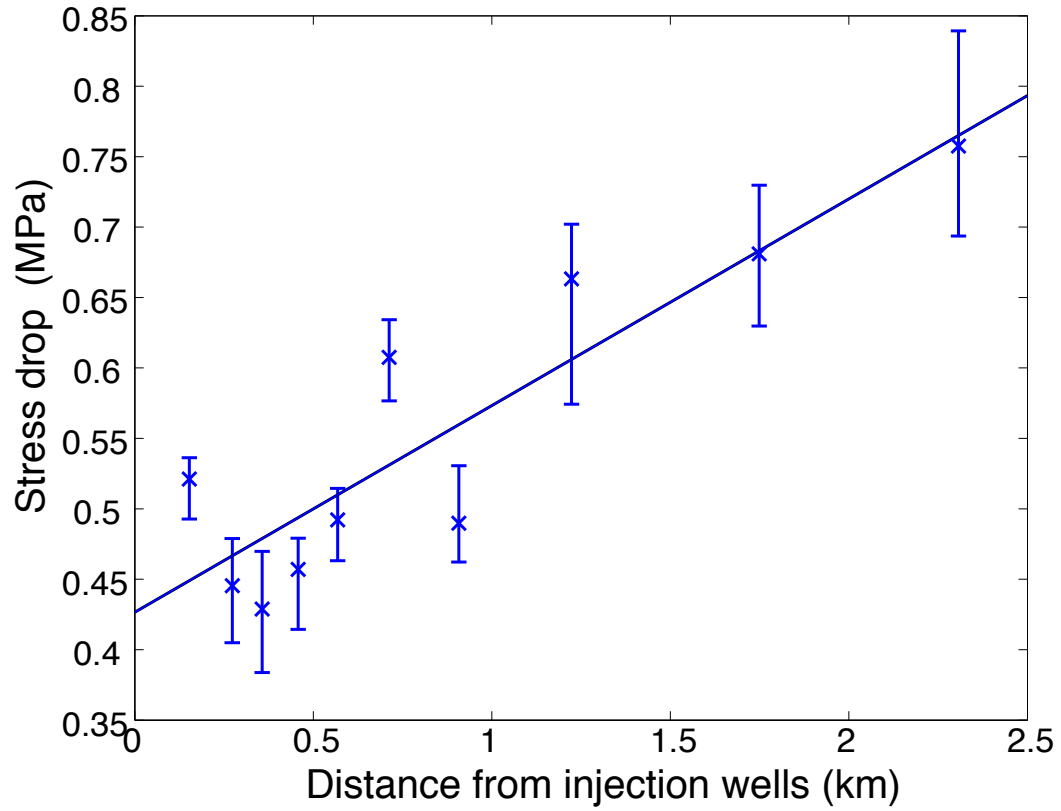
Figure 3.6: Stress drop versus event distance from the nearest injection wells. The Y-axis is the median stress drop for each bin with an equal number of events, sorted by their distance to the injection wells. Error bars are estimated from a bootstrap approach by resampling events within each bin 1000 times, and finding the median value for each resampled dataset. The X-axis is the median distance from injection wells for events within each bin.
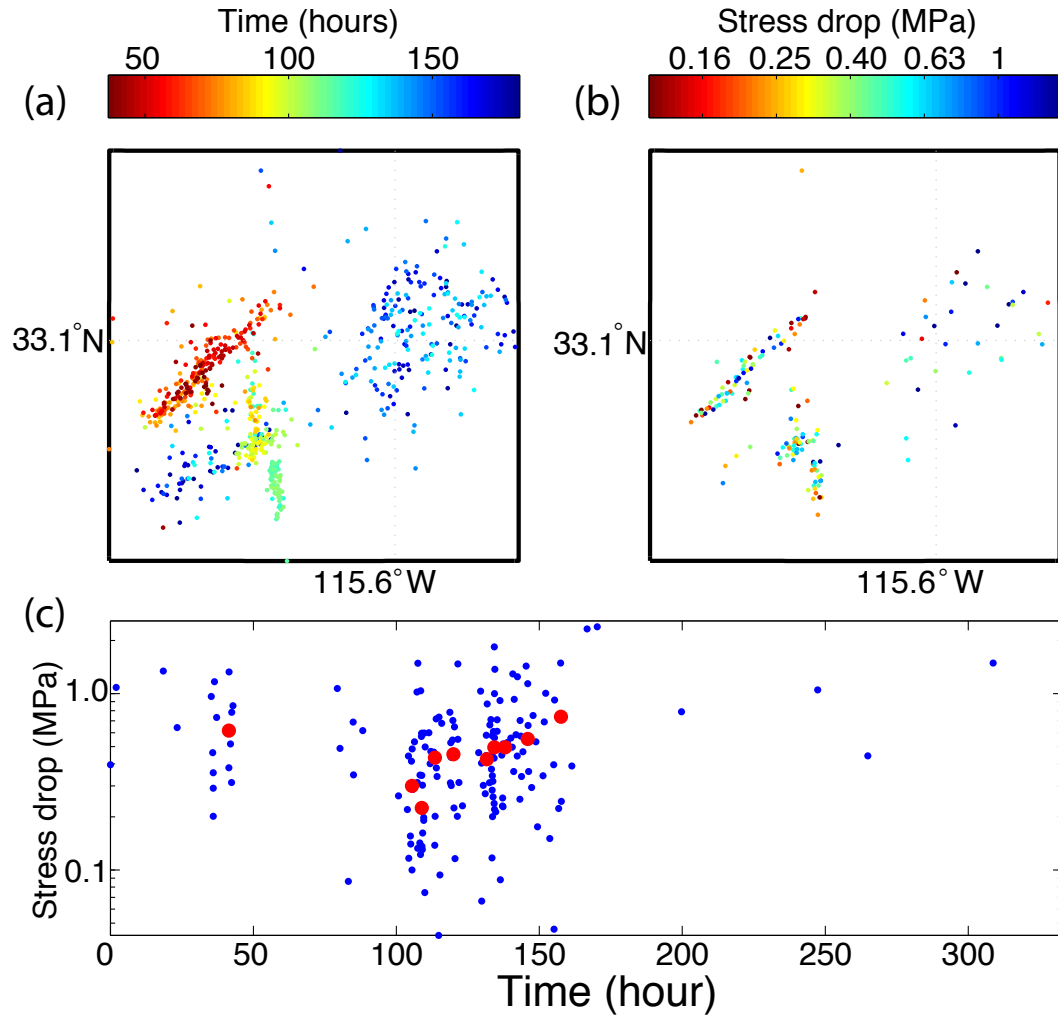
Figure 3.7: (a) Map view of the 1981 swarm with events colored by their occurrence times. (b) Map view of the 1981 swarm with events colored by their stress drop values. (c) Stress drop versus time for the 1981 swarm. The red dots are median values for 10 bins with an equal number of events.
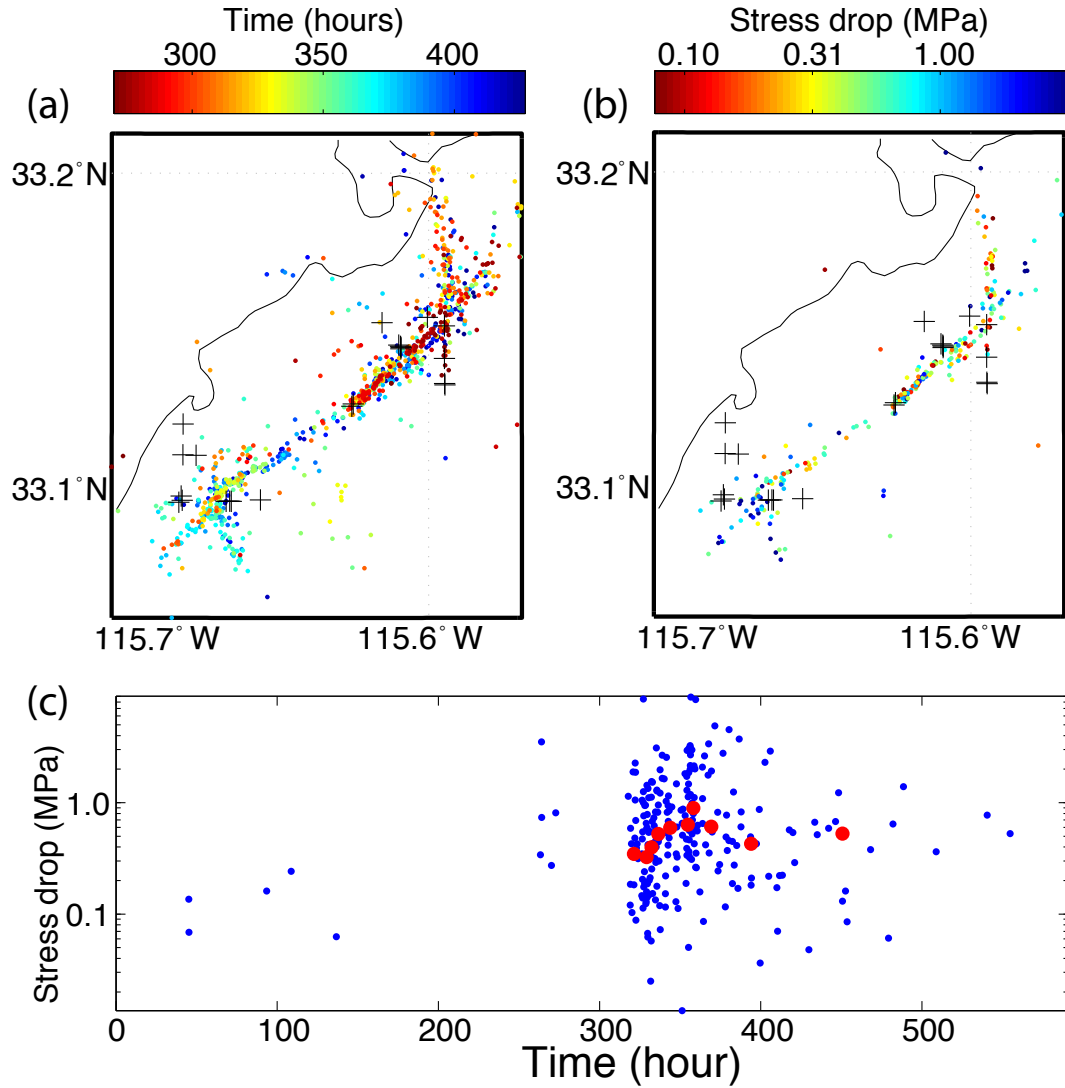
Figure 3.8: (a) Map view of the August, 2005 swarm with events colored by their occurrence times. (b) Map view of the 2005 swarm with events colored by their stress drop values. (c) Stress drop versus time for the 2005 swarm. The red dots are median values for 10 bins with an equal number of events. Black "+" in (a) and (b) are injection wells that are active during the swarm period.
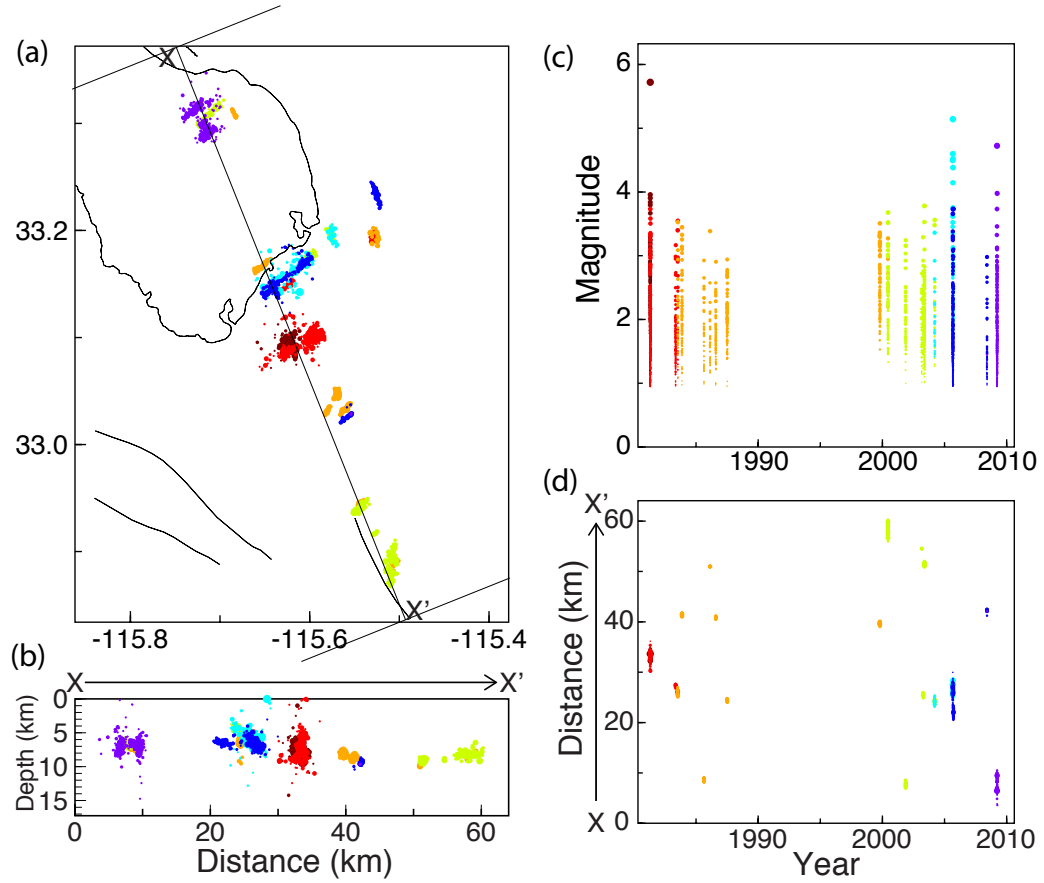
Figure 3.9: Seismic swarms in the Salton Trough. Events are colored by occurrence time with dark red indicating the earliest event and purple indicating the latest event. The size of the closed circles is assigned according to earthquake magnitude. (a) Map view of earthquake swarms, (b) cross-section view along profile X-X' from (a), (c) magnitude versus time, (d) distance of earthquakes along X-X' versus time.
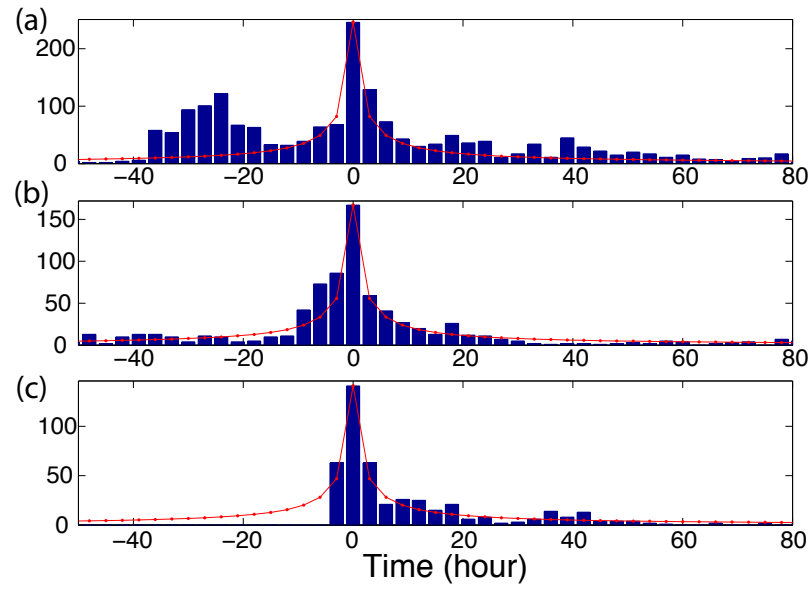
Figure 3.10: (a) Histograms of the stacked time histories for three swarms with more than 400 events within the late-$M_{\max}$ group, (b) eleven swarms with fewer than 200 events within the late-$M_{\max}$ group, and (c) early-$M_{\max}$ group. Event time is relative to the largest event in each sequence. The red lines show the power-law (t^{-1}) increase before the largest event and the decay after the largest event, i.e., Omori's Law.
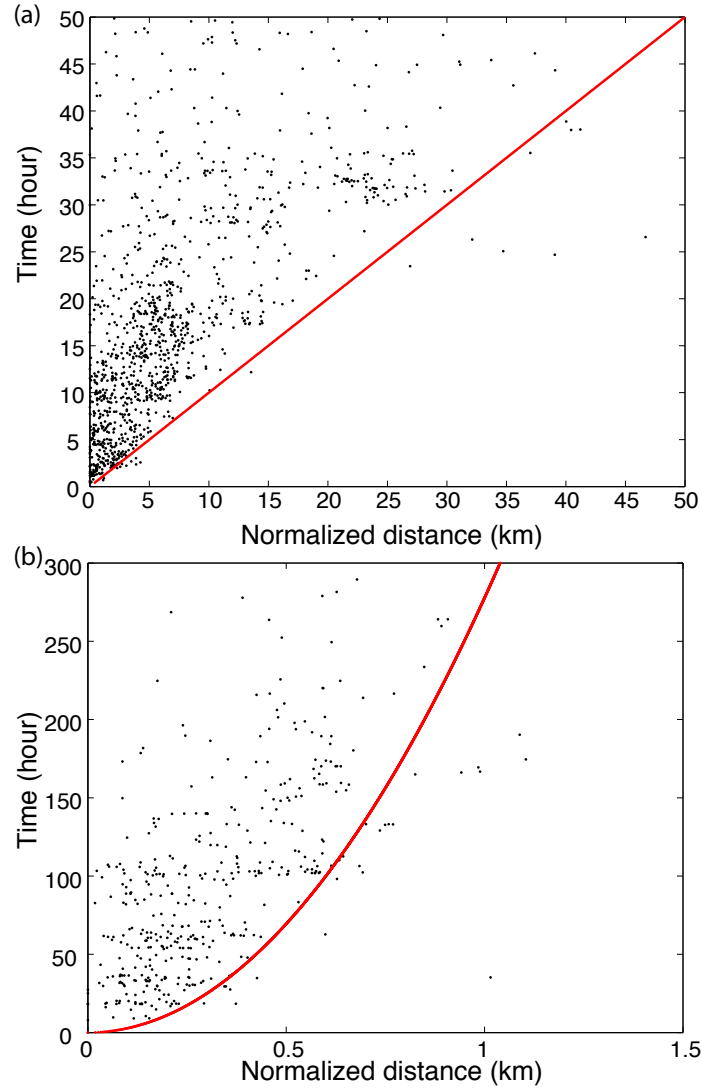
Figure 3.11: Stacked migration behavior of swarm seismicity. (a) is a stacked linear migration curve for all swarms in Table 3.2, x-axis is normalized distance by migration velocity. (b) is a stacked diffusion curve for swarms in Table 3.3, x-axis is normalized distance by $\sqrt{4\pi D}$ (D is the diffusion coefficient).
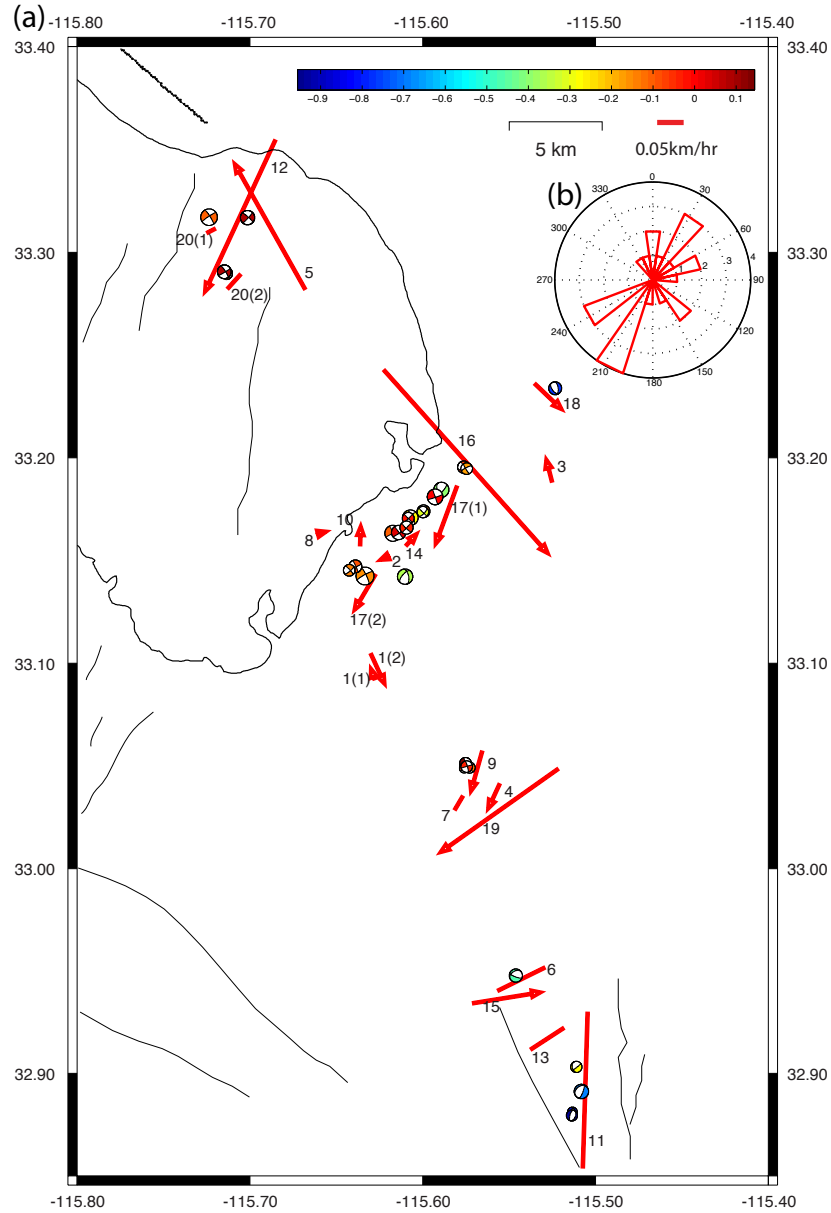
Figure 3.12: (a) Map view of swarm locations. The index numbers correspond to Table 3.1. Red lines with arrows show unilateral migration while red lines without arrows show bilateral migration. The length of each line is proportional to the migration velocity. The red line on the top right indicates a velocity of 0.05 km/hr. The beach balls are colored according to the type of focal mechanisms: -1 indicates normal faulting and 0 is strike-slip faulting. (b) Rose histogram of migration directions from Table 3.2.
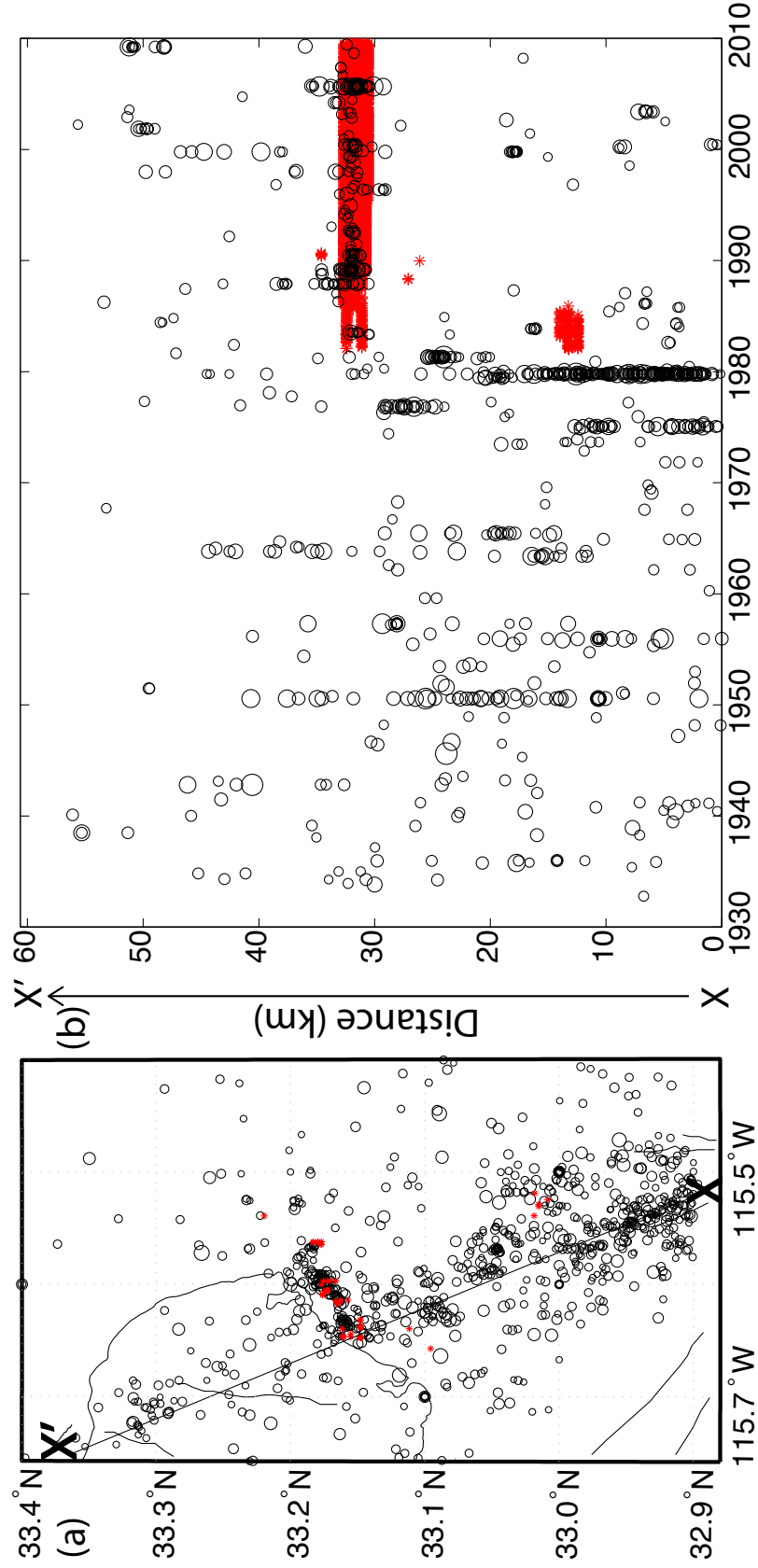
Figure 3.13: (a) Map view of earthquakes with $M \geq 3$ since 1933. The size of the black circles scale according to the size of the event. Red stars are the injection well locations. (b) Distance along profile X-X' versus time for earthquakes (black circles) and injection event (red stars).

Chapter 4

Spatial migration of earthquakes within seismic clusters in Southern California: Evidence for fluid diffusion

Seismicity within many earthquake swarms is observed to migrate slowly with time, which may reflect event triggering due to slow fault slip or fluid flow. We search for this behavior in Southern California by applying a weighted least-squares method to quantify event migration within 69 previously observed seismicity bursts. We obtain best-fitting migration directions and velocities, and compute a statistical migration significance s_m for each burst using a bootstrap resampling method. We define 37 bursts with $s_m \geq 0.8$ as the migration group, and 32 bursts with $s_m < 0.8$ as the non-migration group. To explore differences between the two groups, for each burst we compute effective stress drop ($\Delta\sigma_{quasi}$, the ratio between total moment and radius), the skew of the moment release time series (μ), the timing of the largest event (t_{max}), and the distance separation between the first half and second half of the sequence (d_s). As expected, the migration group features larger d_s and lower $\Delta\sigma_{quasi}$, consistent with higher migration significance. It also features lower μ and higher t_{max}, similar to observations from swarms in the Salton

Trough [*Chen and Shearer*, 2011], while the non-migration group is more similar to mainshock-aftershock sequences. To explore possible fluid involvement, we model the migration behavior with the fluid diffusion equation, and identify 18 bursts with diffusion coefficients ranging from 0.01 to 0.8 m^2/s, with the majority below 0.16 m^2/s. The obtained diffusion coefficients and migration behavior are similar to the Reservoir-induced seismicity beneath the Açu reservoir in Brazil [*El Hariri et al.*, 2010]. The majority of normal faulting events are associated with these 18 bursts, while the non-migration group has the most reverse faulting events, indicating a possible link between sequence type and focal mechanism.

4.1   Introduction

Earthquakes are observed to strongly cluster in time and space. Two major sources for earthquake clustering are mainshock-aftershock sequences and swarms. Aftershock sequences are triggered directly or indirectly by a large earthquake near the beginning of the sequence, while earthquake swarms do not have obvious mainshocks, and are thought to be mainly triggered by an underlying physical processes, such as fluid flow or aseismic slip. Fluid involvement is commonly observed for volcanic swarms, for which the spatial-temporal evolution of seismicity and earthquake source properties (focal mechanism, spectral characteristics, etc.) are consistent with magma movement [e.g., *Hough et al.*, 2000; *Hayashi and Morita*, 2003; *Yukutake et al.*, 2011]. Fluids are also common drivers for non-volcanic swarms within geothermal regions or induced by impoundment of reservoirs [e.g., *Kato et al.*, 2010; *El Hariri et al.*, 2010; *Daniel et al.*, 2011]. The occurrence of induced seismic swarms during injection experiments is a strong indicator of fluid triggering, e.g., at the Coso geothermal field [*Julian et al.*, 2009]. Aseismic slip as a driving force has been observed for a swarm within the Salton Trough [e.g., *Lohman and McGuire*, 2007]. Most earthquake swarms exhibit spatial migration of a seismicity front [e.g., *Roland and McGuire*, 2009; *Chen and Shearer*, 2011], and this migration behavior can help to distinguish between different triggering mechanisms. The fluid-involved swarms can be modeled as a diffusion process,

with diffusivity ranging from 0.02 to about 10 m^2/s [e.g., *do Nascimento et al.*, 2005; *Shapiro et al.*, 2005; *Parotidis et al.*, 2005; *Talwani et al.*, 2007] .

Vidale and Shearer [2006] (VS2006) investigated 71 seismic bursts across Southern California based on a waveform-relocated catalog. They classified the bursts into 'swarm-like', 'aftershock-like' and 'mixed' categories according to the timing of the largest event in each sequence. They argued that the strong spatial expansion of 'swarm-like' bursts can be explained by fluid diffusion processes, but that the steady rate of seismicity during many swarms was more consistent with aseismic slip episodes. *Chen and Shearer* [2011] (CS2011) developed a weighted least-squares method to model the migration of seismicity onsets, and used the best-fitting migration velocities and directions to distinguish between swarms driven by fluid flow and aseismic slip. Pore fluid diffusion is typically at velocities on the order of m/day, generally much slower than aseismic slip-driven migration, which is usually at km/hour [*Roland and McGuire*, 2009]. In this study, we take advantage of the LSH catalog [*Lin et al.*, 2007] which features high resolution within similar event clusters, to update the locations of the 71 bursts identified in VS2006, and apply the migration analysis procedure from CS2011 to these bursts. The waveform-relocated catalog for the reservoir-induced seismicity (RIS) beneath the Açu reservoir in Brazil (henceforth referred to as the Brazil swarm), previously analyzed in detail [*do Nascimento et al.*, 2004; *do Nascimento et al.*, 2005; *El Hariri et al.*, 2010], is also included in our analysis for comparison. Our results help clarify the differences among earthquake bursts and their origins, and provide evidence for fluid migration as the driving force behind many swarms in southern California.

4.2   Migration behavior

With updated locations, 2 out of the 71 original bursts have too few events to properly analyze (fewer than 10 events). For the remaining 69 bursts, we apply the weighted least-square method to model the linear migration of seismicity onset times (i.e., the lower edge of the upper-triangle function in time versus distance

plots of seismicity), to compute the best-fitting migration directions and velocities, following the equation $t = t_0 + \vec{n} \cdot (\vec{X} - \vec{X_0})/v$, where $\vec{n}$ is the migration direction, v is migration velocity, t_0 is the timing of the first event, and $\vec{X_0}$ is the location of the first event. The estimated velocities generally appear slower than swarms within the Salton Trough (henceforth referred to as SS-swarms) (CS2011), and are mostly below 0.01 km/hour. We then apply a statistical resampling method to obtain a statistical significance (s_m) for the migration behavior of each burst. This method works by randomly 'scrambling' the occurrence time of each event in the sequence, and then applying the least-squares method to find the minimum misfit for each resampled dataset. This procedure is repeated 100 times for each burst, and s_m is defined as the percentage of higher misfits from the resampled dataset compared with the original dataset. The computed s_m values range from 0.5 to 1.0 for all bursts, with generally higher values for the 18 'swarm-like' bursts in VS2006 and lower values for the 'aftershock-like' bursts. We separate the 69 bursts into two groups based on s_m, in which 37 bursts (including 14 'swarm-like' bursts) with $s_m \geq 0.8$ are defined as the migration group, and 32 bursts (including 12 'aftershock-like' bursts) with $s_m < 0.8$ are defined as the non-migration group. For each burst, we compute the normalized distance using $d_n = \vec{n} \cdot (\vec{X} - \vec{X_0})/v$ with the best-fitting migration direction $(\vec{n})$ and velocity (v). To illustrate differences in the migration behavior among each group, we combine (stack) data from all bursts within the same group, and plot normalized distance versus time for each event. Shown by Figure 4.1a, the seismicity onset of the migration group aligns well with the best-fitting straight line, while the seismicity of the non-migration group (Figure 4.1b) centers within a narrow region regardless of time. The uncertainty of migration directions within the migration group is estimated to be 15° with respect to the median value from the resampling method.

4.3 Statistical characteristics

The overlap with the categories in VS2006 indicates the migration group is similar to swarms, while the non-migration group is similar to mainshock-

aftershock sequences. To explore differences between the two groups, we compute a set of parameters for each of the bursts, and identify differences among the statistical distributions within each group. Similar to the SS-swarms, we compute the parameter t_{max}, which is the time delay of the largest event normalized by the mean time delay within the burst. We also compute the skew of the seismic moment release μ, calculated from the third moment and standard deviation of the seismic moment time history (details in CS2011). μ is generally lower for swarms, and higher for aftershock sequences [*Roland and McGuire*, 2009]. In addition to these two parameters associated with the event magnitude, we compute two other parameters to quantify the spatial distribution of the bursts. Parameter $\Delta\sigma_{quasi} = \frac{7\sum_1^n M_0^i}{16r^3}$ (r is the mean radius of the burst) quantifies the total moment release relative to the area of the burst. *Roland and McGuire* [2009] showed that swarms on transform faults generally have lower $\Delta\sigma_{quasi}$ and lower μ compared with mainshock-aftershock sequences. Another parameter, d_s, measures the distance separation between the centers of the first half and second half of each burst, normalized by the mean radius of the burst, which provides an alternate measurement of the spatial migration.

We compute the parameters t_{max}, μ, $\Delta\sigma_{quasi}$ and d_s for the 69 bursts, and compare the CDF (cumulative density function) of the distribution for each parameter. For comparison, we also compute the same parameter set for the SS-swarms and the Brazil swarm. The Brazil swarm features μ of 1.1, t_{max} of 0.7, d_s of 0.5, and $\Delta\sigma_{quasi}$ of 0.4, close to the median values for the migration group and SS-swarms, with a slight lower $\Delta\sigma_{quasi}$. Shown in Figure 4.2, the migration group has similar parameter distributions to the SS-swarms. For μ (Figure 4.2b), we find that the SS-swarms and the migration group have very similar distributions, which are limited to a range between -3 and 5, while the non-migration group extends from 0 to about 45. Higher μ values indicate the energy release is concentrated at the beginning of the sequence, consistent with lower t_{max} for the non-migration group (see Figure 4.2c). Figure 4.2d shows the distance separation between the first and second halves for the SS-swarms. As expected, this separation is much greater for the migration group than the non-migration group.

For the $\Delta\sigma_{quasi}$ parameter (Figure 4.2a), the SS-swarms and the migration group have median values around 3 MPa, while the non-migration group has median values around 8 MPa, higher than the other two groups, which indicates the total moment release is centered in a relatively small region. To investigate whether the $\Delta\sigma_{quasi}$ values have any relationship to stress drops for individual earthquakes, we compare the values with stress drop estimates ($\Delta\sigma$), available for some of the events from *Shearer et al.* [2006]. We find 39 bursts have at least 10 events with stress drop estimates, of which 21 bursts fall within the migration group and 18 within the non-migration group. We compute the correlation coefficient and significance of correlation between $\Delta\sigma_{quasi}$ and median $\Delta\sigma$ based on a *t*-test. We apply a bootstrap method to obtain the distribution of correlation coefficients and the significance based on 1000 resampled datasets. Including all bursts, the correlation coefficient between $\Delta\sigma_{quasi}$ and median $\Delta\sigma$ is 0.1, and is only significant at the 50% confidence level. For the migration group, the correlation is around 0.4, and is significant at over 90% confidence; however, the non-migration group has a slightly negative correlation of -0.15 at a confidence level of 50%. For comparison, the SS-swarm has a coefficient of 0.4 at a confidence level of 90%, similar to the migration group. The correlation results show that the 'swarm-like' migration group is more correlated to the average single event stress drop estimates, although not very strongly, while the 'aftershock-like' non-migration group is barely correlated at all. The rupture area and the total moment for a mainshock-aftershock sequence is mostly dominated by the mainshock, so $\Delta\sigma_{quasi}$ should approximate the mainshock stress drop, and not necessarily correlate to individual aftershock stress drops. Unfortunately, due to waveform clipping problems, the *Shearer et al.* [2006] study does not include stress drop estimates for events larger than about M 3.5, so we cannot compare our results directly to mainshock stress drops.

Another important feature is the deviation of the temporal event distribution from Omori's power-law decay curve. Individual bursts exhibit variations in their temporal distributions, so to examine the general features of the two groups, we stack the delay times in each burst relative to the largest event within each group. Figure 4.3 shows that the migration group has about 50% of its seismicity

before the largest event, while the non-migration group is more similar to typical mainshock-aftershock sequences with very few events prior to the largest event. Despite the differences in the 'foreshocks' before the largest event, both groups exhibit power-law decay after the largest event in each sequence. The temporal distributions of SS-swarms and the Brazil swarm are similar to the migration group with an excess of seismicity before the largest event and Omori-like decay afterward. Such Omori-like decay indicates that some earthquake-to-earthquake triggering is likely significant even for the migration group [*Hainzl and Ogata*, 2005]; however, it should be noted that individual bursts do not usually follow Omori-like decay as closely as the stacked result.

4.4   Fluid diffusion

In CS2011, the possibility of fluid movement as a driving force is analyzed for some swarms within the Salton Sea geothermal field, where continuous injection and production are conducted. To investigate possible fluid involvement for the 69 bursts, we apply the same fluid diffusion modeling procedure used in CS2011. We use a similar weighted least-squares method to find the best-fitting diffusion coefficient based on the migration of seismicity onset, following the equation $|\vec{X} - \vec{X_0}| = \sqrt{4\pi D(t - t_0)}$, where D is the diffusion coefficient. To apply the least-squares method, we modify the equation to $t = t_0 + |\vec{X} - \vec{X_0}|^2/(4\pi D)$, and solve for D. A similar resampling method is used to find the statistical significance s_m. For each burst, we apply a bootstrap method to compare the misfit from the two models. The least-squares procedures are applied to 100 resampled datasets, and the misfits from the two models are compared for each dataset. We find 18 bursts have overall lower misfits with the diffusion model, which are all within the previously defined migration group of 37 bursts. We consider these 18 bursts as likely driven by fluid diffusion, of which 15 bursts have diffusion coefficients ranging from 0.01 to 0.16 m^2/s and 3 bursts have higher coefficients from 0.4 to 0.8 m^2/s. The uncertainty of the coefficients is estimated to be about 10% from the bootstrap test. Of the 6 bursts within the Coso geothermal field, 4 are better

fit with the fluid diffusion curve, similar to previous observations in the Salton Sea geothermal field, which indicated a high fraction of swarms that are fit with the diffusion curve (CS2011). To illustrate the diffusive migration behavior, we normalize distance using $d_n = |\vec{X} - \vec{X}_0|/\sqrt{4\pi D}$, and combine (stack) the 18 bursts to produce a distance versus time plot, shown in Figure 4.1c.

We also compare these results with the Brazil swarm, which was triggered by increased water level in the Açu Reservoir [*El Hariri et al.*, 2010]. We apply both the linear migration model and diffusion migration model to the waveform relocated catalog and compare the misfit from the two models. The migration significance is over 95% for both models, and the misfit from diffusion modelling is much lower than the linear migration model, consistent with a fluid triggering mechanism. We obtain a linear migration velocity of 38.4 m/d during peak seismicity, consistent with the velocity of 32-52.5 m/d obtained by *El Hariri et al.* [2010], and a diffusion coefficient of about 0.02 m^2/s, somewhat lower than the hydraulic diffusivity of 0.06 m^2/s obtained in *do Nascimento et al.* [2005], but within the same order, considering the wide range of diffusivities that have been reported (e.g., Talwani et al., 2007).

4.5   Focal mechanisms

So far, we have identified three types of bursts, the non-migration 'aftershock-like' bursts, linear migrating bursts, and bursts with apparent fluid involvement. VS2006 found that normal faulting mechanisms are usually associated with 'swarm-like' bursts, while 'aftershock-like' bursts are mainly associated with strike-slip and thrust faulting mechanisms. Here, we associate events from each burst with focal mechanism solutions from the HASH catalog [*Hardebeck and Shearer*, 2003], and then compute the focal mechanism type using the same method as VS2006, where -1 is normal faulting, 0 is strike-slip faulting and 1 is reverse faulting. We use focal mechanism solutions with quality A and B, and find 46 out of 69 bursts have at least one focal mechanism. We then separate the events into the three groups based on the burst type. As shown in Figure 4.4, the non-migration group has the most

reverse faulting mechanisms, the linear migration group is dominated by strike-slip faulting mechanisms, while the fluid-driven bursts have an excess of normal faulting mechanisms. Roughly speaking, about 70% of the reverse faulting events belong to the non-migration group and about 60% of the normal faulting events belong to the diffusive group. Strike-slip faulting is the dominant mechanism among all events, events of this type are evenly distributed among the three groups, and it is also the dominant focal mechanism among events in the SS-swarms and the Brazil swarm. Because these results could be dominated by a few large bursts, we also find the most common focal type and the focal type of the largest event with a focal mechanism solution for each burst. The results consistently show that the fluid-involved swarms have a higher fraction of normal-faulting mechanisms. As shown in Figure 4.5, south of the Garlock Fault, the fluid associated bursts are mostly distributed within the San Jacinto Fault Zone, the San Andreas Fault-Coachella zone, and the Eastern California Shear Zone, where high focal mechanism heterogeneity and substantial normal faulting are found [*Bailey et al.*, 2010]. However, the higher fraction of reverse faulting seen within the non-migration group is not obvious, as both the linear migrating swarms and the non-migration group are dominated by strike-slip faulting mechanisms.

We also compare the migration directions with focal mechanism orientations of the largest event in each burst. The migration directions are mostly at about 5° to 30° to one of the best-fitting focal planes, and are mostly within 30° of the seismicity strike direction. Considering the uncertainty of 15° for the migration direction estimates, this result indicates rough agreement between the focal mechanism orientations and migration directions. However, the directions usually do not follow surface fault traces, especially for the fluid associated bursts (see Figure 4.5), which include most normal faulting components. As noted by *Bailey et al.* [2010], for non strike-slip faulting types, the dominant focal mechanism orientations usually do not agree with surface traces, and may sample secondary fault structures.

4.6   Discussion

There have been many studies on fluid diffusivity using migration of micro-seismicity within geothermal areas, gas field, rift, volcanic regions, etc. *Talwani et al.* [2007] analyzed over 90 cases of induced seismicity from reservoir and geothermal injection experiments, and found the hydraulic diffusivities lie between 0.1 and 10 m^2/s. *Shapiro et al.* [2005] obtained a diffusivity of 0.023 m^2/s by fitting seismicity fronts triggered during a hydraulic fracturing test in Soultz (France), which is consistent with the diffusivity obtained based from a borehole injection/flow test. The diffusivities for Southern California are mostly between 0.01 and 0.16 m^2/s, consistent with values for other geothermal regions (obtained from hydraulic fracturing tests), water reservoirs and rift-related swarms, which range between 0.02 to 0.25 m^2/s [*Audigane et al.*, 2001; *Shapiro et al.*, 2005; *do Nascimento et al.*, 2005; *Pacchiani and Lyon-Caen*, 2010]. The values are slightly lower than diffusivities obtained for volcanic regions, which are generally between 0.2 to 0.7 m^2/s [*Shapiro et al.*, 2005; *Parotidis et al.*, 2005; *Yukutake et al.*, 2011]. The diffusive bursts are mostly distributed between 0 and 15 km depth. There is a hint of decreasing diffusivity with depth between 2 and 6 km, but this trend is less clear for deeper bursts.

Some swarms feature episodes with different diffusivities. *Parotidis et al.* [2005] obtained diffusivities ranging from 0.3 to 10 m^2/s for different episodes of seismicity during the 2000 Vogtland swarm, and suggested hydraulic heterogeneities as a possible cause. We find two swarms within the Coso geothermal region are best explained with two different diffusion curves, both starting with lower diffusivity and continuing with higher diffusivity. The swarm starting on 08/12/1984 began with lower diffusivity at shallower depth, and continued to deeper depths with a higher diffusivity; the swarm starting on 08/01/1992 began with lower diffusivity at deeper depth along a NE-SW strike, and continued to shallower depth at SE-NW strike with higher diffusivity (see Figure 4.6). The different migration behaviors within the same swarm may arise from different diffusivity patches that account for hydraulic heterogeneities.

The linear migration velocities for swarms within the linear migration group

are mostly below 0.01 km/hour, about an order of magnitude lower than the average migration velocities for the SS-swarm (CS2011) and swarms along transform faults [*Roland and McGuire*, 2009]. The typical aseismic slip velocity is on the order of 0.1 km/hour to 1.0 km/hour [*Roland and McGuire*, 2009; and references therein]. Our low observed velocities for these swarms are more comparable to fluid-driven migrations [e.g., *Hainzl and Ogata*, 2005], but we nonetheless achieve better data fits with a constant linear velocity than with a diffusion curve. Thus, these swarms may have been triggered by slower or weaker aseismic slip than previous work has suggested is typical for slow-slip events. Future analysis with Epidemic Type Aftershock Sequence (ETAS) models and physical seismicity models based on rate and state friction laws may help to reveal additional information [e.g., *Hainzl and Ogata* 2005; *Llenos and McGuire*, 2011].

4.7   Conclusions

We examine 69 seismicity bursts across southern California to quantify the spatial migration of their events and to explore differences in their behavior as defined by parameters that describe the time history of moment release and stress drop estimates. Bursts that do not exhibit significant migration(with migration significance $s_m < 0.8$) have low t_{max}, low d_s, high μ and high $\Delta\sigma_{quasi}$, and are mostly aftershock-like sequences, while bursts with high s_m feature high t_{max}, high d_s, low μ and low $\Delta\sigma_{quasi}$, are more 'swarm-like'. Through diffusive migration behavior modeling, we find over half of the migration bursts are better-fitted to a diffusive curve with similar parameters to a well-recorded RIS sequence, indicating fluid involvement, and the diffusivities are consistent with previous studies for geothermal reservoirs. The focal mechanism solutions for the fluid-involved bursts show a high fraction of normal faulting mechanisms, consistent with the hypothesis of an extensional stress field for geothermal reservoirs. Further analysis with ETAS modeling and physical models may help to further explain this behavior.

Acknowledgments

References

Audigane, P., J. J. Royer, and H. Kaieda (2002), Permeability characterization of the soultz and ogachi large-scale reservoir using induced microseismicity, *Geophysics*, *67*(1), 204–211.

Bailey, I. W., Y. Ben-Zion, T. W. Becker and M. Holschneider (2010), Quantifying focal mechanism heterogeneity for fault zones in central and southern California, *Geophys. J. Int. 183*, 433-450, doi: 10.1111/j.1365-246X.2010.04745.x.

Chen, X., and P. M. Shearer (2011), Comprehensive analysis of earthquake source spectra and swarms in the salton trough, california, *J. Geophys. Res.*, *116*(B09309), doi:10.1029/2011JB008263.

Daniel, G., E. Prono, F. Renard, F. Thouvenot, S. Hainzl, D. Marsan, A. Helmstetter, P. Traversa, J. L. Got, L. Jenatton, and R. Guiguet (2011), Changes in effective stress during the 2003-2004 Ubaye seismic swarm, France, *J. Geophys. Res.*, *116*, B01309, doi:10.1029/2010JB007551.

do Nascimento, A. F., Cowie, P. A., Lunn, R. J. and Pearce, R. G. (2004) Spatio-temporal evolution of induced seismicity at Açu reservoir, NE Brazil, *Geophys. J. Int. 158*, 1041-1052.

do Nascimento, A. F., Lunn, R. J. and Cowie, P. A., (2005) Modeling the heterogeneous hydraulic properties of faults using constraints from reservoir-induced seismicity, *J. geophys. Res., 110*, B09201, doi:10.1029/2004JB003398.

El Hariri, M., R. E. Abercrombie, C. A. Rowe, and A. F. do Nascimento (2010), The role of fluids in triggering earthquakes: observations from reservoir induced seismicity in brazil, *Geophysical Journal International, 181*(3), 1566–1574.

Julian, B. R., G. R. Foulger, F. C. Monastero, and S. Bjornstad (2010), Imaging hydraulic fractures in a geothermal reservoir, *Geophys. Res. Lett., 37*, L07305, doi:10.1029/2009GL040933.

Kato, A., K. Obara, T. Igarashi, H. Tsuruoka, S. Nakagawa, and N. Hirata (2012), Propagation of slow slip leading up to the 2011 m-w 9.0 tohoku-oki earthquake, *Science, 335*(6069), 705–708.

Hainzl, S., and Y. Ogata (2005), Detecting fluid signals in seismicity data through statistical earthquake modeling, *J. Geophys. Res., 110*, B05S07, doi:10.1029/2004JB003247.

Hardebeck, J. L., and P. M. Shearer (2003), Using s/p amplitude ratios to constrain the focal mechanisms of small earthquakes, *Bulletin of the Seismological Society of America, 93*(6), 2434–2444.

Hayashi, Y. and Y. Morita (2003), An image of a magma intrusion process inferred from precise hypocentral migrations of the earthquake swarm east of the Izu peninsula, *Geophysical Journal International, 153*(1), 159-174.

Hough, S. E., R. S. Dollar and P. Johnson (2000), The 1998 earthquake sequence south of Long Valley Caldera, California: Hints of magmatic involvement, *Bull. Seismol. Soc. Am., 90*(3), 752-763.

Lin, G., P. M. Shearer, and E. Hauksson (2007), Applying a three-dimensional velocity model, waveform cross correlation, and cluster analysis to locate southern California seismicity from 1981 to 2005, *J. Geophys. Res., 112*, B12309, doi:10.1029/2007JB004986.

Llenos, A. L., and J. J. McGuire (2011), Detecting aseismic strain transients from seismicity data, *J. Geophys. Res., 116*, B06305, doi:10.1029/2010JB007537.

Lohman, R. B. and J. J. McGuire (2007), Earthquake swarms driven by aseismic creep in the Salton Trough, California, *J. Geophys. Res. 112*, B04405, 10.1029/2006JB004596.

Pacchiani, F. and H. Lyon-Caen (2011), Geometry and spatio-temporal evolution of the 2001 Agios Ioanis earthquake swarm (Corinth Rift, Greece), *Geophys. J. Int., 180*(1), 59-72.

Parotidis, M., S. A. Shapiro, and E. Rothert (2005), Evidence for triggering of the Vogtland swarms 2000 by pore pressure diffusion, *J. Geophys. Res., 110*, B05S10, doi:10.1029/2004JB003267.

Roland, E., and J. J. McGuire (2009), Earthquake swarms on transform faults, *Geophysical Journal International, 178*(3), 1677–1690.

Shapiro, S. A., R. Susanne and E. Rothert (2005), Characterization of hydraulic properties of rocks using probability of fluid-induced microearthquakes, *Geophysics, 70*(2), 27-33.

Shearer, P. M., G. A. Prieto, and E. Hauksson (2006), Comprehensive analysis of earthquake source spectra in southern california, *Journal of Geophysical Research-Solid Earth, 111* B06303, doi:10.1029/2005JB003979.

Talwani, P., L. Chen, and K. Gahalaut (2007), Seismogenic permeability, ks, *J. Geophys. Res., 112*, B07309, doi:10.1029/2006JB004665.

Vidale, J. E., and P. M. Shearer (2006), A survey of 71 earthquake bursts across southern California: Exploring the role of pore fluid pressure fluctuations and aseismic slip as drivers, *J. Geophys. Res., 111*, B05312, doi:10.1029/2005JB004034.

Yukutake, Y., H. Ito, R. Honda, M. Harada, T. Tanada and A. Yoshida (2011), Fluid-induced swarm earthquake sequence revealed by precisely determined hypocenters and focal mechanisms in the 2009 activity at Hakone volcano, Japan, *J. Geophys. Res., 116*, B04308, doi:10.1029/2010JB008036.
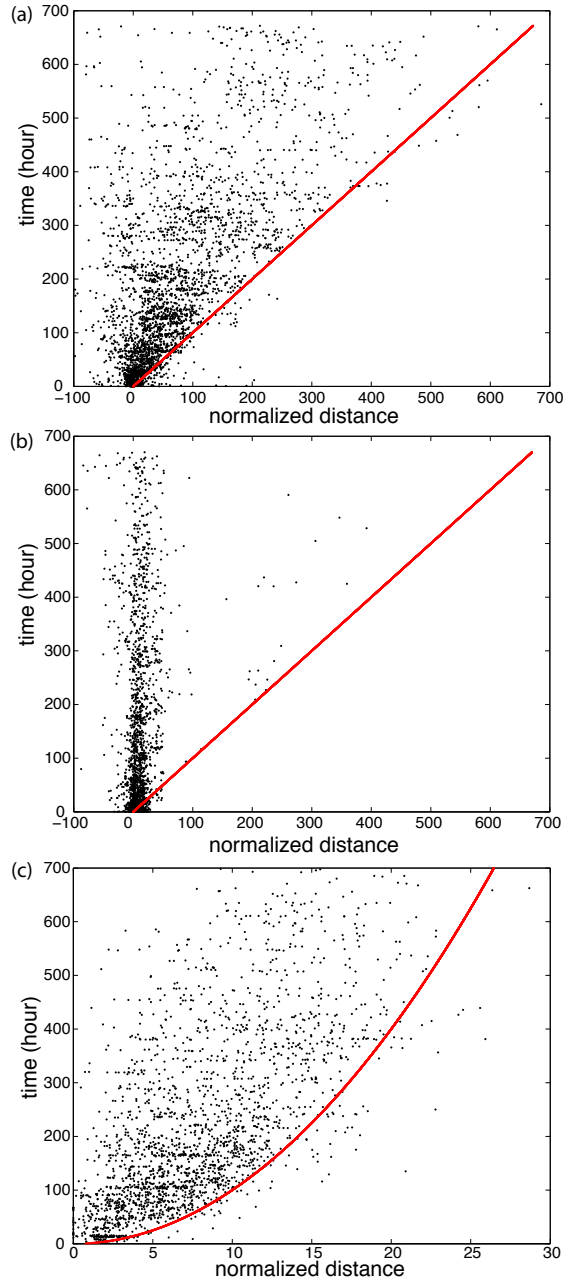
Figure 4.1: (a) Stacked time versus normalized distance migration behavior for 37 bursts with migration significance ≥ 0.8. (b) Stacked normalized migration behavior for 32 bursts with migration significance <0.8. (c) Stacked normalized diffusion migration curve for 18 bursts. Red lines in (a) and (b) represent normalized distance following $d = t - t_0$, red line in (c) represents normalized distance following $d = \sqrt{t - t_0}$.
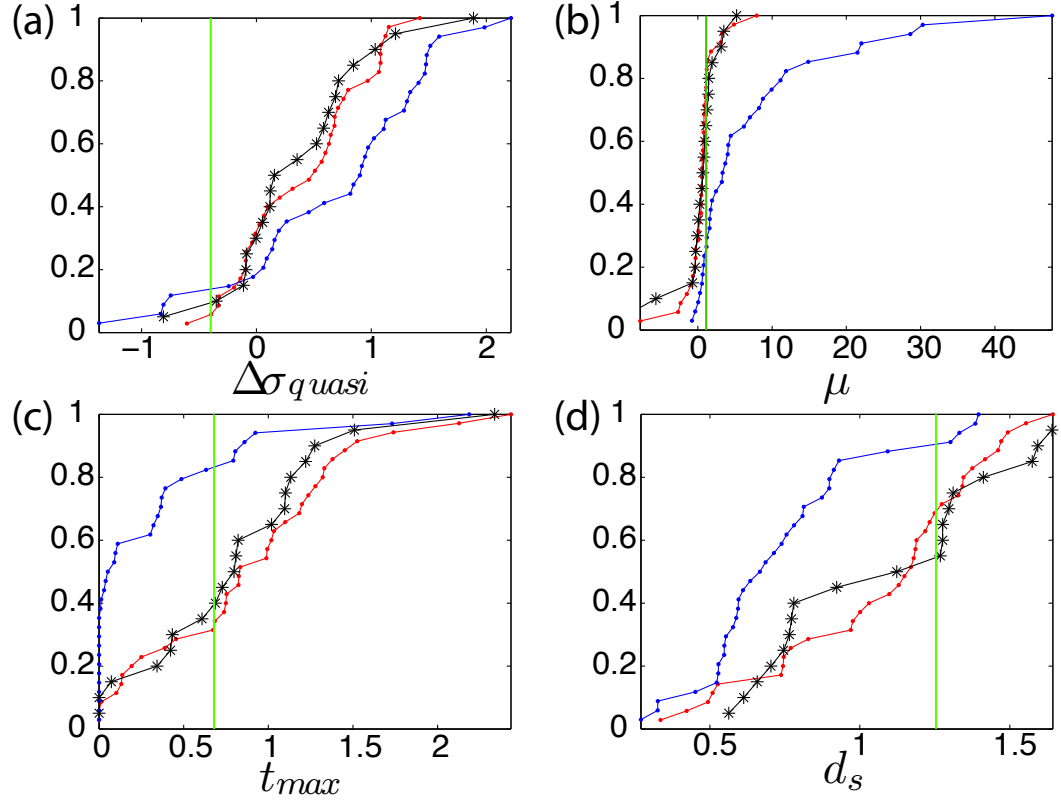
Figure 4.2: Cumulative distribution functions (CDFs) for different burst categories, as a function of (a) effective stress drop (log scale), (b) skew of seismic moment release, (c) time delay of the largest event normalized by the mean time delay, and (d) the normalized distance separation between the first and second half of the burst. Results for swarms in the Salton Trough from *Chen and Shearer* [2011] are shown in black, bursts from *Vidale and Shearer* [2006] with $s_m \geq 0.8$ are shown in red, bursts with $s_m < 0.8$ are shown in blue, results for the Brazil swarm are shown in green.
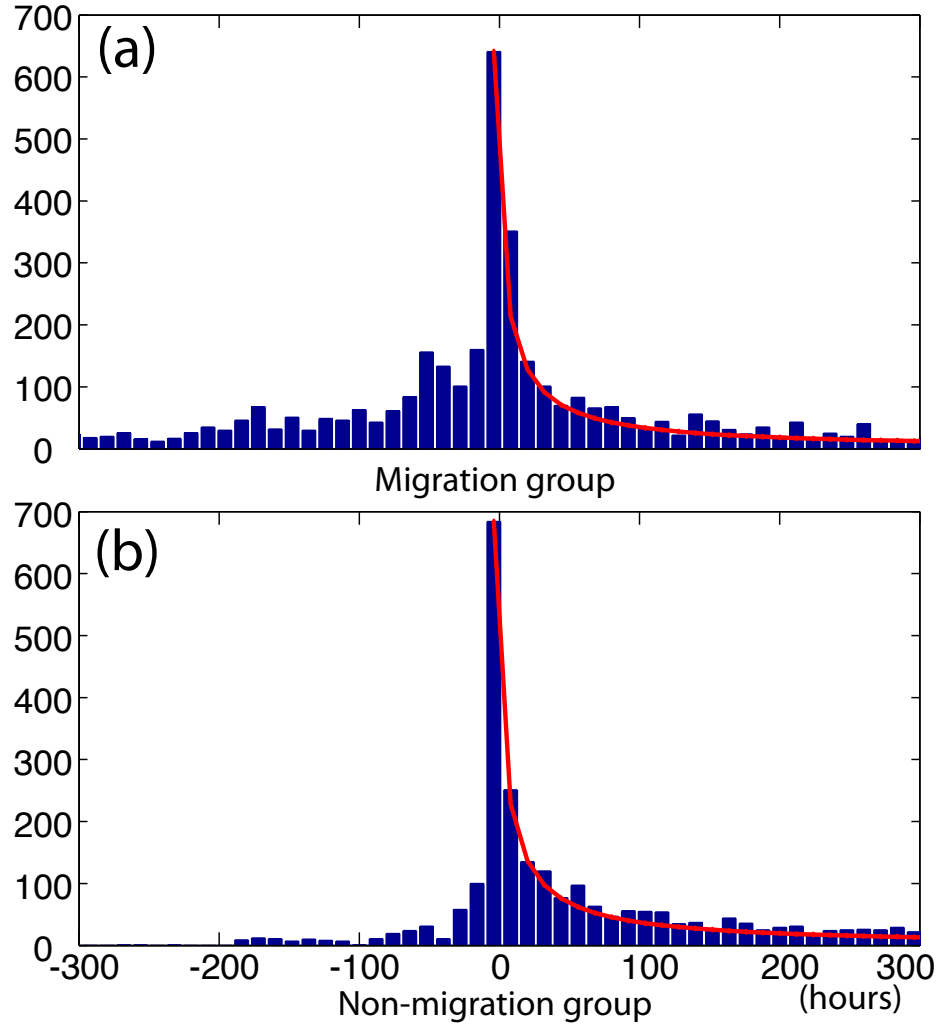
Figure 4.3: (a) Temporal distribution for events within bursts with high migration significance ($s_m \geq 0.8$). (b) Temporal distribution for bursts with low migration significance ($s_m < 0.8$). Red lines are the predicted t^{-1} decay curves.
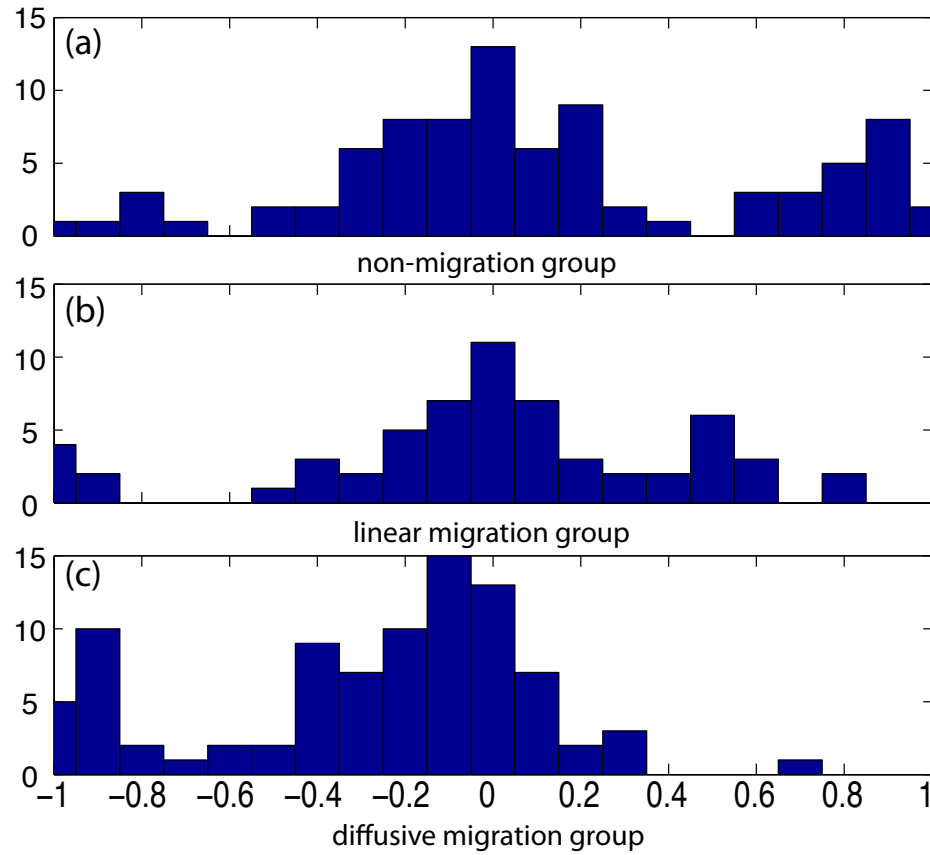
Figure 4.4: Focal mechanism distribution for events within (a) the non-migration group, (b) the linear migration group, and (c) the fluid diffusion group. -1 corresponds to normal faulting, 0 corresponds to strike-slip faulting, and 1 corresponds to reverse faulting.
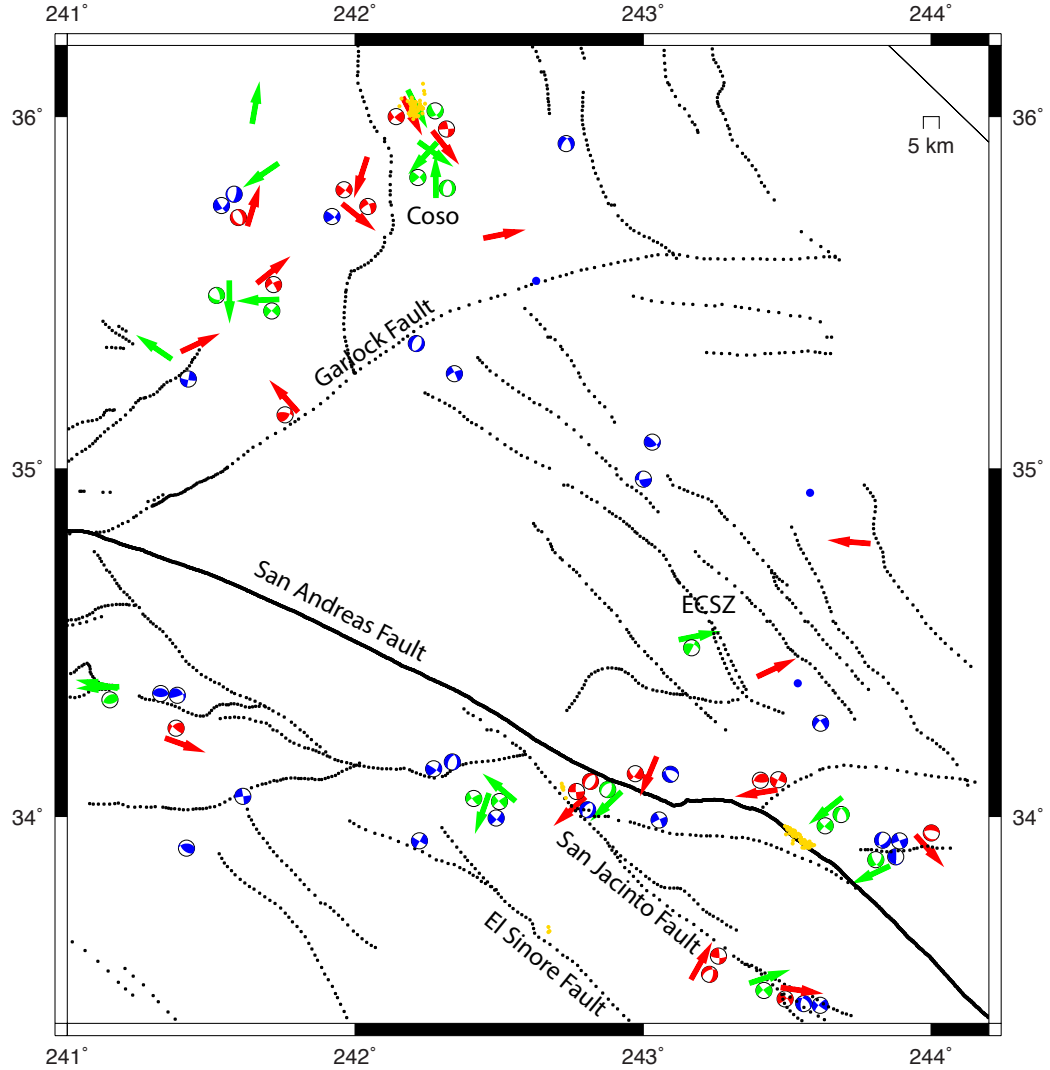
Figure 4.5: Map view of burst locations, major focal mechanisms and migration directions. Yellow dots are the geothermal well locations (data from California Conservation Department website). Arrows are the best-fitting directions for bursts within the migration group. Green color indicates bursts best fit with diffusion curves. Red color indicates bursts with $s_m \geq 0.8$. Blue color indicates bursts with $s_m < 0.8$ and no clear migration directions. Focal mechanisms are from *Hardebeck and Shearer* [2003], the focal type of the largest available earthquake and second largest available earthquake with a different focal type are plotted for each burst. If no focal mechanism or migration is available for a burst, a dot of corresponding color is plotted.
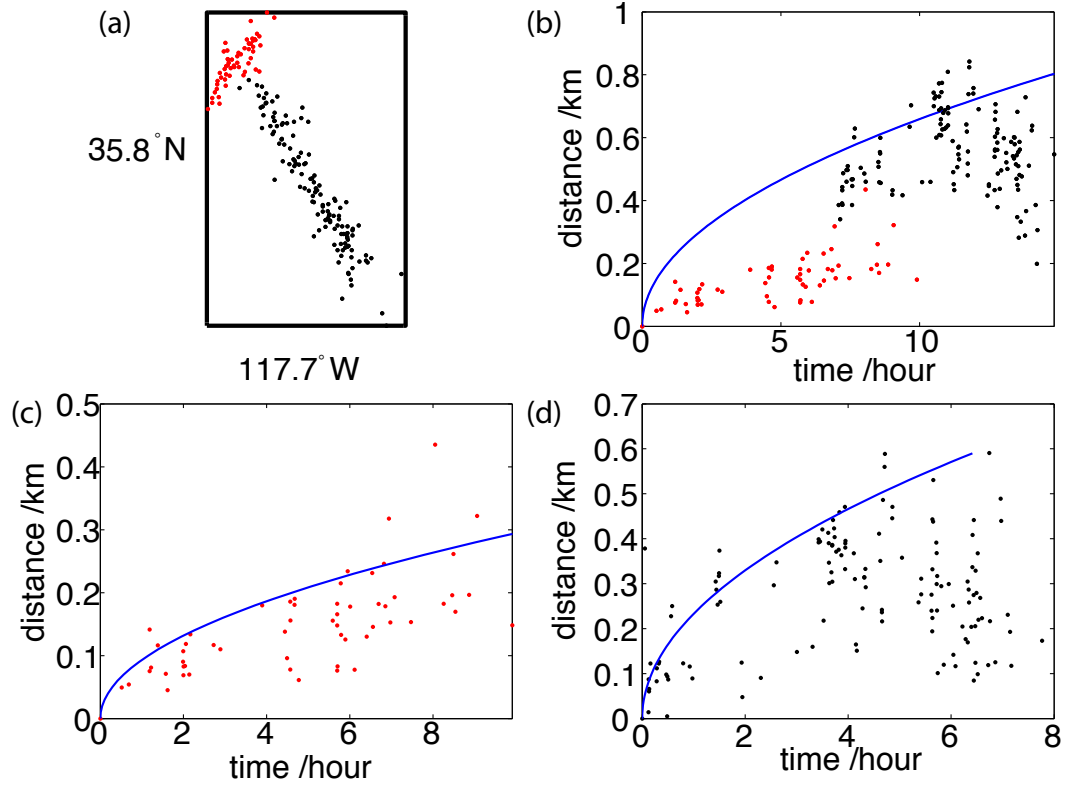
Figure 4.6: (a) Map view of events within a swarm starting on 08/01/1992 in Coso geothermal field. (b) Best-fitting diffusive migration curve for all events with D=0.04 m^2/s. (c) Best-fitting diffusive curve for the NE-SW striking events at the early stage of the swarm with D=0.008 m^2/s. (d) Best-fitting diffusive curve for the SE-NW striking events at the later part of the swarm with D=0.05 m^2/s. Red dots correspond to events in figure (c), black dots corresponds to events in figure (d). Blue lines in figures (b), (c) and (d) are the predicted migration curve with corresponding diffusion coefficients in each figure. Distance in figures (b), (c) and (d) is relative to the first event in each figure.

Chapter 5

California foreshock sequences suggest aseismic triggering process

Foreshocks are one of the few well-documented precursors to large earthquakes; therefore, understanding their nature is very important for earthquake prediction and hazard mitigation. However, the triggering role of foreshocks is not yet clear. It is possible that foreshocks are a self-triggering cascade of events that simply happen to trigger an unusually large aftershock; alternatively, foreshocks might originate from an external aseismic process that ultimately triggers the mainshock. In the former case, the foreshocks will have limited utility for forecasting. The latter case has been observed for several individual large earthquakes, however, it remains unclear how common it is, and how to distinguish foreshock sequences from other seismicity clusters that do not lead to large earthquakes. Here, we analyze foreshocks of three M > 7 mainshocks in southern California. These foreshock sequences appear similar to earthquake swarms, in that they do not start with their largest events and they exhibit spatial migration of seismicity. Analysis of source spectra shows that all three foreshock sequences feature lower average stress drops and depletion of high-frequency energy compared with their corresponding aftershocks. Using a longer-term stress drop catalog, we find that the average stress drop of the Landers and Hector Mine foreshock sequences

are comparable to nearby swarms. Our observations suggest that these foreshock sequences are manifestations of aseismic transients occurring close to the main-shock hypocenters, possibly related to localized fault zone complexity, which have promoted the occurrence of both the foreshocks and the eventual mainshocks.

5.1   Introduction

Foreshock sequences are the most obvious precursor to large earthquakes; therefore, understanding their origin and relation to mainshocks is of great importance for earthquake prediction and hazard mitigation. Previous studies of immediate foreshocks in California suggest that these events may be part of a mainshock rupture nucleation process, because estimated Coulomb stress changes from foreshocks are too small to produce stress triggering and observed foreshock areas scale with mainshock magnitude, consistent with nucleation rather than earthquake-to-earthquake triggering (*Dodge et al.*, 1996). For the 1999 Izmit earthquake, accelerating repeating events originating from near the mainshock hypocenter suggest an extended nucleation process (*Bouchon et al.*, 2012). For the 2011 Tohoku earthquake, a quasi-static slip transient was observed from foreshock sequences with repeating earthquakes, but its properties differ from expectation from the pre-slip nucleation model (*Ando and Imanishi*, 2012; *Kato et al.*, 2012). Despite the observations for several individual earthquakes, however, some questions remain unclear: whether the aseismic triggering process would generalize to other mainshocks; is there any physical properties that distinguish foreshocks from other sequences. Here, we use a recently compiled high-resolution earthquake catalog (*Hauksson et al.*, 2012), and apply a source spectral analysis method (*Shearer et al.*, 2006) to study foreshock sequences in southern California and compare their properties to other nearby earthquakes.

5.2 Spatial-temporal pattern

There are three M > 7 earthquakes in the catalog since 1981: 1992 Mw 7.3 Landers, 1999 Mw 7.1 Hector Mine, and 2010 Mw 7.2 El Mayor-Cucapah (Figure 5.1). All of them are all dominated by strike-slip faulting (a normal-faulting sub-event exists for the El Mayor-Cucapah earthquake), located along secondary faults adjacent to the main North America-Pacific plate boundary (*Hauksson et al.*, 2012). The Landers earthquake is preceded by 27 cataloged foreshocks within 7 hr and 1.5 km. The Hector Mine earthquake has 18 cataloged foreshocks within 24 hr and 0.5 km. The El Mayor-Cucapah earthquake is preceded by an extended foreshock sequence, which is separated into two distinct time periods: the first occurred on March 21, and the second occurred on April 3, 30 hr before the mainshock; the foreshocks extend up to 6 km from the mainshock. The foreshock magnitudes range from 1.2 to 4.4 for all three cases with no clear "mainshock" within the foreshock sequences (Figure 5.2).

To obtain greater relative location accuracy between the mainshock hypocenters and their foreshock sequences, we first apply a custom relocation method (see Methods). We then use a weighted-L1-norm approach (*Chen and Shearer*, 2011) to model the spatial migration of the foreshock sequences (Figure S1). The Landers foreshock sequence is separated into two periods: the first starts at -7 hr, lasts about 2 hours, and spreads across the entire foreshock region; the second starts at -2.5 hr, and migrates northward toward the mainshock at about 0.6 km/hr. The El Mayor-Cucapah sequence exhibits similar behavior: the first part quickly spans almost the entire foreshock region, and the second part migrates northward at about 0.5 km/hr. The Hector Mine foreshock sequence also migrates northward, but at a much lower velocity of about 0.03 km/hr, similar to swarms thought to be triggered by fluid flow (*Chen et al.*, 2012). Modeling this sequence with fluid diffusive migration yields a slightly lower misfit compared to the linear migration model; the best-fitting diffusion coefficient is 0.2 m^2/s, consistent with swarms in the Salton Trough (*Chen and Shearer*, 2011).

All of the foreshock sequences appear associated with fault zone complexity (Figure 5.1). The Landers foreshocks are located at a jog between two fault seg-

ments (*Dodge et al.*, 1996). The Hector Mine foreshocks are located at a branch of the main fault trace and the foreshocks themselves define a small branch (Figure S1). The El Mayor-Cucapah foreshocks outline a nearly north-south striking fault plane, whereas the main fault trace strikes N50^{o}W (*Hauksson et al.*, 2011). The El Mayor-Cucapah mainshock initiated on an extensional jog at depth, with a similar strike but different dip as a M 4.4 foreshock (*Hauksson et al.*, 2011; *Wei et al.*, 2012). In all three cases, the final stage of migration started at a region of local complexity in the fault zone (Figure S1).

5.3   Source spectra

For each mainshock sequence, we obtain event source spectra from an iterative de-convolution method, and compute event stress drop using an empirical Greens function method (*Shearer et al.*, 2006; *Madariaga*, 1976). The stress drops follow a log-normal distribution and do not depend on event magnitude, indicating self-similar behavior. We compare the median stress drops for foreshocks and aftershocks within 3.3 km (6.6 km for El Mayor-Cucapah) and 5 days from each mainshock, and find that the median foreshock stress drops are substantially lower than that of the corresponding aftershocks (Figure 5.3). It is possible that attenuation changes after a large earthquake could affect the EGF-corrected source spectra and the stress-drop estimates. To test for this possibility, we compute separate EGFs for the foreshocks and aftershocks, and estimate the change in t* from their spectral ratio (*Shearer*, 2009). The increase in t* suggests increased attenuation after the mainshocks (Figure S2). However, due to the limited number of available foreshock source spectra, this result is not stable with respect to the choice of different magnitude bins and thus these attenuation changes are not reliably resolved. Nonetheless, it seems unlikely that our result (lower stress drop estimates for foreshocks) is an artifact of attenuation changes, because this would require attenuation to decrease as a result of the mainshock, opposite to what previous studies have found. For example, increased attenuation was observed following the 1989 Loma Prieta and 2004 Parkfield earthquakes, possibly due to

increased pore creation and fault zone damage after the mainshock (*Chun et al.*, 2004; *Allmann and Shearer*, 2007).

The absolute level of our estimated stress drops depends upon a number of modeling assumptions (e.g., assumed rupture velocity, etc.), but the relative differences indicate variations in the source spectra that are robust with respect to our modeling choices. To confirm these differences, we directly compare the stacked foreshock and aftershock spectra, and find that foreshock spectra are consistently depleted in high-frequency energy, and exhibit a faster fall-off rate than the aftershock spectra. To validate our deconvolution process, we also examine the P-wave spectra at individual stations, and find the original displacement spectra exhibit similar behavior (see example in Figure S3). These results indicate that the observed differences in median stress drop reflect real differences in the earthquake source spectra.

To better understand the short-term stress-drop variations occurring at the time of the mainshock, it is important to examine the longer-term stress-drop behavior in the same region. Using the stress-drop catalog for southern California from 1989 to 2002 (*Shearer et al.*, 2006), we examined the complete stress-drop history within the vicinity of the Landers and Hector Mine mainshocks (Figure 5.4). The background seismicity prior to the Joshua Tree earthquake (about two months before the Landers earthquake) has generally higher stress drops than the ensuing aftershocks, but this is based on a relatively small number of events. Immediately prior to the two M>7 mainshocks, the foreshock stress drops are anomalously low compared to other seismicity in the region.

After the Landers earthquake, the median aftershock stress drops slowly increase, lessen immediately after the Hector Mine earthquake, and then again increase, perhaps indicating long-term fault zone recovery from large earthquakes (*Li et al.*, 1998). The foreshock stress drops are similar to other small seismicity bursts in this region (*Chen et al.*, 2012; *Vidale and Shearer*, 2006). Among the smaller bursts in Figure 5.4, bursts 49 and 64 are possibly secondary triggered aftershock sequences after the Landers and Hector Mine mainshocks. Burst 52 is an extended swarm sequence that migrated at very low speed (about 0.001 km/hr),

and was most likely triggered by a fluid signal (D=0.03 m^2/s). Burst 31 is a small swarm that does not show spatial migration. Overall, the Landers and Hector Mine aftershocks have median stress drops only slightly less than the southern California median of 1.8 MPa (*Shearer et al.*, 2006); it is the foreshock sequences and swarms in this region that have anomalously low stress drops.

5.4   Discussion

Quasi-static slip signals prior to rapid dynamic rupture have been observed from numerical modeling and laboratory observations (*Ohnaka and Shen*, 1999; *Lapusta and Rice*, 2003). Emergent onsets in seismic waveforms and immediate foreshock sequences have been interpreted to represent a slow nucleation process (*Dodge et al.*, 1996; *Ellsworth and Beroza*, 1995). However, the observed spatial-temporal evolution patterns for the foreshocks studied here differ from a nucleation-related pre-slip model. There is no temporal acceleration of foreshock occurrence, and the three similar sized mainshocks have very different foreshock areas and durations (Figure 5.2 and 5.3), suggesting no simple scaling relationship with mainshock magnitude (*Abercrombie and Mori*, 1996). Rather, the spatial pattern resembles features of earthquake swarms in the vicinity, where an external aseismic transient is likely involved.

For the Landers and El Mayor-Cucapah earthquakes, observations of smaller sub-events (*Wei et al.*, 2012; *Abercrombie and Mori*, 1994) indicate that the direct mainshock nucleation may start after the last observed foreshocks. It is interesting to note the association between fault zone complexity (*Jones*, 1984) and the foreshock migration pattern. Both numerical modeling and laboratory experiments have found that fault zone complexity is critical in the generation of smaller events (*Ohnaka and Shen*, 1999; *Lapusta and Rice*, 2003; *Rice and Ben-Zion*, 1996). For a constant shear loading on a rough fault, the shear stress accumulates non-uniformly along the fault zone with concentration at stronger positions. The failure starts at weaker positions and grows at 0.3 to 4 km/hr (*Ohnaka and Shen*, 1999), consistent with our observed foreshock migration rate. In this scenario, stress loading

from the external transient event accumulates within the localized area, in which abrupt failure events are promoted. Due to strong heterogeneity, the critical pore creation slip distance is small (*Yamashita*, 1999), and swarm-like behavior is generated. The transient event then causes stress loading at the mainshock hypocenter, which may trigger the eventual mainshocks. The origin and nature of the hypothesized transient event is unknown, but either slow slip or fluid flow could lead to reduced fault strength and lowered differential stress (*Chen and Shearer*, 2011; *Allmann et al.*, 2010), which could account for the smaller stress drops seen for the foreshocks. Not all large earthquakes are preceded by observable foreshock sequences and not all swarms lead to large earthquakes. But our results suggest that many foreshock sequences, like swarms, may reflect an underlying aseismic triggering process. For the Eastern California Shear Zone, small seismicity bursts are less frequent that in other parts of southern California (*Chen et al.*, 2012); therefore, at least in this region, burst occurrence may be a useful contributor to short-term earthquake probability estimates.

Acknowledgments

Chapter 5, in full, has been submitted to Geophysical Research Letters: Chen, X., and P. M. Shearer, California foreshock sequences suggest underlying aseismic process, submitted to *Geophysical Research Letters*. I am the primary investigator and author of the paper, in which we examine the foreshock sequences for three M>7 mainshocks in southern California. We apply the relocation and source spectra methods to analyze foreshock spatial patterns and compare their stress drops with those of immediate aftershock sequences.

References

Abercrombie, R., and J. Mori (1994), Local observations of the onset of a large earthquake - 28 june 1992 landers, california, *Bulletin of the Seismological Society of America*, *84*(3), 725–734.

Abercrombie, R. E., and J. Mori (1996), Occurrence patterns of foreshocks to large earthquakes in the western united states, *Nature*, *381*(6580), 303–307.

Allmann, B. P., and P. M. Shearer (2007), Spatial and temporal stress drop variations in small earthquakes near parkfield, california, *Journal of Geophysical Research-Solid Earth*, *112*(B4), 17.

Allmann, B. P., A. Goertz, and S. Wiemer (2010), Stress drop variations of induces earthquakes at the basel geothermal site, *Geophysical Research Letters*.

Ando, R., and K. Imanishi (2012), Possibility of m-w 9.0 mainshock triggered by diffusional propagation of after-slip from m-w 7.3 foreshock, *Earth Planets and Space*, *63*(7), 767–771.

Bouchon, M., H. Karabulut, M. Aktar, S. Ozalaybey, J. Schmittbuhl, and M. P. Bouin (2012), Extended nucleation of the 1999 m-w 7.6 izmit earthquake, *Science*, *331*(6019), 877–880.

Chen, X., and P. M. Shearer (2011), Comprehensive analysis of earthquake source spectra and swarms in the salton trough, california, *J. Geophys. Res.*, *116*(B09309).

Chen, X., P. M. Shearer, F. Walter, and H. A. Fricker (2011), Seventeen antarctic seismic events detected by global surface waves and a possible link to calving events from satellite images, *J. Geophys. Res.*, *116*(B06311).

Chen, X., P. M. Shearer, and R. Abercrombie (2012), Spatial migration of earthquakes within seismic clusters in southern california: Evidence for fluid diffusion, *J. Geophys. Res.*, *117*(B04301).

Chun, K.-Y., G. A. Henderson, and J. Liu (2004), Temporal changes in p wave attenuation in the loma prieta rupture zone, *J. Geophys. Res.*, *109*(B2), B02,317.

Dodge, D. A., G. C. Beroza, and W. L. Ellsworth (1996), Detailed observations of california foreshock sequences: Implications for the earthquake initiation process, *Journal of Geophysical Research-Solid Earth*, *101*(B10), 22,371–22,392.

Ellsworth, W. L., and G. C. Beroza (1995), Seismic evidence for an earthquake nucleation phase, *Science*, *268*(5212), 851–855.

Hauksson, E., J. Stock, K. Hutton, W. Z. Yang, J. A. Vidal-Villegas, and H. Kanamori (2011), The 2010 m (w) 7.2 el mayor-cucapah earthquake sequence, baja california, mexico and southernmost california, usa: Active seismotectonics along the mexican pacific margin, *Pure and Applied Geophysics*, *168*(8-9), 1255–1277.

Hauksson, E., W. Yang, and P. M. Shearer (2012), Waveform relocated earthquake catalog for southern california (1981 to june 2011), *Bulletin of the Seismological Society of America*, *102*(5), 2239–2244.

Jones, L. M. (1984), Foreshocks (1966-1980) in the san-andreas system, california, *Bulletin of the Seismological Society of America*, *74*(4), 1361–1380.

Kato, A., K. Obara, T. Igarashi, H. Tsuruoka, S. Nakagawa, and N. Hirata (2012), Propagation of slow slip leading up to the 2011 m-w 9.0 tohoku-oki earthquake, *Science*, *335*(6069), 705–708.

Lapusta, N., and J. R. Rice (2003), Nucleation and early seismic propagation of small and large events in a crustal earthquake model, *J. Geophys. Res.*, *108*(B4), 2205.

Li, Y. G., J. E. Vidale, K. Aki, F. Xu, and T. Burdette (1998), Evidence of shallow fault zone strengthening after the 1992 m7.5 landers, california, earthquake, *Science*, *279*(5348), 217–219.

Lin, G. Q., P. M. Shearer, and E. Hauksson (2007), Applying a three-dimensional velocity model, waveform cross correlation, and cluster analysis to locate southern california seismicity from 1981 to 2005, *Journal of Geophysical Research-Solid Earth*, *112*(B12), 14.

Madariaga, R. (1976), Dynamics of an expanding circular fault, *Bull. Seismol. Soc. Am.*, *66*, 639–666.

Ohnaka, M., and L. Shen (1999), Scaling of the shear rupture process from nucleation to dynamic propagation: Implications of geometric irregularity of the rupturing surfaces, *J. Geophys. Res.*, *104*(B1), 817–844.

Prieto, G. A., P. M. Shearer, F. L. Vernon, and D. Kilb (2004), Earthquake source scaling and self-similarity estimation from stacking p and s spectra, *J. Geophys. Res.*, *109*.

Rice, J. R., and Y. Ben-Zion (1996), Slip complexity in earthquake fault models, *Proc. Natl. Acad. Sci*, *93*, 3811–3818.

Shearer, P. M. (2009), *Introduction to Seismology*, second edition ed., Cambridge University Press.

Shearer, P. M., G. A. Prieto, and E. Hauksson (2006), Comprehensive analysis of earthquake source spectra in southern california, *Journal of Geophysical Research-Solid Earth*, *111* (B6).

Vidale, J. E., and P. M. Shearer (2006), A survey of 71 earthquake bursts across southern california: Exploring the role of pore fluid pressure fluctuations and aseismic slip as drivers, *Journal of Geophysical Research-Solid Earth*, *111* (B5).

Wei, S. J., E. Fielding, S. Leprince, A. Sladen, J. P. Avouac, D. Helmberger, E. Hauksson, R. S. Chu, M. Simons, K. Hudnut, T. Herring, and R. Briggs (2012), Superficial simplicity of the 2010 el mayor-cucapah earthquake of baja california in mexico, *Nature Geoscience*, *4* (9), 615–618.

Yamashita, T. (1999), Pore creation due to fault slip in a fluid-permeated fault zone and its effect on seismicity: Generation mechanism of earthquake swarm, *Pure and Applied Geophysics*, *155* (2-4), 625–647.
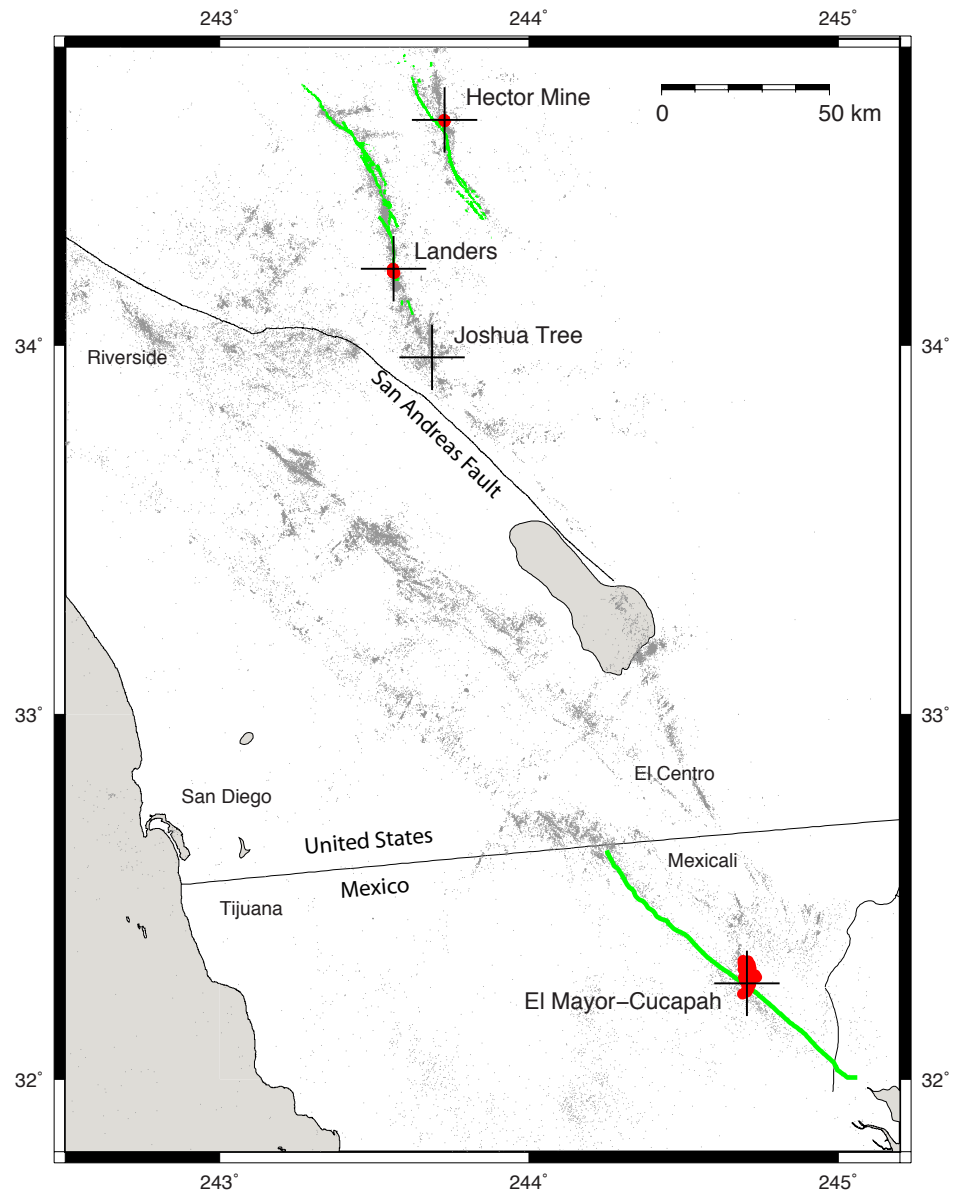
Figure 5.1: A map of southern California, showing the locations of three M >
7 mainshocks (black "+"), their foreshocks (red dots) and a random 2% of total
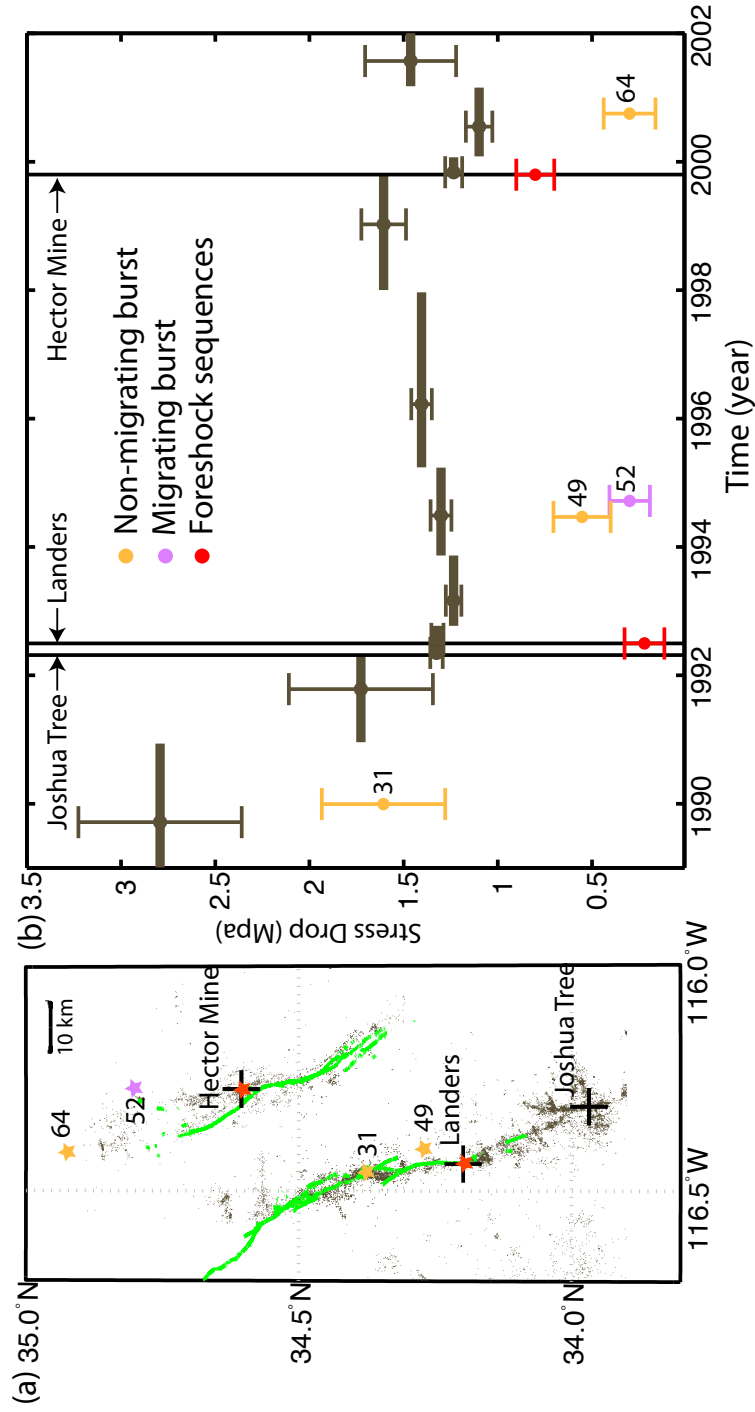seismicity in the region (small grey dots). Green lines are surface fault traces.
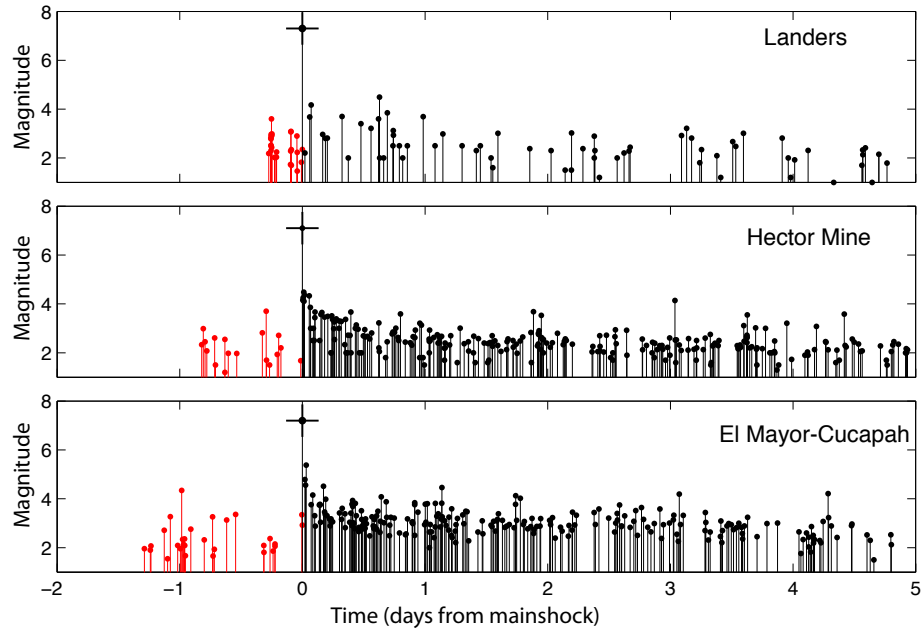
Figure 5.2: Magnitude versus time distributions for the three mainshocks. Foreshocks within 3.3 km (6.6 km for El Mayor-Cucapah) and 2 days from mainshocks are shown in red; aftershocks within the same region and 5 days from mainshocks are shown in black.
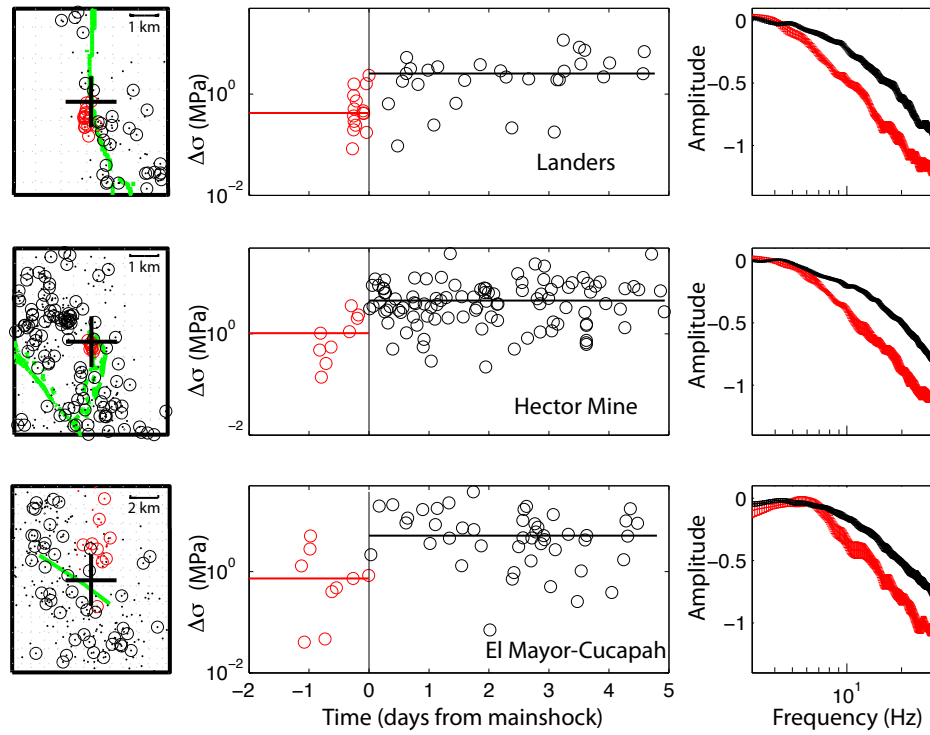
Figure 5.3: Foreshock vs. aftershock comparison. Left column: map view of seismicity, mainshock (shown in black "+") and fault trace (green lines) within the mainshock source region. Middle column: temporal variation of estimated earthquake stress drops (open circles), median values (horizontal lines). Vertical black lines are mainshock occurrence times. Right column: averaged source spectra for foreshocks and aftershocks. In all figures, foreshocks are shown in red, and aftershocks are shown in black.

Figure 5.4: Longer-term stress-drop variations in the Landers and Hector Mine source region. (a) Map view of seismicity (grey dots), surface rupture trace (green lines) and mainshock hypocenters (black "+"). Foreshock sequences and small seismicity "bursts" (from Vidale and Shearer 2006) are shown in stars with matching colors in (b). (b) Long-term median stress-drop variations over different time periods from 1989 to 2002 within the Landers and Hector Mine source regions. Median stress drops within small clusters are shown in closed circles. Two-standard-error bars are also plotted.

Supplemental materials

Methods

1. Location: The initial locations are obtained from a relocated catalog based on a 3D seismic velocity model and waveform cross-correlation (*Hauksson et al.*, 2012). Most of the foreshocks are within similar event clusters, but the mainshocks lack waveform similarity and are located using phase picks alone. In the catalog, the Landers and Hector Mine mainshocks are much deeper than their foreshocks, which may due to different location methods. To obtain more reliable mainshock locations relative to foreshocks, we apply a STA/LTA auto-picker method (*Chen et al.*, 2011) to obtain differential arrival times between the mainshocks and foreshocks, which are then incorporated with differential times among the foreshocks to obtain relative locations for each foreshock-mainshock sequence (*Lin et al.*, 2007). After relocation, the Landers and Hector Mine mainshock hypocenters are located within their foreshock clouds. For the El Mayor-Cucapah sequence, due to the lack of station coverage south of the US-Mexico bounder and reduced waveform similarity, only the Hauksson catalog locations are used.

2. Source spectra and stress drop: We obtain available waveforms from the Southern California Seismic Network (SCSN), as archived at the Southern California Earthquake Center (SCEC) data center. Individual source spectra and stress drop estimates are obtained with an iterative de-convolution and empirical Greens function method (*Shearer et al.*, 2006). To directly compare the source spectra before and after the mainshock, we need to account for differences in corner frequency due to moment variations, which is done by shifting the source spectra along the f^{-3} curve (*Prieto et al.*, 2004). We then normalize the spectra to their low-frequency amplitude, and calculate an average for foreshocks and aftershocks respectively, estimating a standard error using a bootstrap approach.
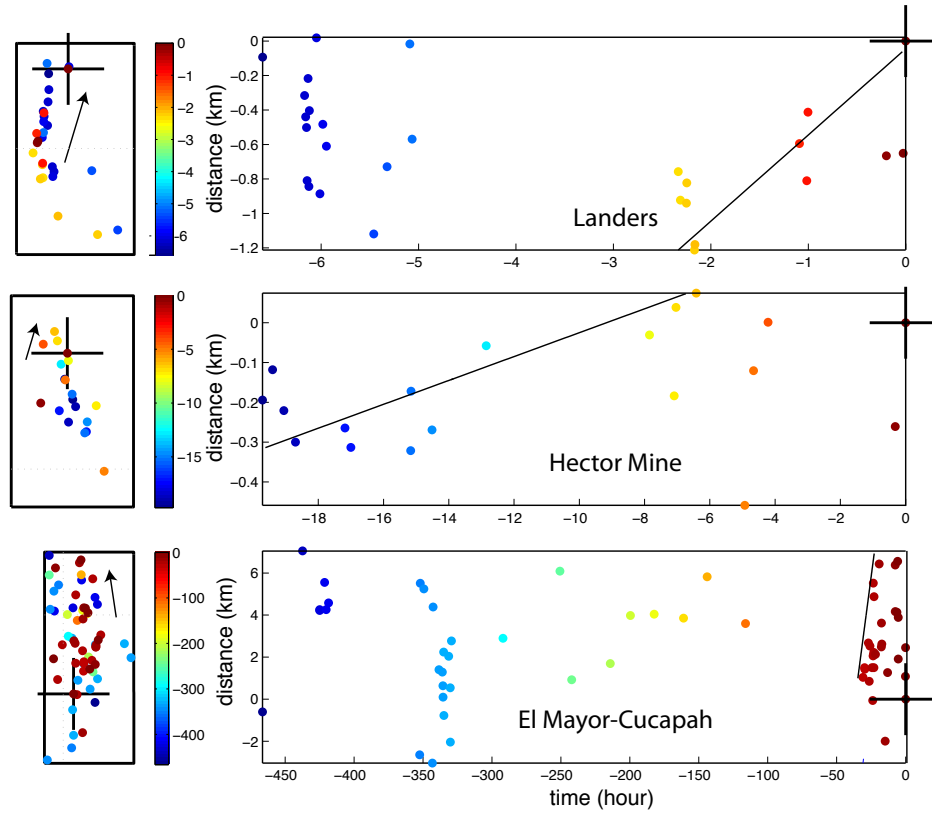
Figure 5.5: Detailed spatial-temporal distribution of foreshock sequences. Left column is the map view of seismicity, with events colored by occurrence times. Right column is the distance along best-fitting seismicity onset migration direction (black arrows) versus time. Black lines are the best-fitting migration velocity. Black + are mainshock locations.
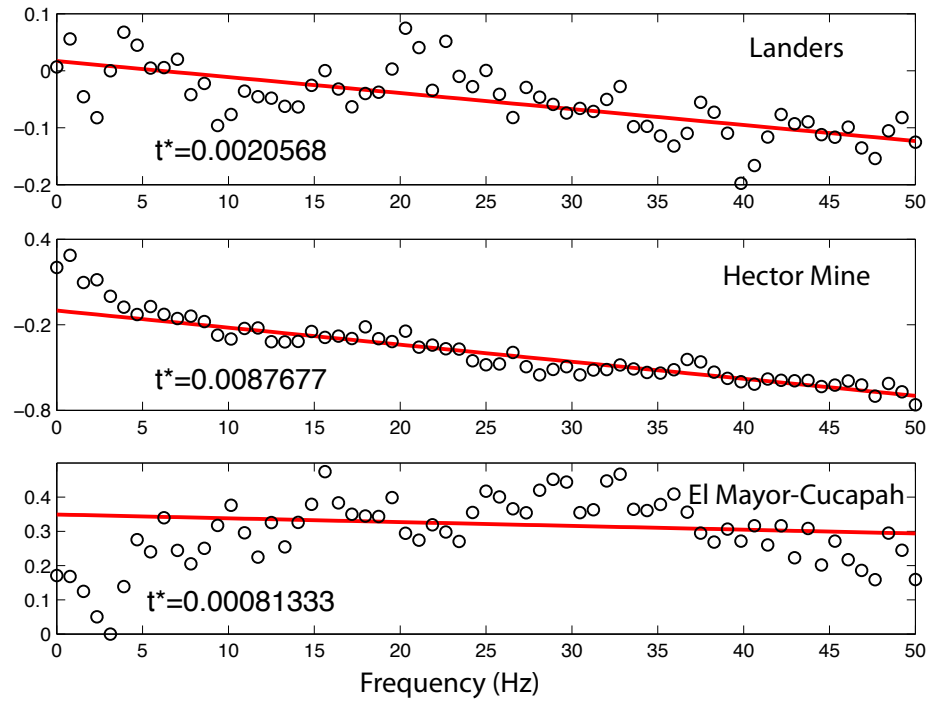
Figure 5.6: Spectral ratio of the empirical Greens function (EGF) before and after the mainshock. t* changes are relative to the pre-mainshock level. Red lines show the least-squares fit line (from 3 to 50 Hz); t* is then computed from the line slope.
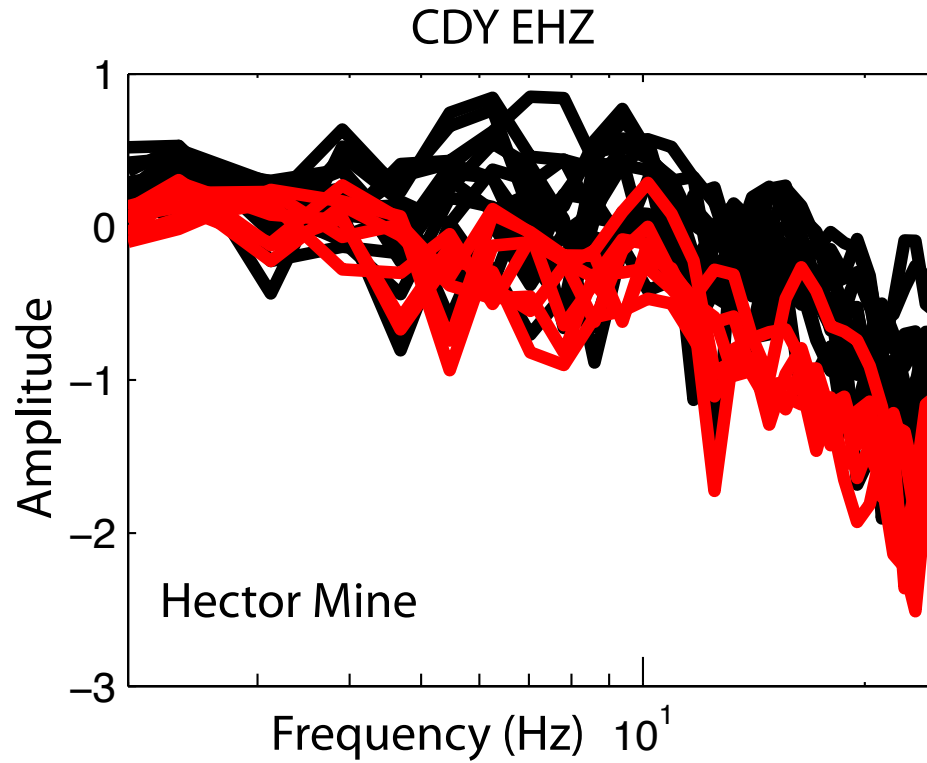
Figure 5.7: Example of the original displacement spectra at station CDY on channel EHZ for the Hector Mine sequence. Foreshock spectra are shown in red, and aftershock spectra are shown in black. Spectra are shifted relative to the low frequency amplitude. The events are from the spatial-temporal window shown in Figure 3.

Chapter 6

Analysis of foreshock sequences in California-implications of foreshock triggering process

We examine precursory occurrence patterns for $M \geq 5$ earthquakes in southern California from 1981 to 2011 and in northern California from 1984 to 2009. 53% of the 64 mainshocks are preceded by at least one foreshock within 2 days and 5 km. Foreshock occurrence appears correlated with mainshock faulting type and depth. Foreshock area is correlated with the magnitude of the largest foreshock but only weakly correlated with mainshock magnitude. We also examine small seismicity clusters that have at least 10 events within 2 days and 5 km, resembling swarm-like foreshock sequences. Only a small fraction of the small clusters lead to a larger cluster. About 70% of the large clusters don't start with their largest event, and the spatial distribution pattern is similar to $M \geq 5$ mainshocks, with lower occurrence rates in the Transverse Range and central California and higher occurrence rates in the eastern California Shear Zone and the Hayward fault zone. These results suggest that foreshock occurrence is largely controlled by the regional tectonic stress field and fault zone properties. Foreshocks properties do not seem useful in predicting the magnitude of the eventual "mainshock."

6.1 Introduction

Mogi (1963) distinguished three main types of earthquake sequences: (1) mainshocks with both foreshocks and aftershocks, (2) mainshocks and aftershocks, and (3) earthquake swarms. There have been studies on the triggering process involved in each category. Aftershocks are usually triggered by dynamic or static stress changes imposed by the mainshocks, and earthquake swarms are usually believed triggered by crustal transient processes (although some degree of earthquake-to-earthquake triggering is also involved). There have been debates on the triggering role of foreshocks in foreshock-mainshock-aftershock sequences. One model predicts that both foreshocks and aftershocks can be explained with a common triggering model. Statistical tests in California have found no evidence to reject this hypothesis (*Felzer et al.*, 2004). However, for some individual events there is evidence to support models in which foreshocks are triggered by an aseismic transient that occurs within the mainshock rupture zone. It remains unclear whether this aseismic transient is part of a mainshock nucleation phase, because the proposed acceleration phase is difficult to observe in foreshock sequences, except for the Izmit earthquake (*Bouchon et al.*, 2012a). Studies have found foreshock occurrence is dependent on the regional stress field, e.g., normal faulting versus reverse faulting (*Abercrombie and Mori*, 1996), or intraplate earthquakes versus interplate earthquakes (*Bouchon et al.*, 2012b). These observations indicate that the occurrence of foreshocks is not purely random, but may be influenced by the regional stress field. *Dodge et al.* (1996) reported scaling of foreshock area with mainshock magnitude, which is similar to the scaling relationship of the proposed nucleation phase of *Ellsworth and Beroza* (1995). *Felzer et al.* (2004) found a much stronger correlation between foreshock area and the magnitude of the largest foreshock, instead of the magnitude of the mainshock.

Recently developed high-resolution catalogs provide opportunities to review previously identified foreshock features, and further probe the relationships between precursory seismicity, different earthquake cluster types, and mainshock properties, which may be helpful in developing regional hazard or forecasting models. In this study, we search for mainshocks that are relatively isolated from back-

ground seismicity and aftershock sequences from previous large events. We then examine their occurrence compared to faulting type, mainshock location, and magnitude properties, in order to understand if there is any pattern in the apparent randomness of foreshock occurrence and if there is any relationship between foreshock properties and mainshock parameters.

6.2 Foreshock occurrence pattern for $M \geq 5$ earthquakes

We search for mainshocks with $M \geq 5$ using two waveform relocated catalogs in California: (1) the *Hauksson et al.* (2012) catalog for southern California from 1981 to 2011, excluding events north of 35.5° and south of 32.0°; (2) the *Waldhauser and Schaff* (2008) catalog for northern California from 1984 to 2009, excluding events south of 35.5° and north of 39.5°. We use several criteria to define a mainshock, the event is not: (1) a smaller event within 10 days and 50 km after a $M \geq 5$ event; (2) a smaller event within 120 days after $M \geq 6$ events; (3) a smaller event immediately before a $M \geq 5$ event within 2 days and 5 km. These requirements are not an attempt to decluster the catalog, but rather to ensure the mainshocks that we analyze are largely independent from other large events (e.g., not within direct aftershock sequences or when the catalog is temporarily influenced by the occurrence of a large event). Tests without applying such criteria resulted in several large "mainshocks" that are clear aftershocks of previous larger events, in which their "foreshocks" cannot be distinguished from aftershocks of the earlier event. In total, 70 mainshocks in the two catalogs meet our criteria. Visual examination found five of these events are part of long-duration continuous sequences, and are excluded from the final list. The M6.6 event on the Superstition Hills fault in 1987 occurred 12 hours following the M6.2 Elmore Ranch earthquake (noted with "*" in Table 6.1). The M6.6 earthquake is excluded from the final list, because its precursory seismicity is dominated by seismicity following the first event. Because of its large extent, the foreshock zone for the 2010 El Mayor Cucapah earthquake is expanded to 6 km and 10 days.

For the remaining 64 mainshocks, we search for immediate foreshocks that occur within 2 days and 5 km of the mainshock. 30 mainshocks have no foreshocks, and 34 have at least one foreshock. Among the 34 mainshocks with foreshocks, 3 are earthquake swarms in the Salton Trough and Nevada, and 3 are earthquake doublets (two events of similar magnitude occurring almost instantaneously, listed with "**" in Table 6.1). 14 mainshocks have fewer than 2 foreshocks, and 14 have more than 3 foreshocks (for which we are able to estimate the horizontal area that includes all the foreshocks). Some special cases are included (noted with "*" in Table 6.1): (1) the 1986 Mt. Lewis sequence has a swarm with 14 events that occurred 7 days before the mainshock, which are included in the foreshocks; (2) for the 1986 Chalfant earthquake, a M5.9 event occurred 1 day before the M6.4 event, and the former is assumed to be the mainshock, with 40 foreshocks. Thus, from the mainshocks examined here, 53% have at least one foreshock. A list of foreshocks is in Table 6.1 and a map view of the mainshock locations is shown in Figure 6.2.

6.2.1 Relationship between foreshock properties and mainshock parameters

Next, we examine if there is any relationship between foreshock statistics and mainshock source parameters. We first compare foreshock occurrence with focal mechanism. We obtain focal mechanism solutions from: (1) the YSH catalog for southern California, recalculated using the HASH method (*Hardebeck and Shearer*, 2003) with data from Southern California earthquake center (*Yang et al.*, 2012); (2) the northern California moment tensor catalog [*Northern California Earthquake Catalog and Phase Data*]; and (3) Global CMT solutions when available. We compute faulting type based on rake angle (-1 is normal fault, 0 is strike-slip fault, 1 is reverse fault):

$$f = \begin{cases} \lambda/90 & \text{if } |\lambda| \leq 90; \\ (180 - |\lambda|) * (\lambda/|\lambda|) & \text{if } |\lambda| > 90. \end{cases} \quad (6.1)$$

For 8 mainshocks, there is a high degree of mismatch ($> 40°$ between fault plane orientations and $df = |f_{regional} - f_{cmt}| > 0.4$) between the global CMT solution and the regional network solution (see Table 6.1 and Figure 6.2). The mismatch may be due to reduced azimuthal station coverage approaching the limits of the regional network (e.g., events off-shore and events in Mexico), or complexity in the earthquake rupture process (e.g., the rupture initiated with a sub-event with a different focal mechanism). We examine foreshock occurrence in 10 faulting type bins from -1 to 1. From Figure 6.3, there is a higher foreshock occurrence rate for mainshocks with dilational components ($f < 0$). Reverse faulting mainshocks tend to have lower foreshock occurrence rates. Although some mainshocks have a larger degree of mismatch with CMT solutions, these events do not affect the overall trend of decreasing foreshock occurrence for reverse faulting events. There is only one data point for pure normal faulting, and it doesn't have a foreshock. However, with the regional focal mechanism catalog, all the normal faulting earthquakes are preceded by at least one foreshock. The result is most reliable for faulting types from -0.4 to 0.5, where an increase in the compressional component decreases foreshock occurrence for strike-slip faults. We also compare foreshock occurrence with mainshock depth (updated with CMT depth when available, in accordance with focal mechanism solutions). In Figure 6.4, for shallower events (mostly < 8 km), the majority of mainshocks have foreshocks, and the occurrence rate decrease with depth. Regional catalogs confirm the prevalence of foreshock occurrence at shallow depth, however, the overall trend is much weaker compared with CMT depths.

We compare foreshock properties with mainshock magnitude, examining: (1) the radius of foreshock area for the 14 swarm-like foreshock sequences (calculated from the total volume that includes all the foreshocks in each sequence); (2) the number of foreshocks; (3) the magnitude of the largest foreshock; and (4) foreshock duration. For the three $M > 7$ mainshocks, we have shown that none of these properties are correlated with mainshock magnitude (*Chen and Shearer*, 2013). For other events, the foreshock radius is correlated with mainshock magnitude, with $r = 0.48$ (correlation coefficient) and $p = 0.12$ (random chance of

correlation is 12%). A much stronger correlation is found between foreshock area and the magnitude of the largest foreshocks ($r = 0.7, p = 0.01$). The number of foreshocks is not correlated with mainshock magnitude ($r = 0.3$ and $p = 0.5$), nor the magnitude of the largest foreshock ($r = 0.1, p = 0.8$). Foreshock duration is not related to either mainshock magnitude ($r = 0.15, p = 0.61$) or mainshock depth ($r = 0.05, p = 0.86$). The magnitude of the largest foreshock is not well correlated with mainshock magnitude, the mean magnitude difference is 2, and a large portion of Δm fall outside the $[0, 2]$ range (see Figure 6.9).

Overall, observations of foreshock dependence on faulting type and depth is consistent with the results in *Abercrombie and Mori* (1996), however, our result is more reliable for strike-slip faults and shallow depths, because we have examined more events and obtain consistent results with both regional and CMT catalogs. We compare our foreshock radius estimates with results in *Dodge et al.* (1996) (see Figure 6.5). In general, for the events in common, our radius is consistent with previous measurements, however, about half of the points are above the 1σ boundaries of nucleation radius estimated from the slow onset of mainshock waveforms (*Ellsworth and Beroza*, 1995). There is no clear correlation between foreshock duration and mainshock depth, which is inconsistent with previous observations (*Jones*, 1984; *Abercrombie and Mori*, 1996). There is no clear spatial separation between different types of mainshocks, however, some regions are dominated by certain type: within the Transverse Range region in Los Angeles county and central California, most mainshocks do not have foreshocks; in contrast, in the Hayward fault zone and Eastern California Shear Zone (ECSZ), the occurrence rate of foreshocks is relatively high.

6.2.2   Precursory seismicity

5 km roughly corresponds to the rupture area of a M5.8 earthquake, assuming a stress drop of 2 MPa (the average stress drop for southern California from *Shearer et al.* (2006), calculated from *Shearer* (2009), with $r = (\frac{7M_0}{16\Delta\sigma})^{1/3}$). According to *Shearer and Lin* (2009), the radius of the "Mogi-doughnut" (precursory quiescence) roughly agrees with the expected rupture radius for target mainshocks.

Due to the small number of M5 earthquakes in the catalog, such behavior is not reliably resolved for larger events. For the 64 M $\geq$ 5 mainshocks, we examine the averaged precursory seismicity for: (1) 28 mainshocks without foreshocks; (2) 28 mainshocks with foreshocks; and (3) 3 earthquake swarms. From Figure 6.7, within 1 day prior to mainshock, the low seismicity zone extends beyond the 5 km criteria, consistent with the empirical scaling of the "Mogi-Doughnut" behavior. Due to the limited number of available mainshocks, it is difficult to perform statistical analysis to test the reliability of the result. Foreshock activities are confined within the "Mogi" zone, and well separated from background seismicity. The three earthquake swarms are almost completely separated from background seismicity, most likely because these three events are located near the limits of the NoCal and SoCal catalogs (two events are near the southern end of southern California, and one event is near the north-eastern end of northern California).

6.3 Smaller clusters that resemble foreshock features

So far, our analysis has been limited to $M \geq 5$ target events, and any precursory seismicity within 5 km and 2 days. Other questions related to precursory activities include: (1) How are foreshocks different from random small clusters?, and (2) How often do the small clusters lead to larger clusters that might include a larger event? To address this, we remove the magnitude requirement, and search for small compact clusters that resemble the observed foreshock sequences. Specifically, we search for small clusters that have at least $N \geq 10$ events within 5 km and 2 days, and fewer than 5 events in the previous 7 days within 5 km. We apply the same criteria as before to temporarily remove immediate aftershock sequences from the catalog. This results in 1152 small clusters across California, mostly located within seismically dense regions (see Figure 6.10).

Next, we examine if these clusters lead to larger clusters. To define a larger cluster, we require: (1) $N_{cluster} \geq 50$ within 28 days and 5 km; (2) $N_{out} \leq 0.2 N_{cluster}$ within 28 days between 5 and 10 km for $M < 5$ earthquakes (for $M \geq 5$

events, the aftershock zone likely extends beyond 5 km radius, therefore, we only add this requirement for smaller events). Only 197 small clusters lead to larger clusters that meet our criteria. The criteria is based on a previous study (e.g., *Vidale and Shearer* (2006) and *Chen and Shearer* (2011)) and the observations of foreshock sequences. To characterize the cluster type, we compute four parameters as described in *Chen et al.* (2012): (1) the timing of the largest event in the cluster t_{max} normalized by the median duration of the cluster; (2) the skew (μ) of moment release history; (3) the distance separation of the first and second half of the cluster normalized by the radius of the cluster (d_s); and (4) $\Delta\sigma_{quasi} = \frac{7\sum_n^1 M_0^i}{16r^3}$, effective stress drop. Only 58 out of the 197 larger clusters started with the largest event in the sequence. From Figure 6.8, the CDF (cumulative density function) of the four parameters is consistent with the distribution in *Chen et al.* (2012), although the difference in μ is much smaller. Over half of the clusters have their largest earthquake in the later half of the sequence. For clusters with higher T_{max}, there is a higher probability of a greater degree of separation between the first half and second half of the sequence, indicating the possibility of spatial migration. Comparison of $\Delta\sigma_{quasi}$ indicates that clusters that don't start with their largest event tend to span a larger area with similar moment release.

For M $\geq$ 4 events, the magnitude difference between the largest foreshock and the mainshock (Δm) has an average value of about 1.4, and is almost uniformly distributed between 0 and 2, which is consistent with observations in *Zaliapin and Ben-Zion* (2012) for M $\geq$ 4 events. However, for M $\geq$ 5 events, this pattern is not clear, probably because of the small number of mainshocks due to the cluster selection criteria. For this more generalized cluster analysis, the area of the foreshocks is not correlated with mainshock magnitude. Instead, for M $\geq$ 4.5 events, there is a significant correlation between the area of the foreshocks and the magnitude of the largest foreshocks ($r = 0.61, p = 0.002$). For events between M $\leq$ 4.5 and M $\geq$ 2, there is almost no correlation between the area of the foreshocks and foreshock magnitude ($r = 0.001, p = 0.89$). For southern California, we observe a similar relationship between precursory occurrence and small mainshock faulting type, however, the correlation is not so clear for northern California. For smaller

events, the focal mechanism is likely poorly determined compared with M $\geq$ 5 events, and the reduced correlation may be due to uncertainties in the fault plane solutions (as shown in Table 6.1, there is sometimes a large mismatch for $M \geq 5$ events).

The overall spatial distribution is similar for $M \geq 5$ mainshocks (see Figure 6.2 and Figure 6.10). For example, the Transverse Range and central California are still dominated by mainshocks without precursory activities. The Hayward fault zone, the ECSZ, the Salton Trough and the Long Valley region are dominated by mainshocks with precursory activities. Considering the geological features of these regions, this suggests that precursory activities tend to occur within extensional step overs, high heat flow regions, and complex fault zones, while lack of precursory activity is expected at thrust fault zones and relatively simple planar fault zones.

6.4 Discussion

Our analysis method is similar to the study of earthquake "bursts," which considers the relative independence of the clusters from other mainshocks (*Vidale and Shearer*, 2006). This approach may miss some events due to the selection criteria, however, the events selected should represent stress variations in the crust that are less likely influenced by stress changes from larger events. The most reliable patterns of foreshock occurrence that we obtained in this study, which are also consistent with previous observations, is the dependence on faulting type: mainshocks in a transtension setting tend to have more foreshocks compared with mainshocks in a transpression regime; and the dependence on mainshock depth: shallow mainshocks tend to have more foreshocks. There is no correlation between faulting type and mainshock depth, so foreshock occurrence is independently correlated with the two factors. The correlation with focal mechanism is similar to that seen for crustal "bursts" in southern California: normal faulting events tend to lack a clear mainshock and exhibit spatial migration, while reverse faulting events usually start with their largest event and span the entire rupture area in a short time period (*Chen et al.*, 2012).

Different studies have proposed various factors in controlling the generation of different seismicity clustering types. Some commonly accepted factors are fault zone complexity (i.e., small-scale heterogeneity) and fluid flow. Seismology evidence shows that earthquakes are promoted by fluid over-pressure status, which may result from sealing by low-permeable materials surrounding the fault zone (*Hardebeck and Hauksson*, 1999). The creation of dilatancy due to fault slip would increase the porosity and reduce pore pressure, and thus may retard the rupture process. Laboratory results show that the dilatancy strongly depends on the critical slip distance (D_c), which scales with the characteristic length of small-scale heterogeneity. Thus within highly fractured zones, a short D_c is expected, and swarm-like sequences are more likely to be observed (*Yamashita*, 1999). From Figure 6.10, fewer foreshocks are observed for the Garlock and Parkfield faults, where the faults are relatively smooth; whereas more foreshocks are observed within the ECSZ and the Hayward fault zone, where there are several dilational step-overs and fault intersections. Sibson [1993] proposed that the loading style during the earthquake cycle depends on the regional stress field. For pure normal faults, a "loading-weakening" mechanism, where the shear strength reduces with stress loading, is expected; while for reverse faults, a "loading-strengthening" mechanism is expected. For strike-slip faults, depending on the actual stress values, both mechanisms are possible, in which the style changes progressively from transtension to transpression status. If the mean stress decreases during shear loading, it is more likely for fluid to flow into the fault zone, which may facilitate the occurrence of small events. *Abercrombie and Mori* (1996) noted that increased normal stress is commonly expected for reverse faulting and deeper events, which may prohibit occurrence of small events.

Among all the foreshock parameters, only foreshock area is weakly correlated with mainshock magnitude (see Figure 6.5), however, a much stronger correlation is between area and the magnitude of the largest foreshock ($p = 0.01$). Such correlation is only valid for events with M $\geq$ 4.5. This is consistent with results in *Felzer et al.* (2004), in which they argue that this agrees with a single-mode triggering process for foreshocks. It is expected that the area of a cluster

scales up with the magnitude of the largest event in the cluster, because larger events have a larger rupture area. However, this does not necessarily imply an event-to-event triggering process for foreshock sequences, since the area of swarm sequences also scales with the magnitude of the largest event. For large earthquake swarms (e.g., the 1981, 2005 and 2012 Salton Trough swarms), spatial migration of seismicity is only visible prior to the largest event, after which aftershocks dominate the sequence (*Chen and Shearer*, 2011; *Haukkson et al.*, 2013). If the same triggering mechanism is applied to all earthquakes, then we may expect a similar relationship for smaller events, which is not observed with our dataset. *Shearer* (2012) find that for M2-3 events in southern California, earthquake-to-earthquake triggering could not explain the observed pre- to post-mainshock ratio, implying a different clustering process exists for smaller events.

Small, compact clusters are frequent in California (1152 in total), however, only about 17% of them lead to a larger cluster with more than 50 events, whereas 30% start with the largest event in the cluster. This percentile maybe biased by the high swarm occurrence rate in the Long valley region, which was excluded in some previous studies (*Abercrombie and Mori*, 1996; *Felzer et al.*, 2004)). In *Chen and Shearer* (2013), low stress drops compared with background seismicity is observed for swarm-like foreshock sequences in the ECSZ. If there is a distinction in spectral components between random small clusters and small clusters that lead to larger clusters, then their occurrence may be useful for short-term forecasting.

Acknowledgments

Chapter 6, in full, is being prepared for publication: Analysis of foreshock

sequences in California–implications of foreshock triggering process. I am the primary investigator and author of the paper. In this Chapter, we study the general behavior of foreshock occurrence patterns in California, and try to understand the relationship between precursors and fault zone properties.

References

Abercrombie, R. E., and J. Mori (1996), Occurrence patterns of foreshocks to large earthquakes in the western united states, *Nature*, *381*(6580), 303–307.

Beroza, G. C., and W. L. Ellsworth (1996), Properties of the seismic nucleation phase, *Tectonophysics*, *261*(1-3), 209–227.

Bouchon, M., H. Karabulut, M. Aktar, S. Ozalaybey, J. Schmittbuhl, and M. P. Bouin (2012a), Extended nucleation of the 1999 m-w 7.6 izmit earthquake, *Science*, *331*(6019), 877–880.

Bouchon, M., V. Durand, D. Marsan, H. Karabulut, and J. Schmittbuhl (2012b), The long nucleation of most large interplate earthquakes, *Nature Geosci*.

Chen, X., and P. M. Shearer (2011), Comprehensive analysis of earthquake source spectra and swarms in the salton trough, california, *J. Geophys. Res.*, *116*(B09309).

Chen, X., and P. M. Shearer (2013), California foreshock sequences suggest underlying aseismic process, *Geophysical Research Letters, in review*.

Chen, X., P. M. Shearer, and R. Abercrombie (2012), Spatial migration of earthquakes within seismic clusters in southern california: Evidence for fluid diffusion, *J. Geophys. Res.*, *117*(B04301).

Dodge, D. A., G. C. Beroza, and W. L. Ellsworth (1996), Detailed observations of california foreshock sequences: Implications for the earthquake initiation process, *Journal of Geophysical Research-Solid Earth*, *101*(B10), 22,371–22,392.

Ellsworth, W. L., and G. C. Beroza (1995), Seismic evidence for an earthquake nucleation phase, *Science*, *268*(5212), 851–855.

Felzer, K. R., R. E. Abercrombie, and G. Ekstrom (2004), A common origin for aftershocks, foreshocks, and multiplets, *Bulletin of the Seismological Society of America*, *94*(1), 88–98.

Hardebeck, J. L., and E. Hauksson (1999), Role of fluids in faulting inferred from stress field signatures, *Science*, *285*, doi:10.1126/science.285.5425.236.

Hardebeck, J. L., and P. M. Shearer (2003), Using s/p amplitude ratios to constrain the focal mechanisms of small earthquakes, *Bulletin of the Seismological Society of America*, *93*(6), 2434–2444.

Haukkson, E., J. Stock, R. Bilham, M. Boese, X. Chen, E. J. Fielding, J. Galetzka, K. W. Hudnut, K. Hutton, L. M. Jones, H. Kanamori, P. M. Shearer, J. Steidl, J. Treiman, S. Wei, and W. Yang (2013), Report on the august 2012 brawley earthquake swarm in imperial valley, southern california, *Seismological Research Letters*.

Hauksson, E., W. Yang, and P. M. Shearer (2012), Waveform relocated earthquake catalog for southern california (1981 to june 2011), *Bulletin of the Seismological Society of America*, *102*(5), 2239–2244.

Jones, L. M. (1984), Foreshocks (1966-1980) in the san-andreas system, california, *Bulletin of the Seismological Society of America*, *74*(4), 1361–1380.

Mogi, K. (1963), Some discussions on aftershocks, foreshocks and earthquake swarms - the fracture of a semi-infinite body casued by an inner stress origin and its relation to the earthquake phenomena, *Bulletin of the Earthquake Research Institute*, *41*, 615–658.

Shearer, P. M. (2009), *Introduction to Seismology*, second edition ed., Cambridge University Press.

Shearer, P. M. (2012), Self-similar earthquake triggering, bth's law, and foreshock/aftershock magnitudes: Simulations, theory, and results for southern california, *J. Geophys. Res.*, *117*(B6), B06,310.

Shearer, P. M., and G. Q. Lin (2009), Evidence for mogi doughnut behavior in seismicity preceding small earthquakes in southern california, *Journal of Geophysical Research-Solid Earth*, *114*, 9.

Shearer, P. M., G. A. Prieto, and E. Hauksson (2006), Comprehensive analysis of earthquake source spectra in southern california, *Journal of Geophysical Research-Solid Earth*, *111*(B6).

Vidale, J. E., and P. M. Shearer (2006), A survey of 71 earthquake bursts across southern california: Exploring the role of pore fluid pressure fluctuations and aseismic slip as drivers, *Journal of Geophysical Research-Solid Earth*, *111*(B5).

Waldhauser, F., and D. Schaff (2008), Large-scale relocation of two decades of northern california seismicity using cross-correlation and double-difference methods, *J. Geophys. Res.*, *113*(B08311), doi:10.1029/2007JB005479.

Yamashita, T. (1999), Pore creation due to fault slip in a fluid-permeated fault zone and its effect on seismicity: Generation mechanism of earthquake swarm, *Pure and Applied Geophysics*, *155*(2-4), 625–647.

Yang, W., E. Hauksson, and P. M. Shearer (2012), Computing a large refined catalog of focal mechanisms for southern california (1981-2010): Temporal stability of the style of faulting, *Bulletin of the Seismological Society of America*, *102*(3), 1179–1194.

Zaliapin, I., and Y. Ben-Zion (2012), Earthquake clusters in southern california, i: Identification, *J. Geophys. Res., in review.*

Table 6.1: List of foreshocks with M>5 included in this study. CMT solutions are in parentheses. Red color indicates events with a high degree of disagreement between CMT solutions and regional moment tensor catalog. Events with "*" are special cases and events with "**" indicates earthquake doublets (see text for details).

| Time	Location	Depth	Mag	N_{fore}	Focal mechanism	Fault type	Plane$_{diff}$
1981/09/04 15:50:49.62	33.650 -119.121	10.92(5.00)	5.45	0	134. 77. 169.(311. 90. 180.)	0.12(0.00)	12.94
1986/07/08 09:20:44.06	34.001 -116.606	13.25(10.00)	5.65	0	298. 38. -177.(294. 37. 156.)	-0.03(0.27)	3.33
1986/07/13 13:47: 9.12	32.988 -117.863	21.36(5.00)	5.45	0	359. 72. -167.(126. 37. 106.)	-0.14(0.82)	43.86
1987/10/01 14:42:19.66	34.067 -118.092	13.50(11.00)	5.90	0	262. 23. 83.(270. 31. 98.)	0.92(0.91)	10.71
1988/06/10 23:06:42.52	34.931 -118.742	9.46(N/A)	5.37	0	162. 83. 176.(N/A)	0.04(N/A)	N/A
1988/12/03 11:38:26.26	34.142 -118.138	12.74(N/A)	5.02	0	157. 86. 169.(N/A)	0.12(N/A)	N/A
1988/12/16 05:53: 4.48	33.983 -116.688	11.47(N/A)	5.03	0	292. 41. 148.(N/A)	0.36(N/A)	N/A
1991/06/28 14:43:54.47	34.266 -117.989	9.64(11.00)	5.80	0	56. 25. 74.(93. 43. 130.)	0.82(0.56)	35.15
1991/12/03 17:54:36.20	31.718 -115.821	18.31(N/A)	5.32	0	N/A (N/A)	0.00(N/A)	N/A
1993/05/28 04:47:40.26	35.132 -119.116	23.90(N/A)	5.19	0	114. 71. 170.(N/A)	0.11(N/A)	N/A
1994/01/17 12:30:54.96	34.206 -118.549	21.07(18.00)	6.70	0	113. 36. 106.(278. 42. 65.)	0.82(0.72)	13.00
2001/12/08 23:36:10.03	32.035 -114.963	17.23(10.00)	5.70	0	N/A (141. 59. -149.)	N/A(-0.34)	N/A
2002/02/22 19:32:41.50	32.309 -115.315	19.91(7.00)	5.70	0	N/A (190. 66. -4.)	N/A(-0.04)	N/A
2004/09/29 22:54:54.20	35.385 -118.629	7.30(3.50)	5.03	0	105. 82. 173.(293. 71. -169.)	0.08(-0.12)	11.13
2005/06/12 15:41:46.19	33.533 -116.570	15.48(14.20)	5.20	0	304. 58. 172.(305. 53. -179.)	0.09(-0.01)	5.03
2006/05/24 04:20:26.05	32.303 -115.223	14.38(N/A)	5.37	0	0. 0. 0.(N/A)	N/A(N/A)	N/A
2008/02/09 07:12: 6.84	32.410 -115.312	18.65(2.90)	5.10	0	147. 66. -175.(226. 79. 3.)	-0.06(0.03)	24.25
2008/07/29 18:42:15.28	33.946 -117.767	14.89(14.70)	5.39	0	296. 66. 146.(44. 55. 29.)	0.38(0.32)	34.85
2008/12/06 04:18:42.29	34.812 -116.423	9.33(7.30)	5.06	0	172. 79. -157(253. 83. 6.)	-0.26(0.07)	12.02
1984/01/23 05:40:20.03	36.390 -121.886	7.73(N/A)	5.10	0	65. 85. 10.(N/A)	0.11(N/A)	N/A
1984/04/24 21:15:18.75	37.310 -121.682	7.97(8.00)	6.20	0	240. 80. 10.(333. 76. 179.)	0.11(0.01)	16.66
1988/02/20 08:39:57.49	36.798 -121.306	8.22(N/A)	5.10	0	45. 60. 10.(N/A)	0.11(N/A)	N/A
1988/06/27 18:43:22.65	37.129 -121.894	11.54(N/A)	5.30	0	35. 85. 30.(N/A)	0.33(N/A)	N/A
1988/09/19 02:56:31.33	38.458 -118.344	6.72(N/A)	5.30	0	40. 50. -10.(N/A)	-0.11(N/A)	N/A
1989/10/18 00:04:15.39	37.043 -121.877	16.41(19.00)	7.00	0	130. 75. 130.(235. 41. 29.)	0.56(0.32)	46.77
1991/09/17 21:10:29.35	35.815 -121.322	8.01(N/A)	5.20	0	80. 55. 50.(N/A)	0.56(N/A)	N/A
1993/05/17 23:20:49.15	37.171 -117.782	2.39(7.00)	6.40	0	250. 65. 20.(210. 30. -93.)	0.22(-0.97)	42.81
1996/11/27 20:17:23.54	36.090 -117.628	6.56(1.00)	5.10	0	N/A (244. 71. -3.)	N/A(-0.03)	N/A
2003/12/22 19:15:56.21	35.701 -121.099	8.05(7.60)	6.50	0	105. 35. 80.(296. 32. 88.)	0.89(0.98)	9.73
2004/09/28 17:15:24.31	35.818 -120.366	8.20(8.80)	6.00	0	145. 85. -170.(321. 72. -178.)	-0.11(-0.02)	13.02
1987/02/07 03:45:14.97	32.388 -115.317	24.44(5.00)	5.38	2	235. 87. 98.(202. 70. 2.)	0.91(0.02)	17.55
1997/04/26 10:37:30.38	34.376 -118.673	13.67(N/A)	5.07	1	358. 52. -141.(N/A)	-0.43(N/A)	N/A
2001/10/31 07:56:16.22	33.504 -116.503	16.83(N/A)	5.02	1	301. 35. 172.(N/A)	0.09(N/A)	N/A
2009/09/19 22:55:17.64	32.344 -115.256	19.08(3.00)	5.08	1	67. 38. 75.(125. 71. -172.)	0.83(-0.09)	44.09
2009/12/30 18:48:56.69	32.417 -115.149	23.81(9.00)	5.80	2	205. 40. -92.(328. 82. -178.)	-0.98(-0.02)	45.98
1984/11/23 18:08:25.25	37.455 -118.606	11.11(N/A)	6.10	1	65. 85. 30.(N/A)	0.33(N/A)	N/A
1986/01/26 19:20:51.18	36.803 -121.284	7.10(7.00)	5.50	1	260. 80. -10.(166. 90. 180.)	-0.11(0.00)	9.97
1987/02/14 07:26:50.39	36.171 -120.339	13.55(13.00)	5.30	1	150. 50. 90.(300. 46. 38.)	1.00(0.42)	20.24
1988/06/13 01:45:36.68	37.395 -121.739	8.87(9.00)	5.30	1	60. 90. -10.(325. 76. -175.)	-0.11(-0.06)	13.97
1989/08/08 08:13:27.51	37.153 -121.926	12.59(N/A)	5.30	2	45. 65. 30.(N/A)	0.33(N/A)	N/A
1990/10/24 06:15:20.01	38.053 -119.125	12.38(12.00)	5.80	1	70. 55. 10 (56. 59. -10.)	0.11(-0.11)	8.58
1996/01/07 14:32:52.82	35.772 -117.622	9.56(N/A)	5.10	2	160. 80. -170.(N/A)	-0.11(N/A)	N/A
2007/10/31 03:04:54.87	37.432 -121.777	7.49(10.00)	5.40	1	55. 85. 0.(324. 81. 176.)	0.00(0.04)	10.18
1994/09/12 12:23:42.94	38.793 -119.702	2.96(14.00)	5.90	1	40. 40. -40. (42. 74. -13.)	-0.44(-0.14)	34.01
1987/11/24 01:54:14.21	33.082 -115.779	10.07(5.00)	6.20	6*	280. 86. 171.(305. 90. 180.)	0.10(0.00)	3.95
1990/02/28 23:43:36.23	34.138 -117.708	7.28(10.00)	5.51	4	132. 89. 167.(307. 73. 169.)	0.14(0.12)	16.00
1992/04/23 04:50:22.73	33.968 -116.313	13.71(10.00)	6.10	6	344. 85. 171.(81. 87. -1.)	0.10(-0.01)	5.47
1992/06/28 11:57:33.85	34.202 -116.435	7.01(5.00)	7.30	27	173. 85. -177.(341. 70. -172.)	-0.03(-0.09)	15.14
1992/11/27 16:00:57.39	34.337 -116.892	0.00(N/A)	5.29	5	128. 88. 167.(N/A)	0.14(N/A)	N/A
1997/03/18 15:24:47.70	34.966 -116.822	4.02(N/A)	5.26	3	154. 75. -163.(N/A)	-0.19(N/A)	N/A
1999/10/16 09:46:43.95	34.595 -116.271	9.06(0.00)	7.10	18	5. 90. 159.(336. 80. 174.)	0.23(0.07)	9.95
2010/04/04 22:40:42.16	32.264 -115.295	16.47(6.00)	7.20	26	264. 49. 165.(223. 84. -2.)	0.17(-0.02)	36.64
1985/08/04 12:01:55.85	36.138 -120.153	10.35(5.00)	5.60	6	70. 20. 40.(138. 10. 105.)	0.44(0.83)	66.04
1986/03/31 11:55:39.93	37.479 -121.691	8.39(6.00)	5.70	15*	355. 80. -180.(353. 79. -170.)	0.00(-0.11)	1.06
1986/07/20 14:29:45.47	37.567 -118.437	6.16(8.00)	5.90	40*	205. 85. -10.(223. 54. -35.)	-0.11(-0.39)	31.28
1990/04/18 13:53:51.62	36.931 -121.652	4.61(N/A)	5.40	4	55. 80. 40.(N/A)	0.44(N/A)	N/A
1997/11/02 08:51:52.83	37.863 -118.190	1.65(5.00)	5.30	8	N/A (238. 63. 15.)	N/A(0.17)	N/A
1998/08/12 14:10:25.15	36.759 -121.452	7.75(8.80)	5.10	3	225. 75. -10.(48. 85. -1.)	-0.11(-0.01)	10.01
1981/04/26 12:09:28.26	33.088 -115.619	10.60(6.00)	5.75	349	158. 86. -151.(249. 45. -8.)	-0.32(-0.09)	45.03
2005/09/02 01:27:19.46	33.154 -115.633	5.77(9.80)	5.11	387	190. 62. -106.(335. 76. -167.)	-0.82(-0.14)	18.21
2008/04/26 06:40:10.76	39.522 -119.927	2.28(1.40)	5.10	214	N/A (328. 86. 180.)	N/A(0.00)	N/A
2001/07/17 12:07:26.24	36.005 -117.871	8.73(N/A)	5.20	41**	80. 90. 0.(N/A)	0.00(N/A)	N/A
2004/09/18 23:02:17.72	38.012 -118.691	3.26(5.00)	5.60	42**	65. 90. -10.(330. 76. -171.)	-0.11(-0.10)	13.97
2009/10/03 01:15:59.75	36.396 -117.858	0.29(2.50)	5.10	52**	N/A (214. 56. -36.)	N/A(-0.40)	N/A
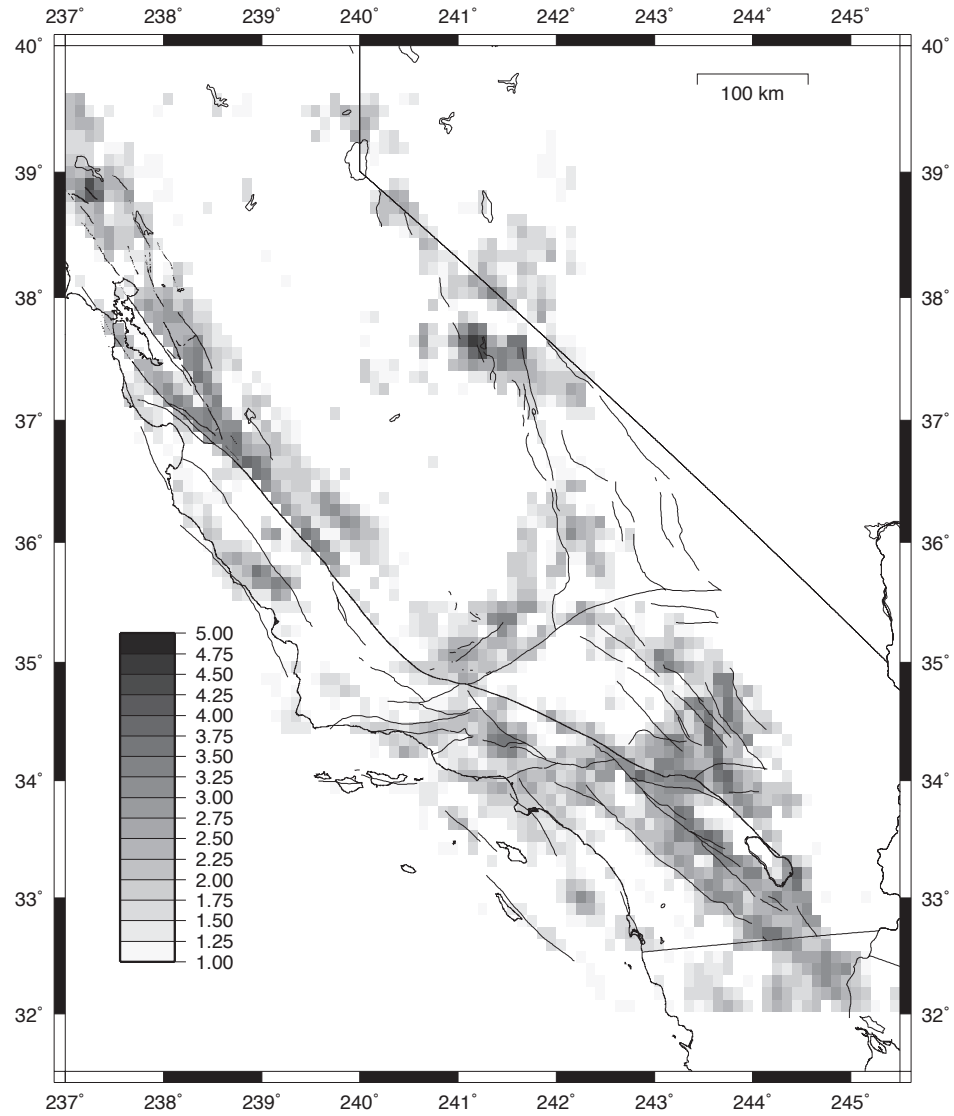
Figure 6.1: Map view of seismicity density in each $0.1^o \times 0.1^o$ grid, colored in log scale.
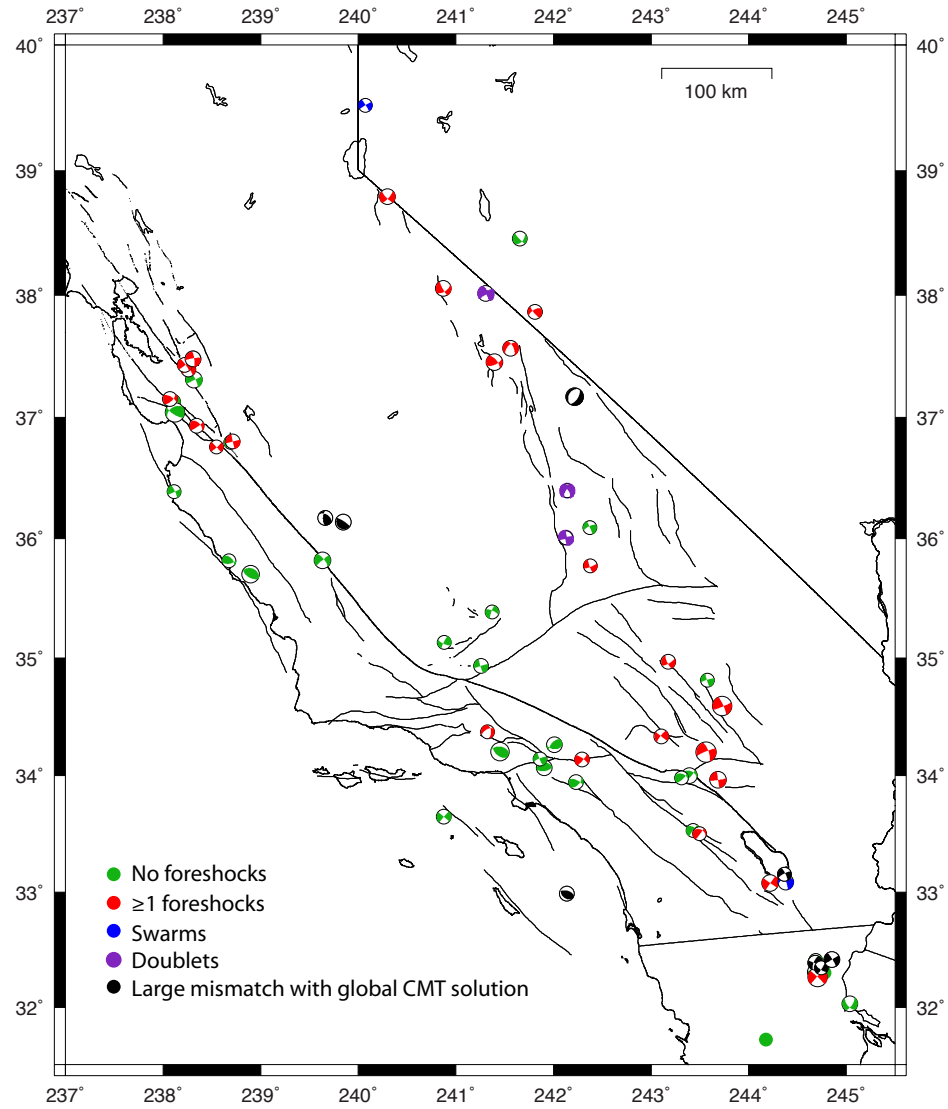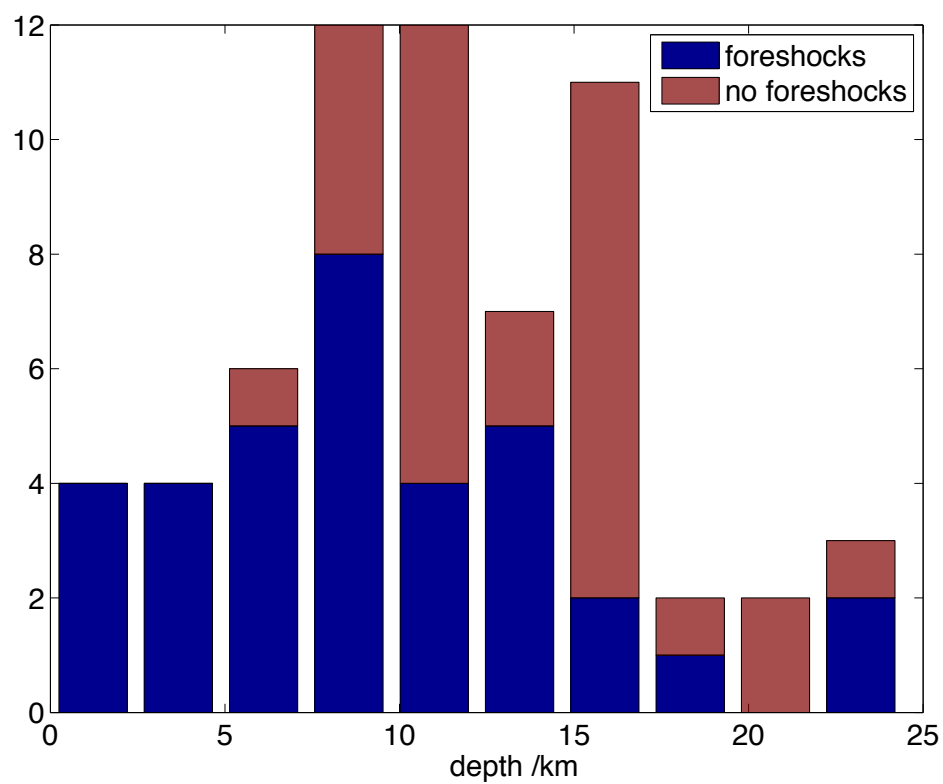
Figure 6.2: Map view of M>5 mainshocks. Events with large mismatch with CMT solutions correspond to events with red color in Table 6.1). Focal mechanisms are according to CMT solutions when available.
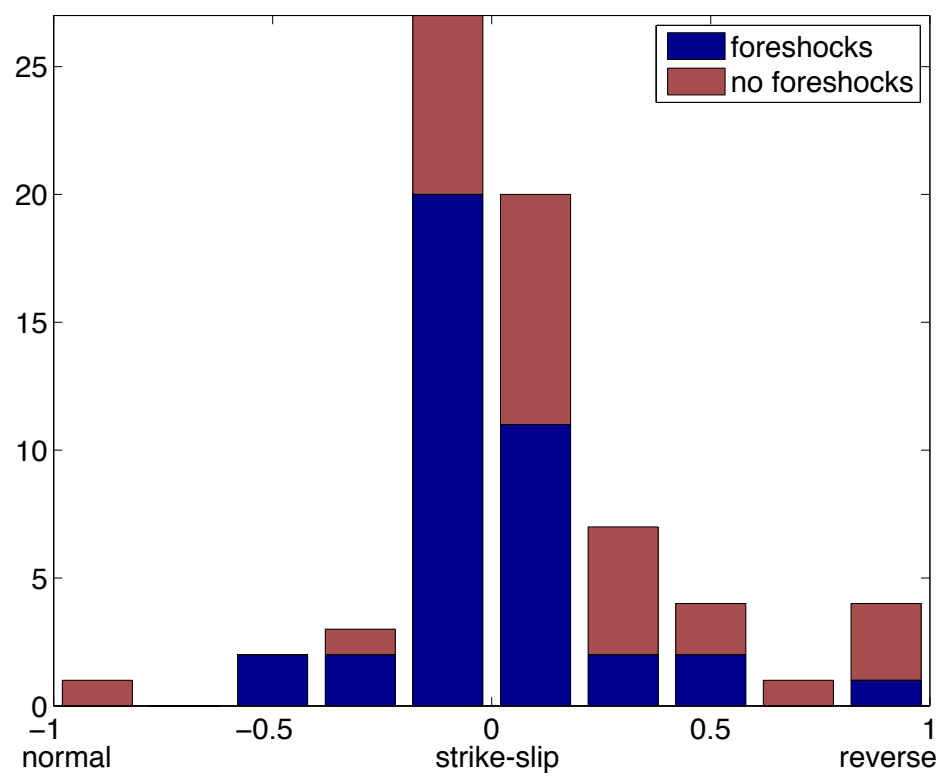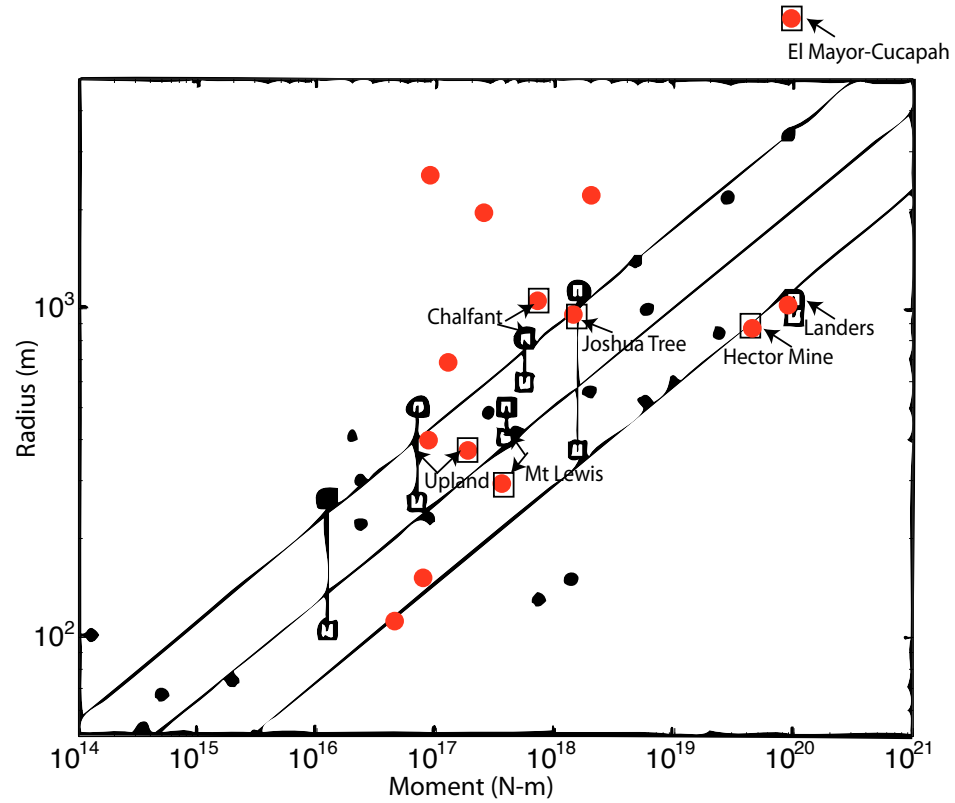
**Figure 6.3**: Histogram of mainshock faulting types.

**Figure 6.4**: Histogram of mainshock depth distribution.

Figure 6.5: Foreshock radius versus mainshock moment plotted on Figure 16 from *Dodge et al.* (1996). Red dots are 14 mainshocks in this study, boxes indicate named events in the catalog. Black dots are source radius estimated in *Beroza and Ellsworth* (1996), straight lines are best-linear fit and 1σ boundaries.
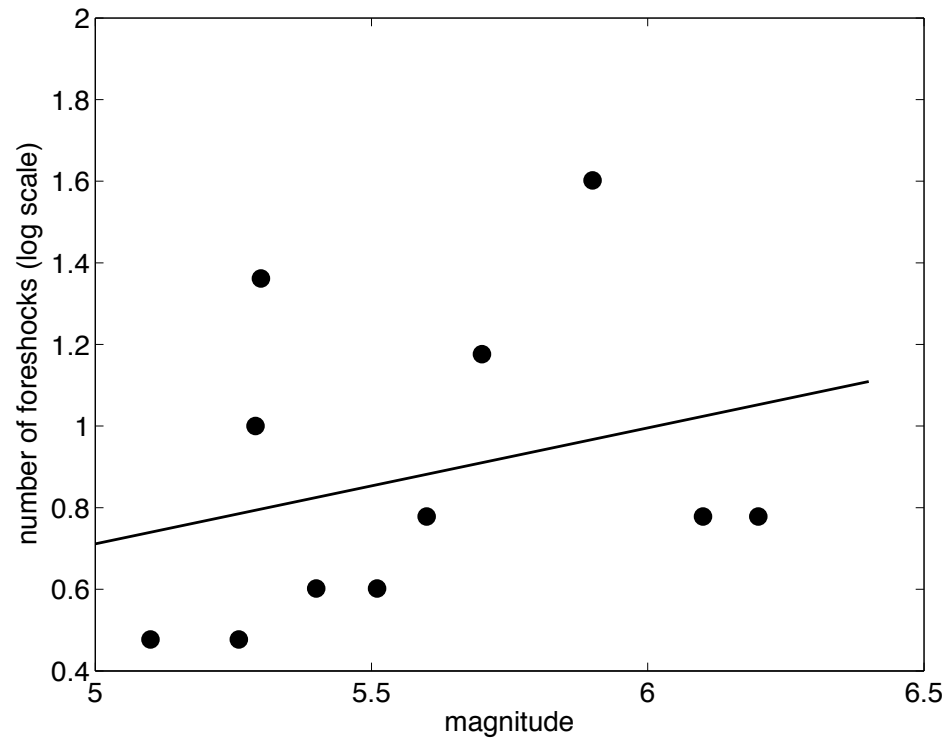
Figure 6.6: Number of foreshocks versus mainshock magnitude (includes 11 main-shocks with M>5 and M<7). Black line is an empirical fitting between $\log_{10}(\mathrm{N}_{fore})$ and magnitude.
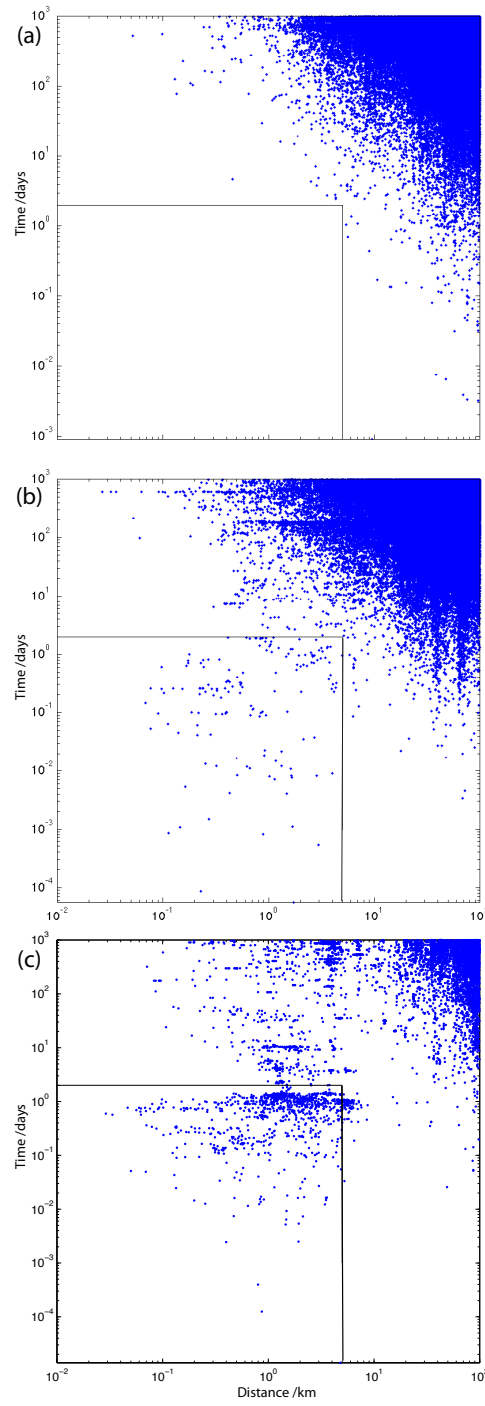
Figure 6.7: Precursory seismicity within 1000 days and 100 km prior to target mainshocks with M> 5. Three mainshock types are included: (a) mainshocks with no foreshocks; (b) mainshocks with ≥ 1 foreshocks; (c) earthquake swarms. Horizontal black lines correspond to T=2 days, vertical black lines correspond to D=5 km, illustrating the selection criteria of foreshock sequences.
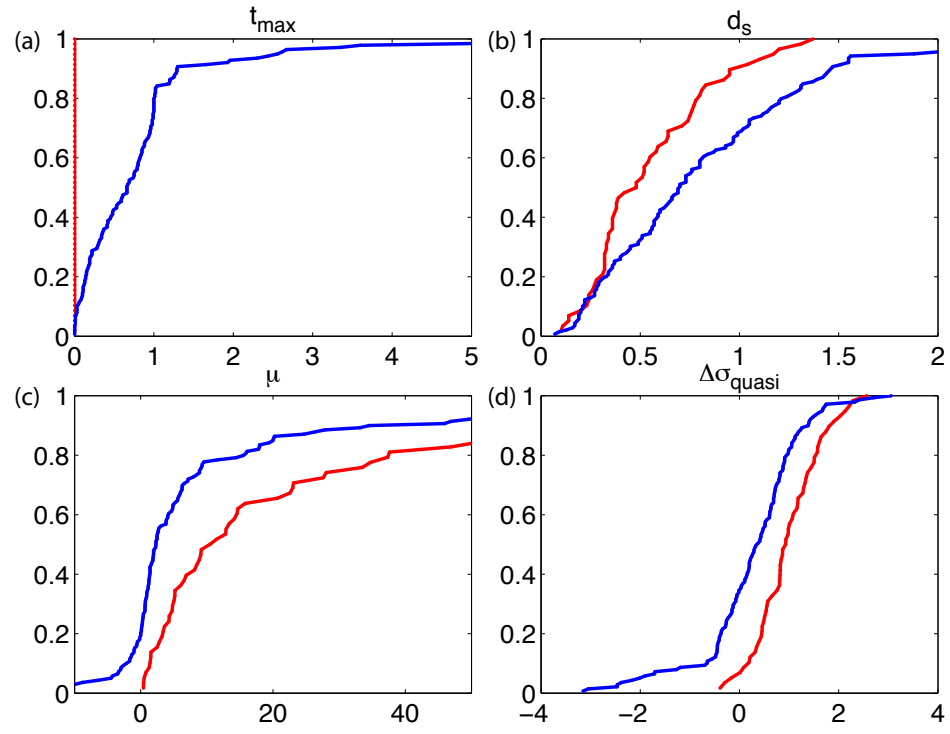
Figure 6.8: Distribution of different parameters for: no foreshock (red) and with at least one foreshock (blue).
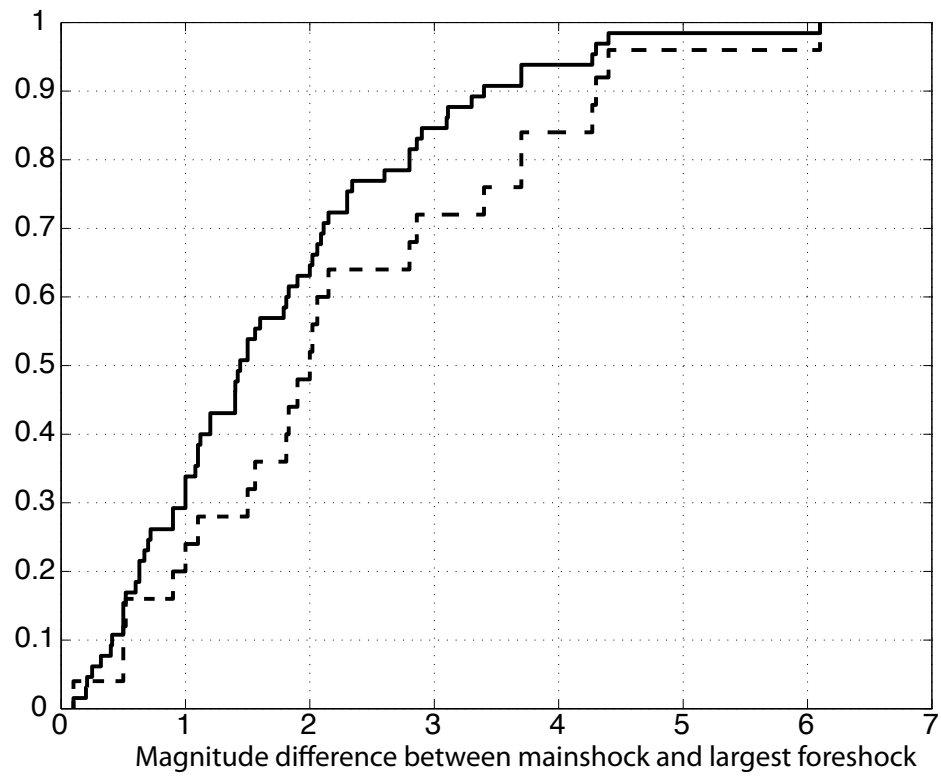
Figure 6.9: Magnitude difference between mainshock and largest foreshock. Solid line: M≥4 mainshocks, dashed line: M≥5 mainshocks.

169
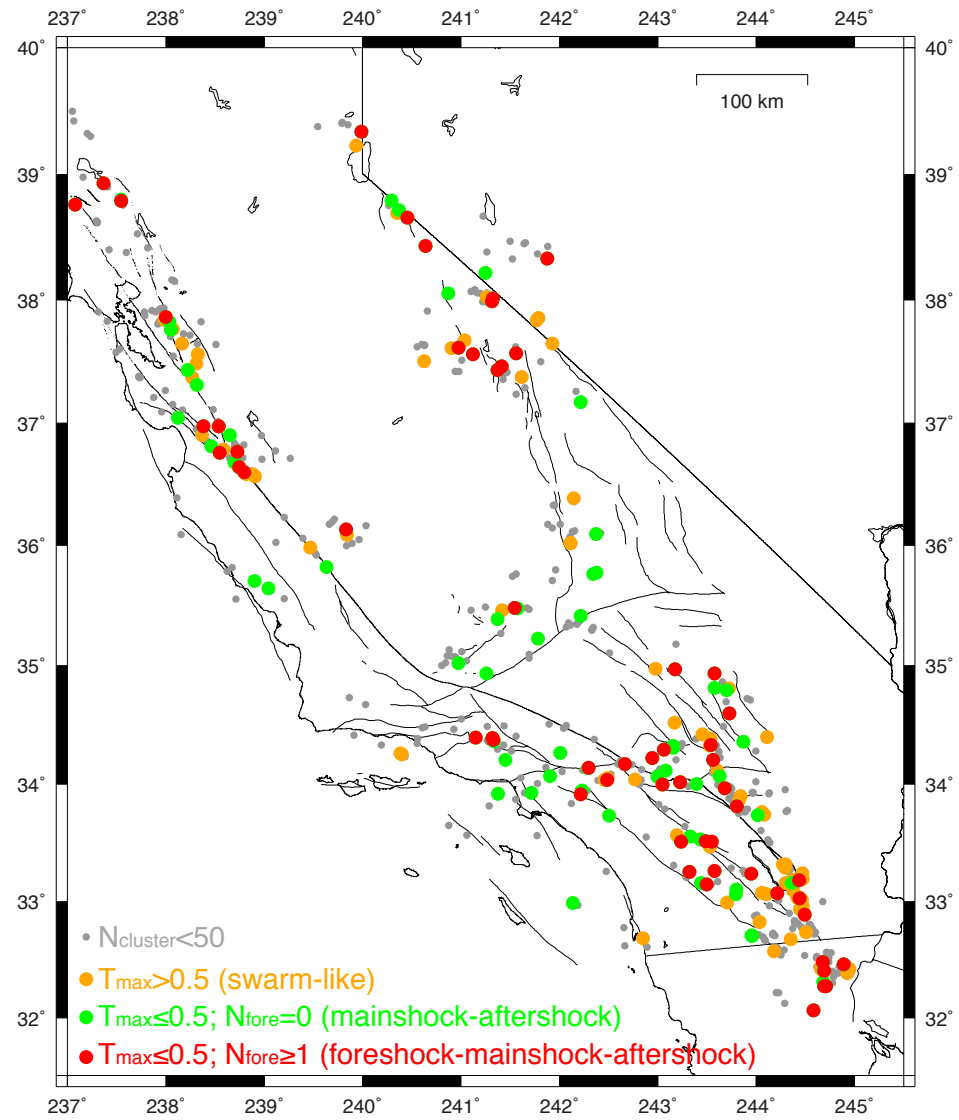
Figure 6.10: Map view of seismicity bursts in California.